Università degli Studi di Ferrara

INTERNATIONAL DOCTORAL COURSE IN
"EARTH AND MARINE SCIENCES (EMAS)"

CYCLE XXXIV

COORDINATOR Prof. Massimo Coltorti

Relationship between chemical and structural features of topaz to unravel the formation conditions: A multidisciplinary approach

Scientific/Disciplinary Sector (SDS) GEO/06

Candidate
Dott. Nicola Precisvalle

Supervisor
Prof.ssa Annalisa Martucci

Co-Supervisor
Prof.ssa Costanza Bonadiman

Years 2018/2021

1 [1]Parole di Qoèlet, figlio di Davide, re a Gerusalemme. [2]Vanità delle vanità, dice Qoèlet,
vanità delle vanità: tutto è vanità. [3]Quale guadagno viene all'uomo per tutta la fatica con cui si
affanna sotto il sole?

(Qo 1:1-3)

Dedicata a Luisa

Acknowledgments

At the end of this thesis, I would like to thank all those people who helped me and supported me in this journey. First, I would like to thank my supervisors, Professor Annalisa Martucci and Costanza Bonadiman, who have been more than just supervisors to me, but guides and role models. I thank them for having believed in me from the start and for their family affection.

I would then thank all the scientists that allowed me to pursue the experiments for this thesis. I will list them here in order of our meetings: Dr. Lara Gigli (Elettra – Trieste), Dr. Jasper R. Plaisier (Elettra – Trieste), Dr. Antonio Langone (CNR IGG Pavia), Dr. Alberto Zanetti (CNR IGG Pavia), Mr. Leonardo Tauro (UniPD), Thomas C. Hansen (ILL – Grenoble), Dr. Lisa Vaccari (Elettra – Trieste), Dr. Diana Eva Bedolla Orozco (Elettra – Trieste), Dr. Giovanni Birarda (Elettra – Trieste), Dr. Chiaramaria Stani (Elettra – Trieste), Dr. Alessandra Gianoncelli (Elettra – Trieste), Dr. Valentina Bonanni (Elettra – Trieste), Dr. Gianluca Gariani. I also want to thank here Dr. Augusto G. Nobre (University of São Paulo), who provided these beautiful blue topazes.

Special thanks go to Dr. Sergio Speziale (GFZ-Potsdam), for hosting me and teaching and giving me so much. When I left for my short stay, I knew I would find a great tutor, but I never imagined I would have found a friend.

I would like to thank my parents Gabriele and Stefania and grandparents with great affection for their help, my best friend Adriano for keeping me company in my sorrows and complaints, my colleagues and all the people I have met along the way.

Finally, I would like to thank Luisa, the person to whom I dedicated this thesis, for all her love, smiles, trips, adventures, and physical and moral support. I thank the fact that our buses arrived in Chieppara at the same time and that the Chinese restaurant in the city centre did not deliver on New Year's Eve. I still get a little scared of something new, but I feel a little safer when I'm with you.

Abstract

Topaz, $Al_2SiO_4(OH, F)_2$, is one the principal fluorine bearing silicates that occurs as accessory minerals in fluorine rich silicates rocks associated with magmatic or hydrothermal events. The structure consists of $[SiO_4]^{4-}$ groups linking octahedral chains of $Al[O_4(F, OH)_2]$ in a zig-zag arrangement parallel to the c-axis. Four out of the six anions surrounding the Al^{3+} ion belong to $[SiO_4]^{4-}$ tetrahedra and two from F^- or OH^- groups. Natural topaz crystallizes in the orthorhombic *Pbnm* space group. This thesis has fully characterized two topaz "families" from different origin, natural blue topaz from Padre Paraìso municipality (Brazil) and colourless topaz from Baoshan county (China) and propose a geochemical model to link the crystal structure to a possible geological environment, thus possibly determine the gem identity and provenance. In order to achieve this, a multi-analytical approach has been chosen. Major and trace element contents evidenced significate chemical differences between the Brazilian and Chinese population. The spatial distribution of Al, Si, Ga, Ge, As, as well as those of F and OH obtained with X-ray mapping confirmed a random distribution of O and F in octahedra, Al-Ga and Si-Ge substitution also for topazes' surface. Arsenic, for the first time, has been shown to be included in topaz either as a substitute for Si (as in the case of Padre Paraìso topaz) or absorbed in the cavities between octahedrons (as in Baoshan topaz). The crystal structure and thermal evolution have been studied by means of synchrotron X-ray powder diffraction and neutron powder diffraction with *in situ* heating from 298 to 1273 K. The successful strategy to combine chemical microanalyses with synchrotron X-Ray and neutron powder diffraction measurements allowed to accurately determine both the mineral structure and crystal chemistry. On the basis of neutron diffraction data, topaz fluorine content is estimated to be ~ 1.03 a.f.u (Padre Paraìso) and ~ 1.59 a.f.u (Baoshan) with OH/(F+OH)= 0.484 (Padre Paraìso) and 0.240 (Baoshan), in very good agreement with the chemical measurements (F ~ 1.05 a.f.u and ~ 1.52 a.f.u for Padre Paraìso and Baoshan respectively). The topaz – mullite transformation (that for the first time here has been reconstructed through heating ramp diffraction analyses) occurs at different temperatures for Padre Paraìso and Baoshan (1181 K and 1225 K, respectively). These temperatures are interpreted as the potential initial crystallization temperature of topaz in a fluid-dominated system. In such a view, it is possible to infer that Padre Paraìso topaz nucleated at ~1148-1181 K from a water rich /fluorine poor fluid $((fH_2O/fHF)^{fluid} \sim 4.5$ log units); instead Baoshan topaz started to form at higher temperature ~1203-1225 K from a water poor /fluorine rich fluid $((fH_2O/fHF)^{fluid} \sim 1.2$ log units). Altogether these data allowed a fair identification of both topaz deposits. The Padre Paraìso topaz is associated with pegmatitic type deposits with a good degree of confidence regarding the type of pegmatite documented in the region that generated it, while the Baoshan topaz is related to a greisen type reaction thus reducing the number of possible topaz source deposits (hydrothermal, magmatic and greisen) present in the Tengchong-Baoshan Sn-polymetallic metallogenic belt.

Table of contents

1. Introduction and aim of the work

Topaz, $Al_2SiO_4(OH, F)_2$, is one the main fluorine bearing silicates that occurs as accessory minerals in fluorine rich silicates rocks associated with magmatic or hydrothermal events (Alberico et al. 2003, Zhang et al. 2011). In some cases, it can also be a principal component in some peculiar rocks called "topazite" (or topaz rhyolites) (Korteimer and Burt, 1988, Burt et al. 1986, Soufi 2021) and topaz ongonite (Burt et al. 1986, Soufi 2021). Because of this characteristic, topaz deposits are spread worldwide and can form in very different environment. The structure consists of $[SiO_4]^{4-}$ groups linking octahedral chains of $Al[O_4(F, OH)_2]$ in a zig-zag arrangement parallel to the c-axis. Four out of the six anions surrounding the Al^{3+} ion belong to $[SiO_4]^{4-}$tetrahedra; and two form F^- or OH^- groups (Fig. 2a, b). Natural topaz crystallizes in the orthorhombic *Pbnm* space group; pronounced sectoral textures with growth planes {hkl} optically triclinic, {0kl}, {k0l}, and {hk0} optically monoclinic, and {100}, {010}, and {001} optically orthorhombic are also well documented. (Precisvalle et al. 2021)

By the way, this mineral is not only an important petrologic indicator, but also a well renowned gemstone that since ancient times is searched and desired by people for its beauty. From the literature) The main method to distinguish topazes of different origins is to determine the OH/F ratio (Ribbe & Gibs 1971, Ribbe & Rosemberg 1971, Wunder et al 1999). To do this, methods based on the study of the structure of topaz have so far been used, through correlations between the measurement of its cell parameters (in particular *b* parameter and Unit cell *Volume*) and the estimation of the weight percentage of F, then obtaining the OH content by difference (Ribbe & Rosemberg 1971, Alberico 2003). However, this method, although effective when comparing a small number of samples, proves to be deficient when the number of topazes of certain origin increases and compared with each other. In addition, another limitation of this methodology is that it does not consider the various types of deposits, which, as mentioned above, differ greatly in the chemistry and temperature

of the magmas or hydrothermal fluids. Nowadays, however, one of the major issues in gemmology is the traceability of the origin of the stones that are placed on the market with a view to more sustainable consumption and a supply that is more sensitive to respect the workers at the bottom of the supply chain. This has already been in place for some time, especially regarding the source of diamonds, through the famous Kimberly process established by the UN in 2003 to prevent "conflict diamonds" from entering the mainstream rough diamond market. This is complemented by other, more modern certifications by large mining companies or gemmological laboratories (such as Alrosa or Gubelin). These guarantees, however necessary they may be, are, for cost and market reasons, operated on those gems known as the 'big three', i.e., emeralds and rubies (and sapphires).

In this thesis two topaz "families" from different origin, natural blue topaz from Padre Paraíso municipality (Brazil) and colourless topaz from Baoshan county (China), has been fully characterized in terms of geochemical and crystallographic features in order to explore the relationships between structure (i.e., OH/F substitution) and environmental conditions. The aim of this work is to establish a correlation between OH/F ratio and formation chemical environment in relation to the efficiency of the mineral/fluid partitioning process in topazes and in the end, define a model to explain the accommodation of elements in the crystal structure as function of the geological environment, thus possibly determine the gem identity and provenance.

2. Topaz review

2.1 Mineralogical aspects

Topaz is a well-recognized and prized gemstone, and it is of primary importance to know all the aspects that characterize it as a mineral, in order to fully understand the genesis in the frame of ethical exploitation.

The average chemical formula for topaz is $Al_2SiO_4(F, OH)_2$, with a variable ratio between F and OH. Topaz belongs to the nesosilicate class and crystallize in the orthorhombic space group Pbnm, although Parise et al. (1980) reported a case of a P1 crystallization in extreme ambient condition topaz achieved by ex-situ heating. This has been explained because of H uneven position. In 1928 the structure of topaz has been solved independently by Pauling (1928) and Alston and West (1928), while the refinement of the structure has been pursued long time after by Ribbe and Gibs (1971).

The structure consists of alternated chains of edge-sharing $AlO_4(F, OH)$ octahedra that run parallel to the c axis. These chains are connected through corner sharing SiO_4 tetrahedra (Figure 1). From a morphological point of view, topaz belongs commonly to the orthorhombic dipyramidal class (Wise, 1995). Its habit is quite variable, ranging from long, slender, prismatic to short, stubby with simple to highly modified pyramidal, blunt, wedge-shaped, or chisel-shaped terminations. (Wise, 1995).

There are a large number of topaz forms, the largest study about these has been carried on by Goldschmidt in 1913 who listed some more than 250 possible forms for topaz crystal. The most common forms are the prisms: {110}, {120}, {011}, {101}, and {021}; the other "normal" forms are dipyramids {113}, {112}, and {111}; but pinacoids {010} and {001} are also observed. Unfortunately, as this work was conceived before the discovery of the structure of topaz, and even

earlier the refinement of this, Goldschmidt had no knowledge of how the OH against fluorine substitution affects the topaz structure; an important issue that remains unclear is how the OH/F ratio affects the morphological aspects and shape of topaz.

The chemistry of Topaz is simple and, apart from the OH/F substitution, with no major variation among different population from different deposits. Ribbe and Rosemberg (1971) and Foord et al. (1995), by the way, have documented some substitution of Al with Fe^{3+} and Cr^{3+} and Mn^{3+}. In some chemical characterization the presence of Ca, Fe, Mg, Na, K, P and Ti (up to 0.1 wt.%) have been reported (Deer et al. 1982, Wise 1995), but how them arrange into the structure is still not clear. Most commonly these elements are present as the trace-elements (at ppm level). In particular topaz from rhyolites is richer in light elements such as Li and B, while pegmatites and hydrothermal topaz are richer in Co, Cu, Sn, W, Fe, Mn., Ga, Ge (EI-Hinnawi and Hofmann 1966; Marchenko and Shcherbakov 1966; Hervig et al. 1987, Foord 1991, Wise 1995).

2.2 The OH/F ratio and how it affects topaz structure

The following section has been previously published as part of the paper "Precisvalle et al. "F/OH ratio in a rare fluorine-poor blue topaz from Padre Paraíso (Minas Gerais, Brazil) to unravel topaz's ambient of formation". Sci Rep 11, 2666 (2021)."

Topaz is one of the principal fluorine-bearing silicates that occurs as an accessory mineral in fluorine-rich silicate rocks (rhyolites and granites) associated with pneumatolytic/hydrothermal events, and in ultrahigh-pressure rocks (Alberico et al. 2003, Zhang et al. 2011). Its composition ranges from a nearly OH-free end member, $Al_2SiO_4F_2$, in acid igneous rocks, to $Al_2SiO_4F_{1.4}(OH)_{0.6}$, with X_{OH} = OH/(OH+F) = 0.30, in hydrothermal deposits (Barton et al. 1982). Higher OH content was reported for topaz found in ultrahigh-pressure (UHP) -rich topaz–kyanite quartzites from Hushan (west of Dongai), (X_{OH}=0.35), and southern Sulu (X_{OH} = 0.40-0.55), eastern China (Zhang et al. 2002). A series of hydroxyl-rich topaz (OH-topaz) from X_{OH} = 0.22 up to the pure endmember $Al_2SiO_4(OH)_2$, were synthesized (Wunder et al. 1999) at high-pressure/high temperature conditions (pressure from 5.5-10 GPa, temperature up to 1273 K) in the Al_2O_3-SiO_2-H_2O system. For this reason, the study of the OH/F ratio plays a key role to understand the topaz's formation ambient. Usually, natural topaz with OH/(OH + F) < 0.5, crystallizes in the space group *Pbnm*, with one independent H-site, whereas in synthetic $Al_2SiO_4(OH)_{2\ it}$ displays two non-equivalent H-sites. The existence of an upper limit to the OH content is rationalized in terms of hydrogen located in two partially occupied sites whose occupancy limits the OH substitution for F to 50% ("proton-proton avoidance rule") (Parise et al. 1980). Conflicting results about the exact space group were reported for the synthetic endmember "topaz-OH" (Northrup et al. 1994, Chen et al. 2005, Komatsu 2008). Northrup et al. (1994) found that in topaz-OH hydrogen atoms are spread over two independent crystallographic sites; one of these is not found in naturally occurring fluorine-bearing topaz. Both sites lie close to the mirror plane in the space group *Pbnm,* but their short distance (1.7Å) prevents their simultaneous occupancy.

The proton environment in the topaz-OH was recently depicted by (Mookherjee et al. 2016) by first principle simulations on periodic systems, using the Hartree-Fock and Kohn-Sham self-consistent field method. As a result, two space groups, were reported: higher energy orthorhombic form *Pbnm* and a lower energy monoclinic form $P2_1/c$.

The structural and elastic properties of topaz are strongly related to the fluorine content which determines the compressional behaviour of topaz; this causes polyhedral tilting and contraction as well as hydrogen bonding (Gatta et al. 2006, Mookherjee et al. 2016, Ulian & Valdrè 2017).

After *ex situ* heating at 1223 K for 18 h, the symmetry of topaz deviates from orthorhombic, suggesting *P1* as a possible space group (Parise et al. 1980). The structural data were not reported in the paper, only the H-site coordinates (derived from the difference Fourier map) in the *Pbnm* and *P1* space groups were given. The response to increasing pressure and temperature of natural topaz from Gilgit division, Pakistan, was described by structure refinements from single crystal X-ray diffraction data (Komatsu et al. 2003). Consequently, Al-O bond distances and the OH/F ratio controlling the thermal expansion and compression of topaz show an inverse relationship.

IR and Raman spectroscopy (Pinheiro 2002, Bradbury 2003, Lutz 2003, Komatsu et al. 2005) carried out on both natural and synthetic topaz-OH explored the relationship between the structure and the strength of hydrogen bonds and suggested that additional phenomena like synergetic, cooperative, anti-cooperative or competitive effects govern the donor's strengths and the acceptor's capability. Two stretching OH bands (ν(OH)) due to the local F/OH ordering in opposite sites of the structure were distinguishable. Upon compression, the ν(OH) shifted to a lower frequency in topaz-OH and to a higher frequency in F-rich ones (Komatsu et al. 2005).

With increasing temperature, two phase transitions were detected: the first from *P1* to $Pbn2_1$ (~408 K), involving only the H atoms; the second (~433 K), from $Pbn2_1$ to *Pbnm* due to local F/OH ordering in the crystal structure (Peterson et al 2017). Consequently, the real concentration and distribution of F and OH in natural topaz crystals can help to understand how the hydrogen bond geometry influences the OH behaviour with temperature, but not with any certainty.

To understand these mechanisms is important to determine the hydrophilicity and the exchange reactions of fluorine by hydroxyl groups, and ultimately to characterize the environmental redox conditions (H_2O/ F) required for the formation of topaz.

However, OH/F ratio does not affect only the structure of topaz, but also its physical and optical properties. Ribbe and Rosenberg in 1971 pursued a large study about this issue. They found out that the optic angle of topaz can go from 48° for low fluorine content topaz to up to ≈70° in high F topaz (Ribbe and Rosenberg 1971).

Figure 1. Schematic representation of topaz structure along the *a* and *c* axis. The colour scheme is: dark grey for Al octahedra, blue for Si tetrahedra, light grey for oxygen or fluorine atom site, white for hydrogen (from Precisvalle et al. 2021)-

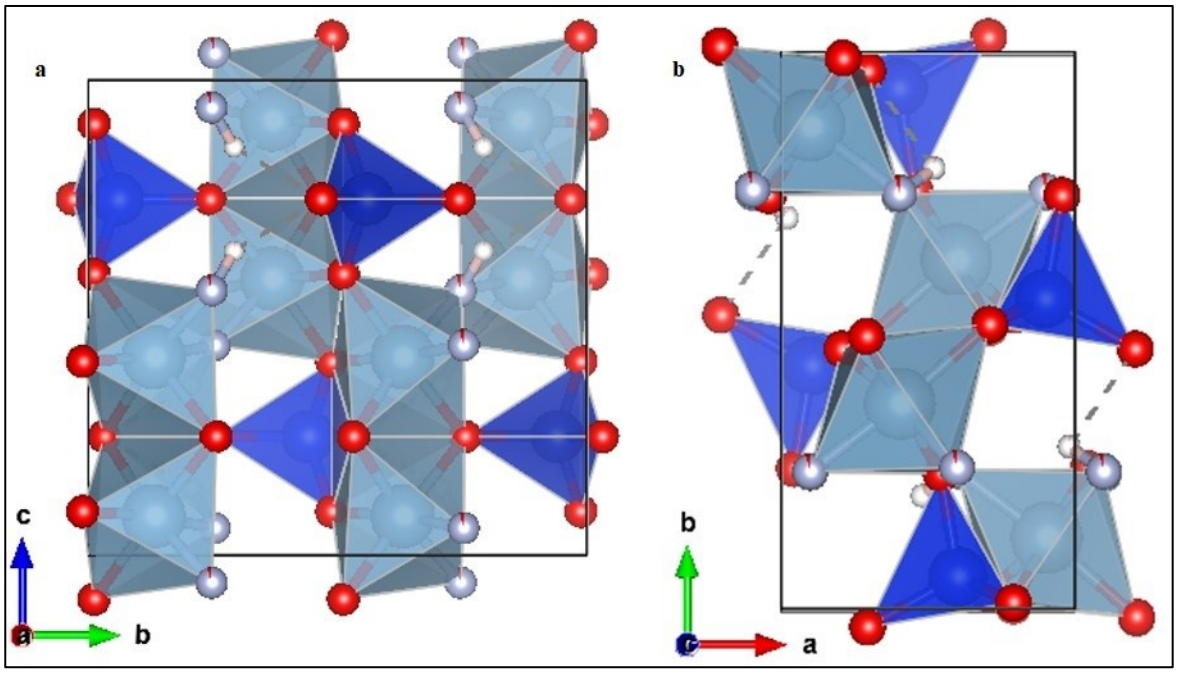

2.3 Gemmological aspects

Although topaz is often overshadowed by gems such as diamonds or the so-called 'big three', i.e., emerald, ruby and sapphire, it remains a key player in the world of jewellery. Since ancient times, when first mines of topaz had been exploited by Romans in the Saxony region in Germany, men and women prized topaz for its transparency, lustre and the wide range of beautiful colours. The term topaz probably came from the island Topazos, which is nowadays the island of Zabargad in the Red Sea (Figure 2). The Topazos island was famous among Europe, Egyptian empire, and Middle East because of beautiful intense green stones. Ironically that green gemstones were not topaz, but peridot. Another possible explanation for the origin of the term topaz is the Sanskrit word *tapas*, which means "fire".

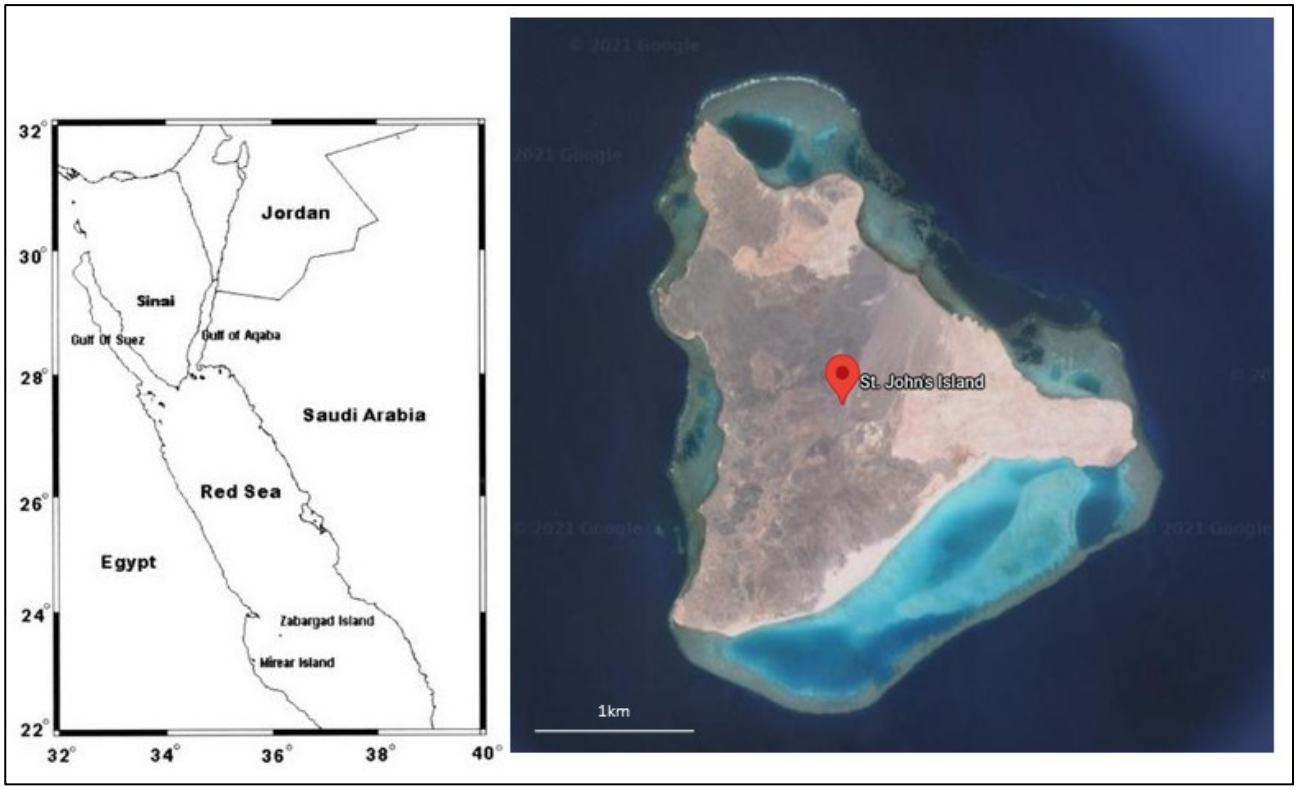

Figure 2. Satellite map of Zabargad Island (also known as "St. Jhon's Island) and its position in the Red Sea. The sketch is taken from El-Manawi (2001), the photo from Google Maps

However, during the Classical and Post-Classical Antiquity topaz was a generic term for many different transparent minerals with a faint colour between green and yellow. In the Middle Ages, the word topaz started to be used as a generic term for colourless to yellow gemstones such as the proper topaz, but also quartz, citrine quartz, sapphire, zircon, and garnet (Wise 1995).

In the 1747, the famous German mining and mineralogy scholar Johann Friedrich Henckel finally assign the name topaz to the World-famous fluorosilicate (Wise 1995).

During history many properties had been attributed to topaz; ancient Greeks thought that topaz could gave them strength and courage, the Romans even believed that topaz put in a liquid could revelated poisons and make them ineffective. In the Renaissance topaz had been used in alchemy and popular magic as spell breaker and remedy against anger.

One of the characteristics that make topaz such a renewed gemstones is its peculiarity to occur in very large samples, not only good for classical gem-cutting but also for carving. Among these the most famous faceted "record holder" topaz are Champagne Topaz (36,853 cts.), the American Golden (22,857 carats), The Brazilian Princess (21,005cts.) and the Ostro blue Topaz (9,831 cts.). (Wise 1995). Coming to carved topaz it is important to mention the "San Cataldo Topaz" or "Ferdinand the Second Topaz". This piece of art is really one of a kind, and it has been cited as one of the greatest pieces of sculpted jewellery in the world. It consists in a large (4 kg circa) carved imperial topaz from Brazil, carved by the "Real Laboratorio delle pietre dure di Napoli" in the middle of XIX century.

However, topaz in history is not only famous for exceptional finds, but also for famous 'oversights'. The most famous one is without doubt the "Braganza Diamond" set in the now lost Portuguese Crown Jewel. The "Braganza Diamond" were found in the XVIII century in Minas Gerais in Brazil and, with its 1,680 cts. it was praised as the largest diamond ever found in that times. It was not a diamond, but a perfect transparent and flawless topaz. Still today topaz is sold as diamond imitation. Besides its quality of reaching large size another characteristic that makes topaz highly sought-after is its wide variety of colours. Most of topaz found are colourless or very pale yellow, but they can

appear in other colours like full, straw yellow, golden, amber, pale to intense brown, pale to strong blue, red, violet, orange, and very rarely pale green. The varieties peach, pink, champagne, medium reddish orange to orange red, orange-yellow and yellowish brown are all named "Imperial topaz". Still today the causes of this large pallet of colour in topaz are not very clear. The theory of "colour centres" and the effects of chromophores' ions are frequently invoked to explain this large colour variety.

The "colour centres" are defects in the crystal structures that lead to selective absorption of certain frequencies of visible light. These are single or clustered, such as impurities, missing ions, imperfection in crystal lattice, in a normally colourless material. Such defects cause the material coloration when the electronic ground state is excited to higher energy states by visible light (Wise 1995, Tilley 2014). Colour centres are probably cause of blue and yellow-to-brown colours (Wise 1995). Other causes of colours in topaz are the chemical substitutions. The Fe^{3+} substitution of Al is thought to be responsible for the pale blue and yellow colours. (Schott et al. 2003) However, the most important element in the colouring of topaz is undoubtedly chrome. Petrov (1977) made the first important studies on how the Cr^{3+} becomes responsible of different colours in topaz He divided three main group of topaz colours on the bases of chrome behaviour and defects. The first group there are topaz where the d-d transition of Cr^{3+} provoke the violet colour. The second group there are topaz where the colour is due to defects centres in structure. To this group belong red, yellow, blue, and rare green topaz. In the third group there are topaz where both defects centres and Cr^{3+} substitutions are present. To this group belong the so called "imperial topaz" with yellow-orange, orange, orange-violet and violet topaz. (Petrov 1977, Petrov et al 1983)

More recently, Schott (2003) lists additional parameters like temperature, natural radiation, sensibilization of special defect centres by "foreign" ions in combination with individual structure properties and chemical composition as causes of colours in topaz.

The refractive index (R.I.) is impacted by the OH/F content; the fluorine richest topaz shows R.I in the range of 1.609 - 1.618, while the OH rich topaz report higher values: 1.630 -1.639.)

The density of topaz ranges from 3.513 - 3.563 g/cm^3. This variability depends on the F content, as long as the more fluorine corresponds to a denser sample.

The topaz hardness on the Mohs scale is 8, and it is used in this scale as mineral of comparison (Broz et al. 2006).

The abovementioned physical and chemical features are related to natural topaz, but this stone can be subjected to various treatments that can change its appearance and chemico-physical characteristics. The most common treatment for topaz is irradiation, using various sources. Through irradiation by gamma rays topaz can assume a yellow-to-brown, dark brown, reddish-brown colour, and pale blue if irradiation is associated with heating. The effects of gamma rays disappear if the treated topaz is exposed to white/natural light for long time or by heating/or reheating up to 200°-300° C (Nassau 1985). The irradiation by high-energy electrons induces an intense and strong blue colour but, due to the strong internal electrical discharge, this type of treatment can be recognized by the presence of "internal lighting" (Figure 3) (Nassau 1985). This method is usually applied to large specimen.

The last type of irradiation known for blue colour is the neutron-irradiation. The effect of this irradiation is a deep blue colour (also in this case a heating process is required). This method is probably the most stable thanks to the high penetrative factor of neutrons. (Nassau 1985)

Heating, by itself is another widely used treatment for topaz. This process is commonly used to remove the yellow or brown component from "imperial topaz" in order to obtain a more desirable pink colour. This heating process is performed with temperature between 400° and 500° C degrees (Figure 4). (Nassau 1985)

Another treatment applied to topaz is the superficial coating. Colourless topazes are coated with different metal oxides to magnify the original (natural colour) or even to induce a completely new colour (Figure 5). However, this is just a very shallow treatment, and it can be removed by simple polishing. A rarer treatment is the fracture filling; this treatment is rarely applied in topaz by the fact that this gem easily form crystals with relatively small internal fracture.

Figure 3. Internal lighting inclusion in irradiated topaz. (Modified from Nassau 1985)

Figure 4. Color transformation from open flame heating. The upper topaz changed from a yellow-to-brown colour (like the bottom topaz) to a pink-violet hue. (Modified from Nassau 1985)

Figure 5. Here some typical colours for topaz are listed. In the first line, typical blue topaz from irradiation and their commercial names. In the middle, 3 hues of natural imperial topaz. In the last line the Mystic and the Azotic®, both from superficial coating. The last sample is a natural orange-brown topaz.
(The image is taken and modified from Diamond Buzz/Diamondbuzz.blog and belongs to Diamond Buzz® under regime of Standard Image License)

Topaz, as mostly precious gemstones, has its own synthetic counterparts. Actually, the synthetic topaz is not so diffuse on the market, but it is used as refractive material in ceramic or in glass and steelmaking industries, as components in moulds, furnaces etc… In these cases, synthetic topaz is preferred for the homogeneity of the material and because the chemical and physical characteristics are controlled by the manufacturer. However, natural topaz is so common and widespread that is uneconomical its production for this purpose. Moreover, in the jewellery industry, the natural characterises of the gem always prevail over the synthetic beauty perfection. Anyway, two main methods are used to synthetize topaz: hydrothermal (most common) and pulling methods.

The high availability of this material means that prices can fluctuate by several percent, where colour is probably the main factor of this oscillation. The Pala International site (palagems.com), one of the biggest and most famous gems trading company, gives some idea of topaz prices on retail. It goes from few dollars per carat for colourless topaz (they cite less than 8$/ct. for cut gemstones up to 100 cts. for the 2021) to up to 25$/ct. for blue topaz whether irradiated or not. Since the '90s most, if not nearly all, the blue topazes on the market today are irradiated topaz. This large availability also

influenced the prices of the rarer natural blue topaz too. The highest price for topaz is referred to the "imperial topaz". Referring to the Pala International site, the mean retail price for intense, orange-coloured topazes (i.e., cut gemstones from 10 ct. or more) is around 1000$/ct. The highest priced topaz are for the "imperial pink topaz"," imperial purple topaz" (imperial topaz with no orange colour component at all) and red topaz. For these coloured gems (even pieces smaller than 5 cts.) the price can also go up to 3500$/ct. A collier with intense orange topazes cushion cut (up to 220 cts. in total) by JAR has been sold by Christie's for circa 350k dollars (lot 269, Christie's catalogue, 13/06/2019), but the record for the most expensive piece of topaz jewellery belongs to a pair of ear pendants with intense orange topazes elongated cut always designed by JAR and sold by Christie's for 710,400 dollars (lot 97, Christie's catalogue, 10/10/2006.

2.4 Topaz deposits

Topaz is the main fluorosilicate of the Earth's crust and occurs in a great variety of geological environment. Together with quartz, topaz is the mineral ubiquitous in the crustal terrains worldwide. (Rudnick and Gao, 2014). Of course, as quartz, not all topazes are of gemmological interest. In addition to the majority of worthless gem-type topaz (too many inclusions, small crystals, unremoved internal defects), topaz can appear in acicular, micro-crystals or in polycrystalline forms that exclude the cut.

What all topaz deposits have in common is their relationship with the different phases of formation and evolution of granites and granitoids. (Wise, 1995) Magmatic, post-magmatic and hydrothermal

events, during the various stage of granite formation and emplacement, give rise to different topaz deposits. (Wise 1995).

The last stage crystallized events (liquid phase), the post magmatic events (hydrothermal phase and vapour phase) characterize the various topaz formation process ((Foord 1991, Wise 1995). That one thing all these processes must have in common is the enrichment in fluorine content.

In magmatic deposits the condition for topaz growing is possible only in metaluminous and peraluminous environments. (Dolejš and Baker 2004, Soufi 2021).

Experimental petrology has shown that the amount of CaO in relation to the amount of F in a fluorine-rich melt actively regulates topaz crystallisation. (Xiong et al 1996, Li et al. 2004, Soufi 2021).

Gioncada et al. (2014) demonstrated how the progressive calcium depletion of the melt due to the fractionation of CaO-rich minerals (such as plagioclase and apatite) favours a relative abundance of F and consequent crystallisation of topaz rather than fluorite. (Giocanda et al. 2014, Soufi 2021).

Soufi et al. (2018) showed how the fluorine concentration in magmatic topazes is closely related to their host magmas.

On the other hand, from experiments on hydrothermal topaz it has been shown that another important parameter in the formation of topaz is the initial ratio of OH/F for starting material and growth environment, expressed by this formula (Rosemberg 1972, Wunder et al. 1999, Soufi 2021)

$$\frac{OH}{(OH+F)}$$

However, temperature remains a key factor during topaz crystallisation. Generally, as the temperature decreases, the concentration of fluorine in the melt increases and consequently the resulting topazes tend to be F-rich. (Xiong et al 2002, Li et al 2004, Soufi 2021)

In the following sub-sections I will give a brief description of the most common topaz deposits. Not all the deposits here described are prone to generate gemmological quality topaz, but I decided to include them anyway so as to give a broader view of the formation of this mineral.

2.4.1 Topaz granites

Topaz granites is the name for F-rich granitic rocks that contains an important amount of euhedral or sub-euhedral topaz (up to 10-15%) (Wise 1995). in association with a "normal" granites paragenesis: alkali feldspar, albite, quartz and micas. Accessory minerals (< 1 % of the modal contents) that could be present are Nb-Ta bearing rutile, columbite-tantalite, cassiterite, monazite, apatite, and tourmaline. (Wise1995).

Topaz granites are often part of large plutonic complexes including stocks or dikes, along their margins or on the roof, with miarolitic cavities and pegmatitic facies. (Wise 1995).

This kind of deposits can be found in Europe along all the European Variscan belt, most famous examples are the Krušné hory/Erzgebirge region (Bohemian Massif) (between Czech Republic and Germany), Cornwall (England, UK), the French Massif Central (France) and the Iberian Massif (Spain and Portugal). (Soufi 2021; Breiter, and Kronz,2004). In North America we have great examples in the Canadian Appalachian Mountain belt of Nova Scotia and New Brunswick (Canada). (Taylor 1992, Yang et al. 2008, Soufi 2021)

In China the Jiangxi metallogenic province host the Hongshan F-rich pluton and the Yichun topaz-lepidolite granite, the Zhejiang province host the Yangbin topaz-quartz porphyries and in Xinjiang the Baishitouquan topaz- amazonite- leucogranite; other Asian topaz granite are present in Vietnam. (Soufi 2021) In Africa, it is worth to mention the Erongo granite in Namibia, world famous gemstones deposits of topaz and tourmaline. (Gu et al. 2003, Gu et al 2011, Soufi 2021) .

2.4.2 Greisens

A type of topaz deposit closely related to granites is the greisen. The greisens are metasomatically altered granitic rocks by hydrothermal fluids. (Wise 2005) These fluids, enriched by F, B, Be, Sn, W and Mo interact with feldspars and muscovite and produce the typical greisens paragenesis mica-topaz-quartz. (Wise 2005)

The greisens are also important as ore for different oxides and sulfides such as: stannite, wolframite, sheelite, pyrite, bismuth etc… (Pirajno 2008). Taylor (1979) and Hutchinson (1998) connect the Sn and W greisens (i.e., the types of greisen in which topaz appears in larger and euhedral samples) to S-type granitic rocks. This kind of affiliation usually appears in dome-like and ridge-like structure. (Taylor 1979, Hutchinson 1998, Pirajno 2008). Some examples of greisen topaz deposits are the Yunnan metalliferous deposits in Yunnan region (China), the Potosi deposits in the Rondonia (Brazil), the Hillsborough pyrophyllite deposit in North Carolina (USA), and the Triberg granite complex (Germany). (Sykes & Moody 1978, Markl and Schumacher 1997, Yokoi et al., 1987, Almeida et al. 2007, Rojas et al. 2009, Soufi 2021)

Another kind of scarn deposits is the “greisened skarns deposit”. It is very similar to the systems described above but apply to the skarns veins. The formation of topaz is a direct result of gresenization process of previously formed calc-silicate and unreplaced carbonates. (Kwak 1987, Wise 1995) These deposits are spatially and temporally related to the above-mentioned topaz-bearing skarns and generally occurs along their margins, in particular in Sn- and W- greisens. (Wise 1995)

2.4.3 Pegmatites

The pegmatites are the most common source of topaz. Menzies (1995) states that about 80% of the world topaz deposits are in pegmatites (Menzies 1995).

These rocks are formed during the final stage of magma crystallization (Thomas and Davidson 2013, Soufi 2021). Pegmatites show geochemical and structural characteristics that merge both igneous and hydrothermal system. (London and Kontak 2012, Soufi 2021)

Another important aspect, which makes pegmatites a particularly prized deposit, particularly for gem-quality topaz, is their tendency to grow large crystals. Most of the record topazes mentioned in section 2.3, for example, come from pegmatite deposits. Topaz in pegmatites can occur either as interstitial fillings in quartz-feldspar matrix, if the formation process is driven by melt circulation, (or, as large crystal , grown inside open cavities (miarolitic pockets in the case for hydrothermal driven pegmatitic deposits (Peretyazhko 2010, Soufi 2021).

Pegmatites represents the crystallization of the final fraction of granitic magmas ; therefore, they are rich in volatile and incompatible elements Topaz bearing pegmatites contains large abundances of Li and Be but B; Nb, Ta, , Zr, Pb, REE and Th, U (Sokolov and Martin 2007) Wise 1995, Sokolov and Martin 2007). A chemical and mineralogical zonation characterize these rocks at macro and micro scale (Ercit et al., 2005).

This compositional variability affects, obviously topaz. Topaz from the same deposit or even the same rock may present completely different chemical and structural characteristics. (Ercit, 2005; Wise, 1995). There are two main families for pegmatites: NYF pegmatites (rich in niobium, yttrium and fluorine) and LCT pegmatites (rich in lithium, caesium and tantalum). The NYF pegmatites are the more important as topaz deposits. These rocks come from low Al, A- or I- type granites. (King et al. 1997; Ercit et al 2005, Groat 2014).

We have a lot of examples of pegmatites deposits in the American continent. In the USA: Topsham in Maine; Little Three mine, San Diego, California; Moat Mountain, New Hampshire; Pikes Peak

region and Brown derby pegmatite, Colorado. In South America: Tanti pegmatite (Cordoba province, Argentina), Eastern Brazilian Pegmatite Province (Minas Gerais state, Bahia state, Brazil). Other notable topaz pegmatites are: Gross Spitzkoppe and Klein Spitzkoppe pegmatites (Namibia), Altenberg granite (Saxony, Germany), Thabeikkyin west in Mogok metamorphic Belt (Mogok, Myanmar). (Wise 1995, Thomas, 1982, Frindt and Poutiainen, 2002, Soufi 2021, Precisvalle et al. 2021)

2.4.4 Topaz rhyolites

It is called a topaz rhyolite a rhyolite formed from a magma particularly rich in F and that contains topaz crystallized from vapor-phase alteration in the post-magmatic events. (Christiansen et al. 1986) Topaz rhyolites are typical of a belt that extends from the south of the state of Montana continues, almost uninterruptedly, to the central states of Mexico. (Burt 1982, Christiansen et al. 1986, Wise 1995) These rocks originated from the Cenozoic events. Topaz grows in gas cavities in association with Mn-Fe garnet, bixbyite, pseudobrookite, specularite, quartz (Burt 1982). All the topaz rhyolites present an high contents of SiO_2 (>75%), F, Na, K, Fe and depletion of Ti, Mg, Ca and P. Additionally enrichment of trace lithophile elements has been also recorded (Li, Rb, Cs, U, Th, Nb, Ta, Sn, W, Be, etc(Burt 1982, Christiansen et al. 1986, Wise 1995). Due to the partition effects, topazes found in these rhyolites present the highest fluorine content of all topazes reported in the literature (Soufi 2021). Other occurrences of topaz rhyolites that worth to be mentioned are the Qiguling rhyolite (Hunan Province, China) and the Late Miocene Chivinar volcano (Argentina) where in turn, topaz has the lowest F contents (for rhyolite deposits). (Xie et al 2013, Gioncada et al 2014, Soufi 2021)

2.4.5 Ongonites

Ongonites are not very common topaz deposits, in fact they are mostly located in Mongolia and represent a very small percentage of the world's topaz deposits. However, they are worth mentioning here as they can be described as the Asian counterpart to the American topaz rhyolites. (Kovalenko and Kovalenko 1984, Christiansen et al. 1986)

Ongonites, or topaz-bearing quartz keratophyres, are fine grained extrusive rocks, related to rare-elements Li-F granites that occur as dikes, stocks, and lava flow. (Wise 1995) They are very similar to the above-mentioned topaz rhyolites for both structural and chemical characteristics (Turley and Nash 1980, Burt and Sheridan 1981, Christiansen et al. 1986) The typical mineral assemblage in ongonites is albite, K-feldspar, quartz, micas and topaz. Topaz can be present either as phenocrysts or as fine grains Accessory minerals are fluorite, garnet, zircon, Fe-Ti oxides, columbite-tantalite, cassiterite, Li-phosphates, pyrite, and tourmaline. (Christiansen et al. 1986, Wise 1995) Such as the American topaz rhyolites, the ongonites are rich in trace of lithophile elements like F, Li, Rb, Cs, Nb, Ta, Be and poor in Zr, Ba, Sr. However, unlike topaz rhyolites, these have a relatively low concentration of REE (Kovalenko et al. 2004, Christiansen et al. 1986)

Ongonites occur generally in Mongolia like in Ongon Khairkhan (central Mongolia) (from where they are named after) and in Daurian region in Russia (Ary-Bulak ongonites). (Kovalenko et al. 2004, Vladykin 1983, Christiansen et al 1986, Soufi 2021) Ongonites are also associated with tungsten and other types of rare metal mineralization (like molybdenum and lithium; Christiansen et al 1986, Wise 1995).

2.4.6 Topazites

Korteimer and Burt (1988) in their work showed how topazites and ongonites are somehow related and differs from the HF concentration in magma during crystallization. (Korteimer and Burt 1988, Wise 1995) Topazites are fine-grained, intrusive rocks that are composed by 30% topaz and 70% quartz. These are the most F-enriched topaz bearing rocks, but topaz is always present as microcrystals (Korteimer and Burt 1988, Wise 1995, Huang et al. 2015, Soufi 2021) Accessory elements in topazites are wolframite, fluorite, muscovite, and tourmaline. (Wise 1995) The origins of topazites are still not fully understood today. Soufi (2020) in his work distinguishes between arguments in favour of the magmatic origin of topazites and those in favour of the hydrothermal origin.

The arguments in favour of magmatic origin are:

1. A gradual fluorine enrichment that follows the magmatic differentiation from associated rocks (Soufi 2021)
2. Feldspar is probably absent because of the inhibitory effect of high fluorine content in the melt (Veksler and Thomas 2002, Soufi 2021)
3. The separation of immiscible alkali-fluoride melts and alkali-halide fluids exsolutions, that leads to alkali elements loss (Kortemeier and Burt 1988, Soufi 2021)
4. The above-mentioned ongonites topazites transition in spatially related deposits (Kortemeier and Burt 1988, Huang et al 2015, Soufi 2021)
5. Crystallization temperatures (Eadington and Nashar 1978, Soufi 2021)

The arguments in favour of hydrothermal origin are:

1. Abundance of alterated topaz with replacement textures (Harlaux et al 2017, Soufi 2021)

2. Chemical compositions changing through different degrees of alteration (Liu et al. 1999, Soufi 2021)

Notable topaz deposits are Torrington and Mount Gibson topazite (Australia), Yanbei complex (Jangxi province, China), Xianghualing tin district (Hunan province, China). (Johnston & Chappell 1992, Zhengjun et al. 2018, Soufi 2021)

2.4.7 Vein-type deposits

In this kind of deposits topaz occur as clusters in void within calcite or quartz veins intercrossing calcareous or siliceous metasedimentary rocks. (Wise 1995) The formation of these deposits is related to pneumatolytic process in the final stages of granite crystallization. (Wise 1995). Low fluorine topaz are typically found in these deposits. Besides topaz, quartz kaolinite, euclase, muscovite and orthoclase form the common mineral paragenesis. (Soufi 2021)

In the Brewer gold deposit in South Carolina (USA) hydrothermal vein type deposits have been find in the argillitic alteration zone. (Ayuso et al. 2005, Soufi 2021)

The most famous vein-type deposit is the Ouro Preto mine in the Minas Gerais state (Brazil). Imperial topazes are typical of these deposits. Other vein-type deposits are the Katlang mining areas (Mardan district, Pakistan), Sanarka river deposits (Chelyabinsk Oblast, Russia). (Wise 1995, Soufi 2021)

3. Experimental techniques and data processing

3.1 The synchrotron X-ray powder diffraction

X-ray diffraction is one of the most widely used techniques for the characterisation of different crystal structures, both synthetic and natural.

This type of technique, which can be performed on both single-crystal and powdered samples, is fundamentally based on the principle of diffraction described by W.H. and W.L. Bragg in 1913 that is referred to as Bragg's Law. If a certain electromagnetic wave is directed towards a lattice of atoms with a periodic structure, it will act as a source of spherical waves which will give rise to constructive interference phenomena and thus produce a certain number of diffracted waves. Bragg's Law describes the direction taken by the waves produced and can be described as:

$$m\lambda = 2\,d\sin\theta$$

Where: m is an integer indicating the order of the diffracted wave, λ is the wavelength of the chosen electromagnetic wave, d is the distance to each scattering point and θ indicates the diffraction angle.

The first to develop a methodology for powder diffraction analysis were Debye and Scherrer in 1916. To date, all classical powder diffractometers have a structure that can be summarised as: an X-ray tube (a cathode tube for producing electrons by heating metal filaments), a sample holder (base or capillary, which may or may not be rotating), and an X-ray detector.

In the last twenty years, however, the use of non-conventional sources as alternatives to the classic cathode ray tube has become increasingly popular. The most widely used is the synchrotron light source. What makes the synchrotron light source more efficient than more traditional methods are,

for example, its high brilliance - the parameter that defines the intensity of the radiation and the beam - and the possibility of obtaining precise beam collimation (Figure 6).

In addition, which is not possible with classic X-ray tubes (where a given source metal corresponds to a given wavelength), the synchrotron source allows a monochromatic wavelength to be selected that is as appropriate as possible for the type of material being analysed. All these features make this analytical technique very versatile and above all provide a high resolution of analysis. This can be further enhanced by the use of monochromators, Soller slits or analyser crystals.

This results in tighter peaks, more accurate positions, and a better signal-to-background ratio. In addition to these characteristics of the instrument, it is also possible to carry out in situ experiments. By in situ experiments we mean those experiments in which the environment in which the sample is located is subjected to changes in temperature (both low and high temperatures) or other changes that may lead to modifications in the crystalline structure of the object under examination. This is useful because it allows any changes to be observed in real time, during data collection, so that changes in symmetry, changes in angles and bond lengths, possible loss of elements, etc. can be recorded and linked to certain environmental conditions. (Staron et al. 2011).

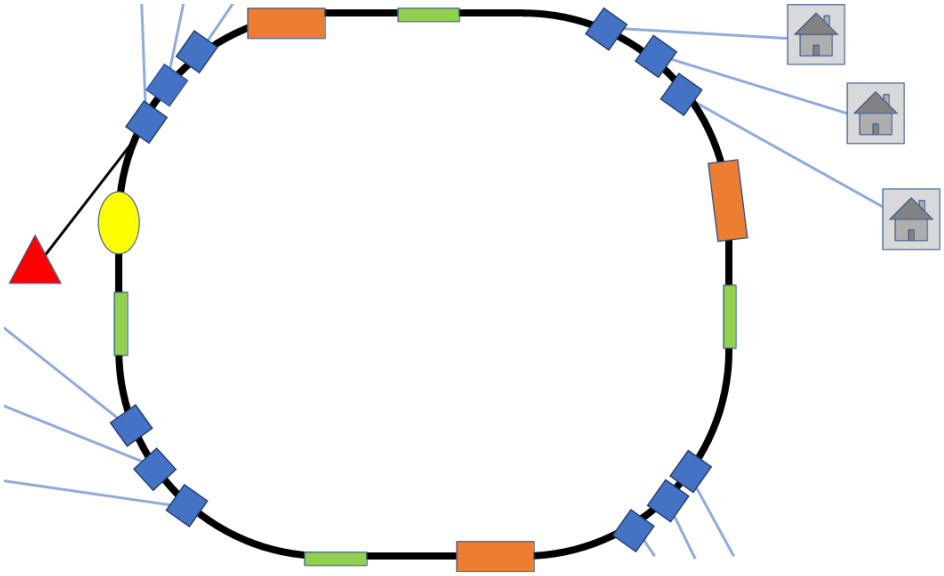

Figure 6. Schematic sketch of the synchrotron radiation source. In red, it is represented the electron gun, where the electron beam start; from here please read the sketch clockwise. In blue, the bending magnets, which direct the light to the beamlines. In orange, the undulator or the wiggler, installed on the straight portion of the ring. In green, the focusing magnet. The grey houses are the beamlines where instruments are installed. In yellow, the RF cavity that provide the energy boost for the energy loss compensation. The black path represents the storage ring.

3.1.1 Padre Paraíso topaz experimental

The powdered PadPar topaz were poured into a thin-walled boron capillary (diameter 0.5 mm) and then collected in transmission geometry (monochromatic wavelength of 0.827 Å (15 keV) and 1x0.3 mm^2 spot size at the MCX beamline (Rebuffi et al. 2014, Plaisier et al 2017) of Elettra - Synchrotron Trieste, (Italy). They were then mounted on a standard goniometric head and spun during data collection. Powder diffraction patterns were collected in 10° - 65° 2θ range with a step size of 0.008° and an exposure time of 1 s.

Each sample was subjected to the same heat treatment; samples were heated from room temperature to 1273 K with a heating rate of 5 K/min using a hot gas blower directing a hot air flux onto the spinning quartz-capillary. Diffraction data were collected every 50 K. The temperature was

continuously measured by a thermocouple and calibrated using the quartz thermal expansion and phase transition.

3.1.2 Baoshan topaz experimental

The Baoshan topaz powdered samples were poured into a thin-walled boron capillary (diameter 0.5 mm) and then collected in transmission geometry (monochromatic wavelength of 0.827 Å (15 keV) and 1x0.3 mm2 spot size at the MCX beamline (Rebuffi et al. 2014, Plaisier et al 2017) of Elettra - Synchrotron Trieste, (Italy). The same experimental procedure described for Brasilian topazes was adopted (see previous chapter, section 5.2.1). Also in this case, powder diffraction patterns were collected at the MCX beamline of Elettra—Synchrotron Trieste, (Italy) in transmission mode, from room temperature to 1273 K with a monochromatic wavelength of 0.827 Å (15 KeV) and 1x 0.3 mm2 spot size (10°- 65° 2θ range, step size of 0.008°, exposure time of 1 s). The samples were heated with a rate of 5 K/min using a hot gas blower directing a hot air flux onto the spinning quartz-capillary. Diffraction data were collected every 50 K. The temperature was continuously measured by a thermocouple and calibrated using the quartz thermal expansion and phase transition.

3.2 The neutron powder diffraction

Neutron powder diffraction follows the same concept as diffraction explained in the previous section but using a different energy source. In this technique, it is not electrons that are sent to the sample to produce the diffraction pattern, but neutrons. These non-charged subatomic particles, first postulated by Rutherford in 1920 and later observed by J. Chadwick in 1932, have a comparable mass to protons, a magnetic moment of − 1.913 μ_b and a nuclear spin of 1/2. In a scattering experiment, incoming neutrons with incident wavelength λ_i, energy E_i and wave vector k_i interact with the sample and are detected at an angle 2θ with final λ_f, E_f and k_f. The scattering vector Q, graphically described in Figure 7, is defined as the change in wave vector : $\vec{Q} = k_i - k_f$

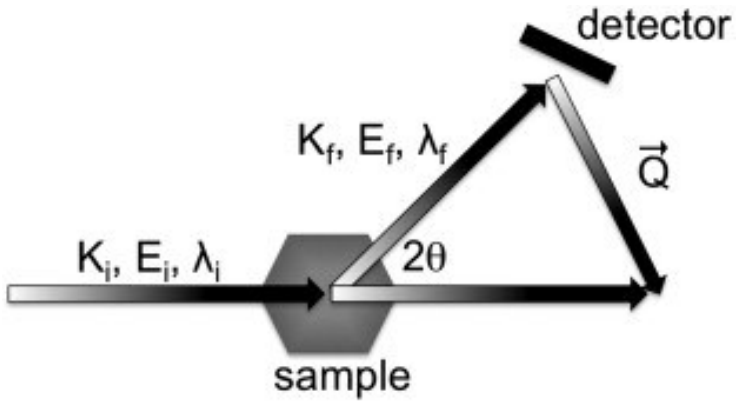

Figure 7. Schematic representation of interaction between neutron ray and the sample. Q represent the scattering vector

The major difference between X-ray diffraction and neutron diffraction is that neutrons are scattered by the nuclei of atoms and their scattering strength is independent of atomic number, momentum transfer Q and scattering angle θ.

Due to the exceptionally large scattering cross-section of the H-atoms, incoherent inelastic neutron scattering enables probing of diffusive proton motions over a broad timescale (from few nano to a few hundred ps) as well as the observation of quite high vibrational frequencies (up to 2000 cm^{-1}).

Compared to X-ray diffraction, therefore, elastic neutron scattering has two major advantages. The first is that it receives a strong scattering length from light atoms. This means that through neutron diffraction it is possible to detect the position of very light atoms, particularly hydrogen, which is why it is widely used on hydrated mineral samples, particularly synthetic ones. This is possible because neutron scattering depends on the properties of the nuclei, and therefore both heavier and lighter atoms are detectable, also giving the possibility of discerning them from neighbouring atoms (e.g., those with a similar atomic number Z) and isotopes of the same atom. The second is that the form factor does not change with the scattering angle θ (Jin, 2013). Furthermore, by using polarised neutron beams and exploiting the phenomenon of magnetic coherent scattering, neutron diffraction allows the determination of the ordered arrangement of magnetic spins within an ordered crystallographic lattice (magnetic structure). Additionally, neutrons penetrate deeply into matter, which allows for the study of structure and dynamics of materials under very precise environmental conditions such as pH, pressure, temperature, hydration and others, providing information not easily accessed by NMR, optical microscopy, light scattering, X-ray diffraction or X-ray absorption spectroscopy. The wavelength of neutrons being in thermal equilibrium with the moderator has a Maxwellian distribution, and one can further describe the neutrons based on their energy as hot ($T \approx 2300$ K, $E \approx 200$ meV), thermal ($T \approx 300$ K, $E \approx 26$ meV) or cold neutrons ($T \approx 25$ K, $E \approx 2.5$ meV). Typically, experiments like single crystal, powder diffraction and stress analysis are carried out with thermal neutrons. Experiments on dynamics (time-of-flight, backscattering and spin echo), reflectometry, tomography and small angle neutron scattering are performed using cold neutrons (Figure 8)

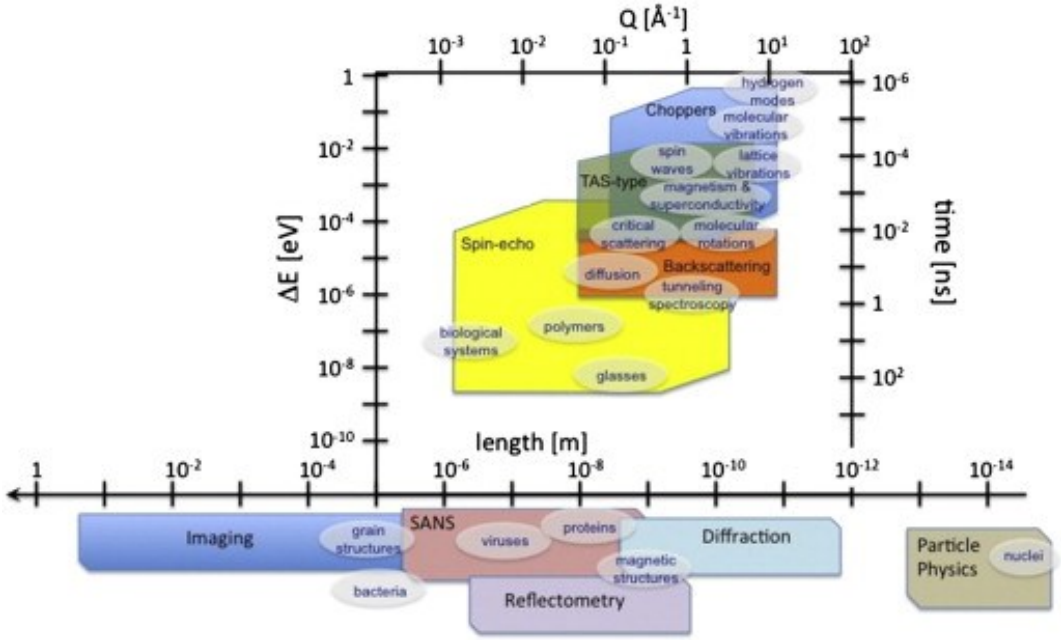

Figure 8. Using neutrons and complementary techniques to explore different length and time scales. The horizontal axes indicate real and reciprocal length scales, while the vertical axes refer to time and energy scales. Scientific areas falling within different length and time scales are indicated along the edges. The experimentally accessible areas of the various neutron-based techniques are shown as polygons in strong colors. Those techniques that are sensitive to both time and length scales are represented above the main horizontal axis; those that measure only length-scales below. In addition to the neutron-based techniques, the analogous areas for a selection of complementary experimental techniques are shown in gray (From Martins et al. 2014)

3.2.1 Padre Paraíso experimental

Neutron Powder Diffraction (NPD) experiments were then carried out on the high-flux two-axis neutron powder diffractometer D20 at the Institut Laue Langevin (ILL, Grenoble, France) using the same topaz sample. Useful data were collected between 6 and 142 degrees, of which 22 to 142 degrees were treated as follow. The samples were heated *in situ* under flowing gas (5% H_2/He), from room temperature to 1273 K (heating rate 2 K/min). Data sets were collected for 2 minutes, thus covering 4 K. A wavelength of 1.54 Å was chosen, from a germanium-(115) monochromator at 90° take-off angle. The sample was poured into a 4 mm diameter vanadium cylinder, placed in the centre of the

furnace's vacuum vessel and heated by a 30 mm diameter vanadium resistor (Martucci and Hansen 2019). A type-K thermocouple was located in the centre of the furnace in order to calibrate the temperature. The same configuration was maintained during all data collection.

A set of diffraction patterns were obtained with this procedure as a function of temperature.

3.2.2 Baoshan topaz experimental

As far as concerns NPD experiments, also in this case were neutron data collection was carried out at the high-resolution two-axis neutron powder diffraction beamline D20 of the Institut Max Von Laue-Paul Langevin (ILL) with a wavelength of 1.54(1) Å (a germanium-(115) monochromator at 90° take-off angle).The samples were heated *in situ* under flowing gas (5% H_2/He), from room temperature to 1273 K (heating rate 2 K/min, 2theta range: 6-142°). The sample was poured into a 4 mm diameter vanadium cylinder, placed in the centre of the furnace's vacuum vessel and heated by a 30 mm diameter vanadium resistor (Martucci and Hansen 2019).

3.3 Scanning electron microscope (SEM)

The scanning electron microscope is an instrument that allows the surface microstructures of the samples under analysis to be studied through images. Using a high-energy beam that is fired at the sample, the SEM allows to visualise all those peculiarities that the human eye alone cannot grasp even with the use of an optical microscope (Ul-Hamid, 2018).

SEM consists of three main elements: the electron column, the sample chamber and hardware – software as station for controlling system. Inside the column is the electron gun which has the function of generating the electron beam. Also here, a system of lenses concentrates the electrons in a beam of few nanometres in diameter, so that it can be focused on the parts of interest in the sample. The entire electron column-sample holder system is kept under high vacuum. The necessity of keeping the system under vacuum is to avoid backscattering phenomena. The electron beam penetrates the samples for a few microns, interacting with the atoms that compose it and generating different response signals such as secondary and backscattered electrons, then the characteristic responses of the x-rays are collected and processed in order to obtain an image of the sample surface. The interactions between the electron beam and the samples can be elastic and inelastic. In the elastic scattering, electrons are deflected at very wide angles with very little energy transfer from the electrons to the nuclei. High-angle elastic scattering is more likely to occur with heavy atoms. Electrons that are elastically scattered at angles greater than 90° are referred to as BSE or backscattered electrons. (Zhou et al. 2006, Ul-Hamid 2018)

Inelastic scattering, on the other hand, occurs when the electrons in the beam interact with the sample in such a way that there is a loss or transfer of their kinetic energy to the nuclei of the sample atoms. In this case, of course, the electrons are deflected at a low angle. The excitation created by the collision of the electrons from the beam and the resulting ionisation of the atoms leads to the formation of secondary electrons, which are essential for the creation of the image (Figure 9). (Zhou et al. 2006, Ul-Hamid 2018)

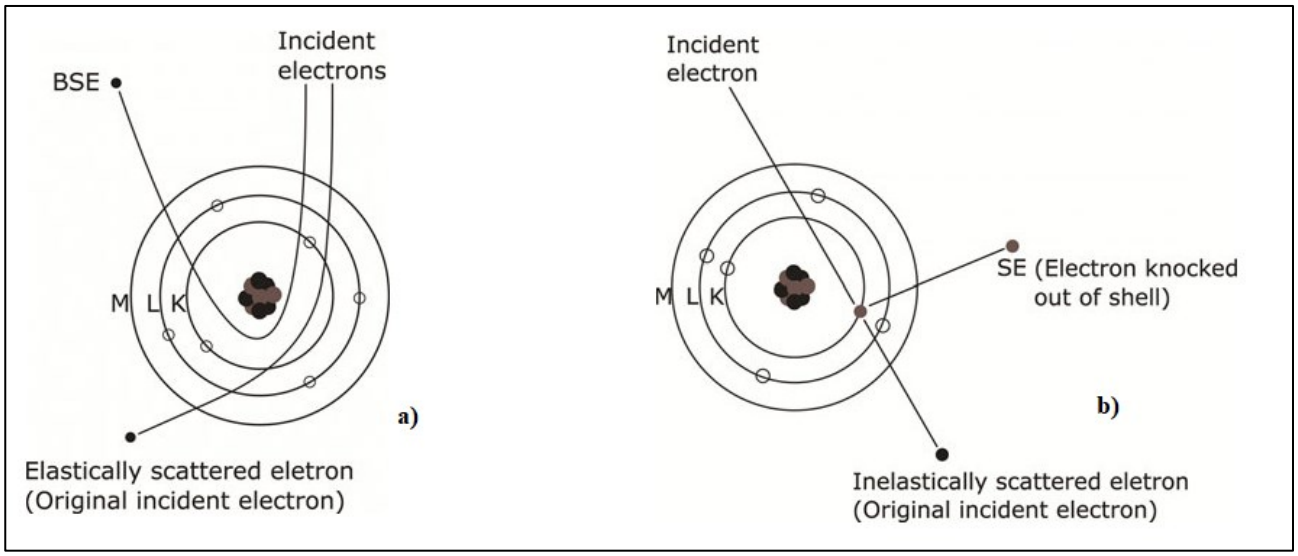

Figure 9. Sketches of electron scattering. In a) it is represented the elastic scattering, with the backscattered electron and the elastically scattered electron. In b) it is represented the effect of inelastic scattering and the formation of a secondary electron. (Modified From Ul-Hamid 2018)

3.4 The Energy Dispersive X-ray Analysis/Spectroscopy (EDS)

Energy dispersive X-ray analysis, or energy dispersive X-ray spectroscopy, is a technique widely used in combination with SEM to obtain information about the chemical composition of the observed sample (Zhou et al. 2006, Ul-Hamid 2018). Indeed, by integrating an EDX detector, it is possible to obtain the point composition of the selected portions of the sample whose image was obtained by SEM. This type of detector is usually integrated with the electron column. The function of EDX is to detect and identify the response of various elements in terms of their X-ray energy and wavelength. Although in the latest generation of EDX systems the detection limit is around 0.2 wt.%, the quantitative use of this technique is not recommended for the detection of trace elements (with a concentration below 0.1 wt.%) and used with extreme caution when investigating minor elements (<1wt.%) (Ul-Hamid2018).

This is because the accuracy of the analysis is directly related to the concentration of the elements in the sample. Regardless of their concentration, the detection of light elements helium, lithium, beryllium and boron is often impractical or very difficult.

The EDX detector uses the X-ray signal formed by the characteristic response of the interaction between the x-ray of the beam and the atoms of the sample together with the white radiation, i.e., the background x-rays, to characterise the concentration of the elements. The result of this analysis will be a spectrum in which the different peaks that can be traced back to the elements that make up the selected investigation zone can be recognised.

Usually, to verify that peak positions are reliable and that they are accurately attributed, EDX is calibrated by analysing pure metal plates such as nickel (Ul-Hamid 2018). Once the identification of the elements has taken place, it is possible to obtain their degree of concentration and thus a quantitative analysis. Quantitative EDS analysis can be obtained after the use of standards, which is more accurate but slower, or without the use of standards.

Quantitative analysis using standards consists of analysing, before and during the analysis of the sample under study, a standard sample whose composition is known. Obviously, in addition to being known, it is necessary that the composition is as close as possible (if not the same) to that of the sample being analysed. The spectra obtained from the standard sample will then be compared with those produced by the unknown sample.

The solution without a standard is faster but slightly less accurate. In this case, only the unknown sample is analysed. In a second step, the spectra obtained are then compared with spectra of previously analysed samples or contained in special databases. (Ul-Hamid et al. 2018)

In any case, for this analysis to be successful, it is important that the sample analysed has a good degree of smoothness and flatness. In addition, non-metallic samples, such as the silicates analysed in this thesis, should be subjected to a metallisation process (e.g., with carbon or gold).

3.4.1 Experimental

For this study, both populations were analysed with a CAMSCAN MX 2500 Scan Electron Microscope (SEM) with an EDAX system for Energy Dispersive Analyses. The SEM was equipped with a high brightness LaB6 cathode, operating in a high vacuum. The samples were coated with carbon. For quantitative purposes, a set of natural minerals was used as standards for their specific elements: augite (Si and Ca), fluorite (F), gahnite (Al) and olivine (Mg, Fe). Relative analytical errors (1σ) of major elements were below 1.00% for Si and for Al; and 3.00–6.00% for F.

Images were collected both in SEI (Secondary Electron Imaging) and BEI (Backscattered Electron Imaging). The parameters used for the analyses were EHT 20kV, EMI 71μA, FIL 1.80A with a working distance of 25mm. Imaging and measurements were performed at the Microscopy Laboratory of the University of Padua.

3.5 Laser Ablation - Inductively Coupled Plasma Mass Spectrometry

Laser Ablation- Inductively Coupled Plasma Mass Spectrometry (LA-ICP-MS) is a technique used for in-situ quantification of minor and trace elements in solid state samples. The LA-ICP-MS consists of four parts: the laser for the high energy photons beam, the laser beam delivery system and optics to modulate the laser, an ablation cell where the sample is positioned, the sample transport system that transfer the ablated ionized aerosol to the ICP-MS (Figure 10). (Kosler, 2007)

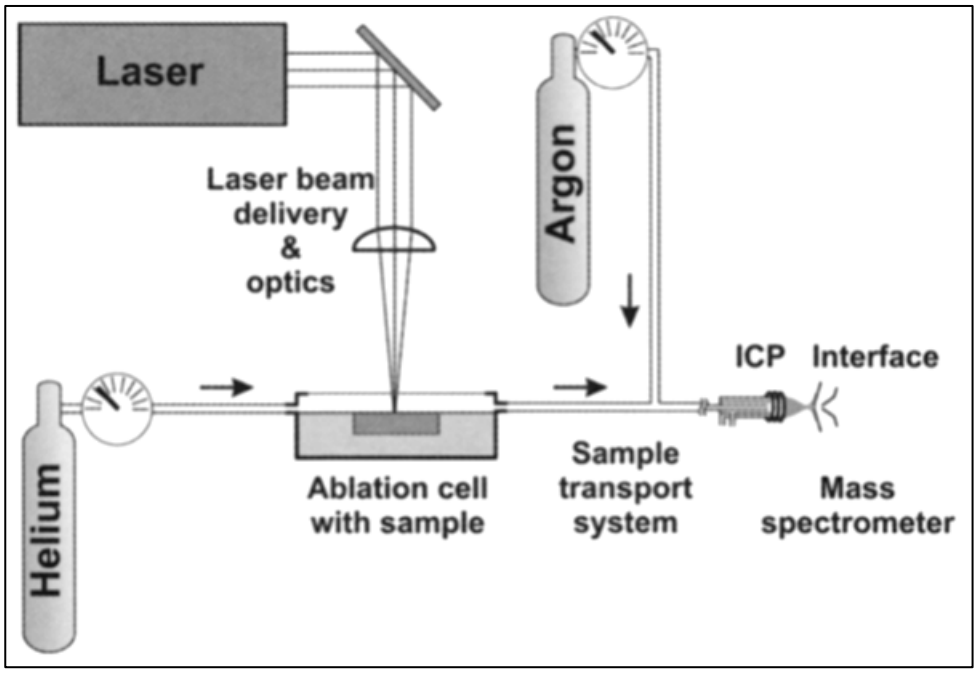

Figure 10. Schematic representation of the LA-ICP-MS system. (Modified from Kosler, 2007)

Laser sampling uses the interaction between the solid sample, a mineral or section of rock, and photons fired at high intensity. The laser then erodes the sample, and the sample is vaporised, vaporisation results in the ejection of atoms, ions and particulate matter. (Darke & Tyson, 1993; Durrant, 1999; Kosler 2007)

The most commonly used lasers for this type of analysis are those that exploit the amplification of light within a gaseous or solid-state medium. To date, the most common are solid-state lasers, particularly those made of yttrium-aluminium garnet with neodymium (Nd:YAG) added. (Kosler 2007) As mentioned above, the laser is sent to a sample contained within an ablation cell. A microscope is often associated with this mechanism to make the technique more focused, precise and therefore more effective for the chemical mapping. It is important that the aerosol that is formed is transported efficiently to the ICP-MS system so that the signal is maintained at a good and stable intensity. To do this, carrier gases are blown into the cell, which can be "pure" such as He or in mixtures such as Ar-N_2 or Ar-He. (Kosler, 2007)

The aerosol is then transformed into a plasma by being subjected to temperatures of up to 10000 K by the ICP plasma torch. The mass spectrometer usually uses a quadrupole mass analyser. Ions are separated according to their mass-to-charge ratio and a signal proportional to concentration is produced. The concentration can be determined by calibration with standards.

The great advantage of a laser system combined with mass spectrometry is first of all the ease with which the sample can be prepared, as it does not require any preparation other than a brief polishing. The other advantage is that the technique is micro-destructive, leaving only a few micron-sized holes in the analysed sample; This is why it is widely used in large gemmological laboratories. This, together with the rapid response and ability to measure concentrations down to ppb (parts per billions), makes the LA-ICP-MS one of the most versatile instruments for studying trace elements.

3.5.1 Experimental

The chemical characterization for trace elements for both populations has been obtained by mean of LA-ICP-MS. In order to carry out in situ chemical analyses of the samples a section had to be made. The obtained thin cross-sections generally have a thickness of 0.4 cm with an average diameter of 1 cm. Raw samples has been polished with a diamond disk and then with diamond suspension. The sections have been prepared at the Sample Preparation Lab at University of Ferrara. Trace elements were analysed by (LA-ICP-MS) using an Agilent 8900 Triple Quadrupole ICP-MS, coupled to a GeoLas200 Microlas Eximer laser with a wavelength of 193nm using an ArF gas. The measurements have been carried out at the IGG (Istituto di Geoscienze e Georisorse) – CNR (Centro Nazionale delle Ricerche), Pavia (Italy). The spot size was 50 μm. Fluorine combined with argon was a carrier gas and ablation have been carried out with a pulse rate of 10 Hz and an energy density of 8 J/cm2. The LA-ICP-MS data collection have provided 60 s of background acquisition followed by 70 s of

ablation. The software GLITTER 4.0 has been used for data reduction with NIST 610 and NIST 612 as primary external standard, BCR – 2g as second external standard and Si29 as internal standard.

3.6 TwinMic: Soft X-ray Transmission and Emission Microscope

Advances in microscopy techniques based on X-rays have opened unprecedented opportunities in terms of spatial resolution, combined with chemical and morphology sensitivity, to analyze solid, soft and liquid matter. The TwinMic X-ray Spectro microscope is a unique instrumentation belonging to the beamline of the same name which is part of the Elettra synchrotron in Trieste (Italy). This instrument combines full-field imaging with an X-ray microscope. This instrumental setting presupposes the use of two X-ray microscopy methods: transmission X-ray microscopy (TXM) and scanning transmission X-ray microscopy (STXM).

The TXM microscopy technique works very similarly to classic visible light microscopy. Obviously in this case the source that allows the surface of the sample to be viewed is not visible light, but an X-ray beam. It has a high spatial resolution, allowing a good portion of the sample to be enlarged, and operates in a very short time. This makes TMX a preferable technique when monitoring morphological changes in the sample over short periods of time.

A condenser with zone plate optics illuminates the sample while a lens in the lens enlarges the image, which is collected by a CCD-type detector (Figure 11). (Gianoncelli et al. 2021, Adams et al. 2015)

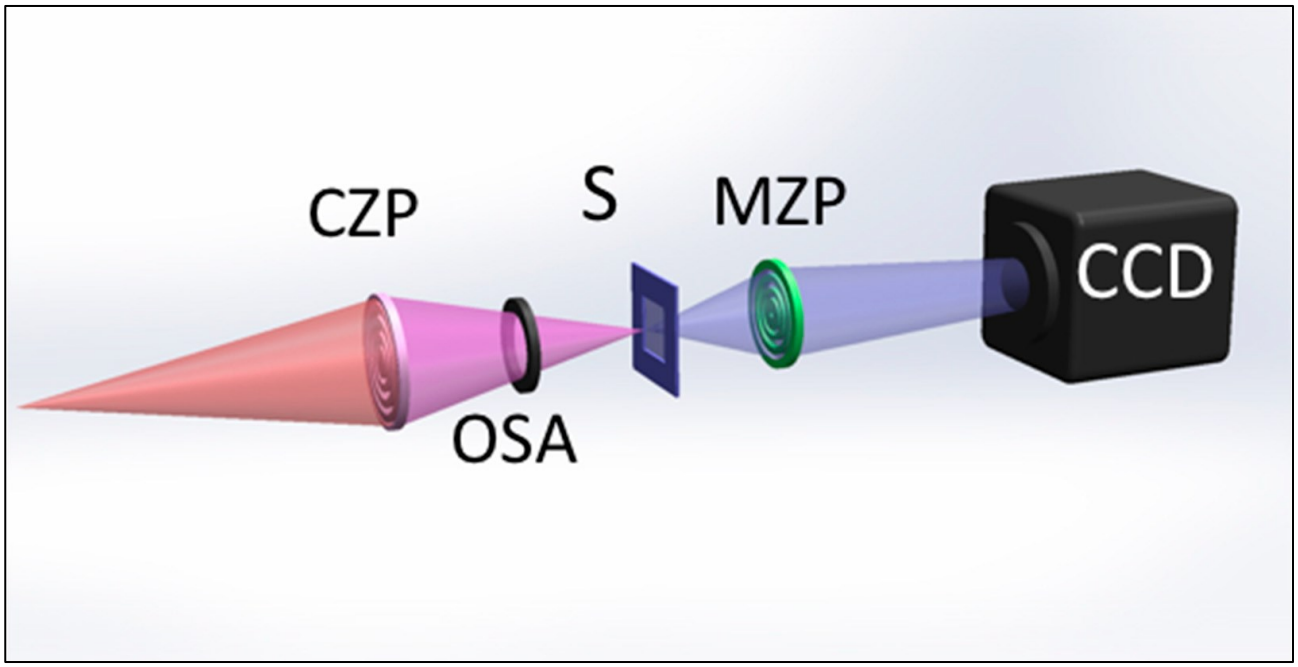

Figure 11. Schematic representation of the TMX setup at TwinMic. The zone plate condenser (CZP) focalize the beam and illuminate the sample (S, in blue), through an order selecting aperture (OSA, in black). The image is then magnified by means of a micro zone plate (MZP, green). In the end the signal is collected by a CCD detector (in black). (From Gianoncelli et al. 2021)

The scanning transmission X-ray microscopy is normally used with soft x-ray or mild x-ray. It requires suitable X-ray optics, usually zone plate (ZP) diffractive optics, to focus the X-ray photons on the sample plane, where the specimen is usually scanned across the microprobe. In a few cases, the beam can be scanned across the sample. (Gianoncelli et al. 2021, Kaznatcheev et al 2007)

Since this is a technique that involves scanning the surface to be analysed, the spatial resolution will depend on the size of the probe. The x-rays transmitted for each point of the raster scan are then collected by a special detector (in the case of TwinMic detectors of the CCD, EMCCD, SDD type), which allows the absorption signal to be recorded. Since this is a technique that involves scanning the surface to be analysed, the spatial resolution will depend on the size of the probe. The x-rays transmitted for each point of the raster scan are then collected by a special detector (in the case of TwinMic detectors of the CCD, EMCCD, SDD type), which allows the absorption signal to be recorded. The instrumental setting of the Twinmic beamline uses a two-dimensional detector, which

allows to obtain a complete image of the analysed sample including an absorption image, a differential phase contrast image and a darkfield contrast image. (Gianoncelli et al. 2021, Morrison et al. 2005, Feser et al. 2006). However, this type of microscopy not only allows an image of the sample to be obtained, but also enables chemical mapping of the surface to be carried out. Through the use of dedicated detectors, it is also possible to obtain not only a scanning imaging analysis, but also the acquisition of other signals such as XRF photons and photoelectrons emitted by the sample (Figure 12) (Gianoncelli et al. 2021, Gianoncelli et al 2009). In this way it is possible to obtain not only the morphology of the sample but also the identification of the elements that compose it and their spatial distribution. The TwinMic microscope is currently equipped with a low-energy X-ray fluorescence.

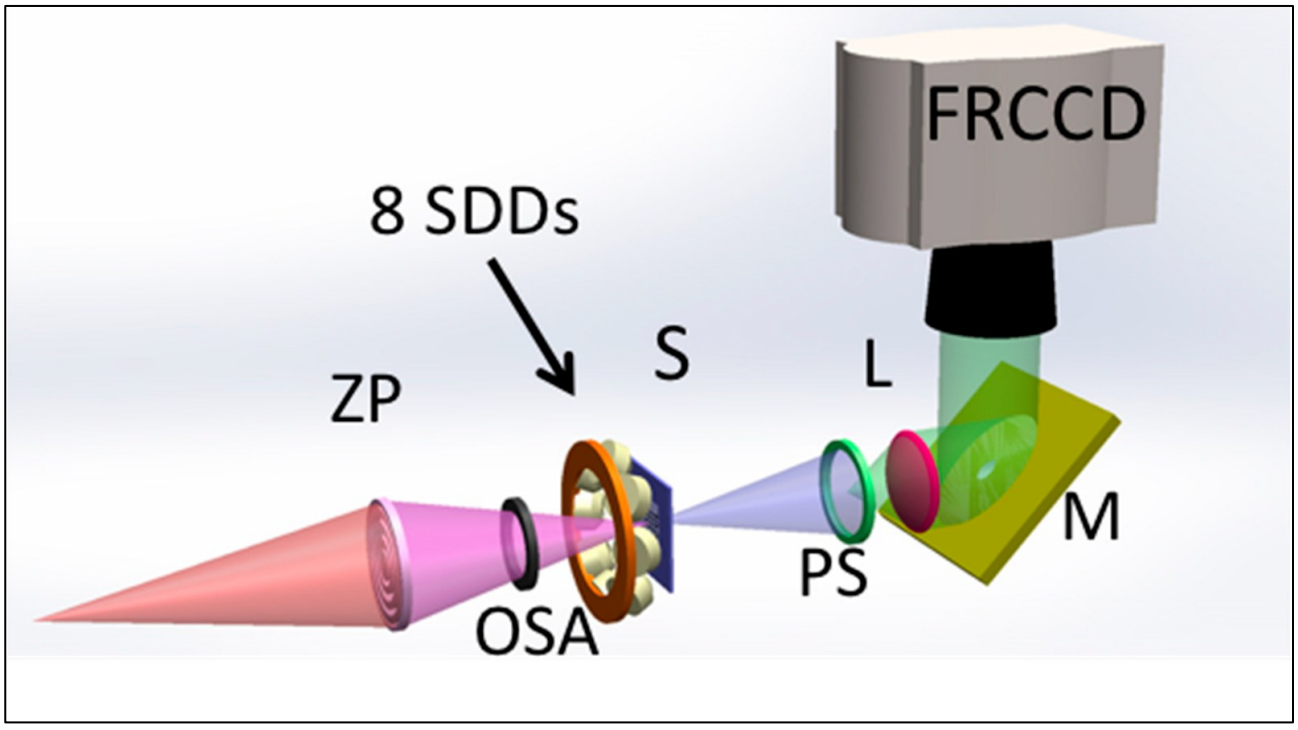

Figure 12. Schematic representation of the STXM coupled with LEXRF system at TwinMic. ZP: zone plate, OSA: diffraction order-selecting aperture, SDDs: silicon drift detectors, S: specimen, PS: phosphor screen, L: lens, M: mirror, FRCCD: transmission detection system with fast-read-out CCD camera. (From Gianoncelli et al. 2021

3.6.1 Experimental

Low energy X-ray fluorescence (LEXRF) analyses were performed at TwinMic beamline of Elettra Synchrotron Trieste (Trieste, Italy). The incident X-ray beam energy was 2 keV to ensure the best excitation and detection of the Kα lines of Si, Al, Ga, Ge, As and F atoms. The samples were raster-scanned with a step size of 0.8µm across a microprobe of 0.8µm diameter delivered by a 600 µm diameter Au zone plate optics with 50nm outermost zone. XRF maps were acquired on areas of around 76 µm x 76 µm or 72 µm x 72 µm, with 5s/pixel acquisition time and were process with PYMCA software package.

These energies of acquisition needs samples with large surface, but 5 microns maximum thickness. This condition applied on solid crystalline state is quite challenging. The sample preparation procedure has been specifically developed for this study and, as far as I know, never applied before on this material. The samples have been prepared at Centre for Electron Microscopy at Istituto Officina dei Materiali – CNR- Trieste (Italy). The samples have been prepared with the Precision Ion Polishing System (PIPS). It is based on a technique that produces discs with a diameter of 3 mm that can be thinned mechanically down to about 50 microns. The disc is then thinned in the central area (using a dimpler) to create a crater geometry with a thickness that varies from the outside to the inside (from 50 microns on the outside to 25 microns in the centre). This disc is then placed in an ion bombardment system to thin the central zone until a hole is created more or less in the centre. The thinnest zone will be the one around the hole, which has a thickness of up to 50 nm at the very edge of the hole (Figure 13 and Figure 14). The crater geometry is preserved: the thickness increases from the inside to the outside. The so-obtained samples have been mounted on a Cu TEM grid for focusing.

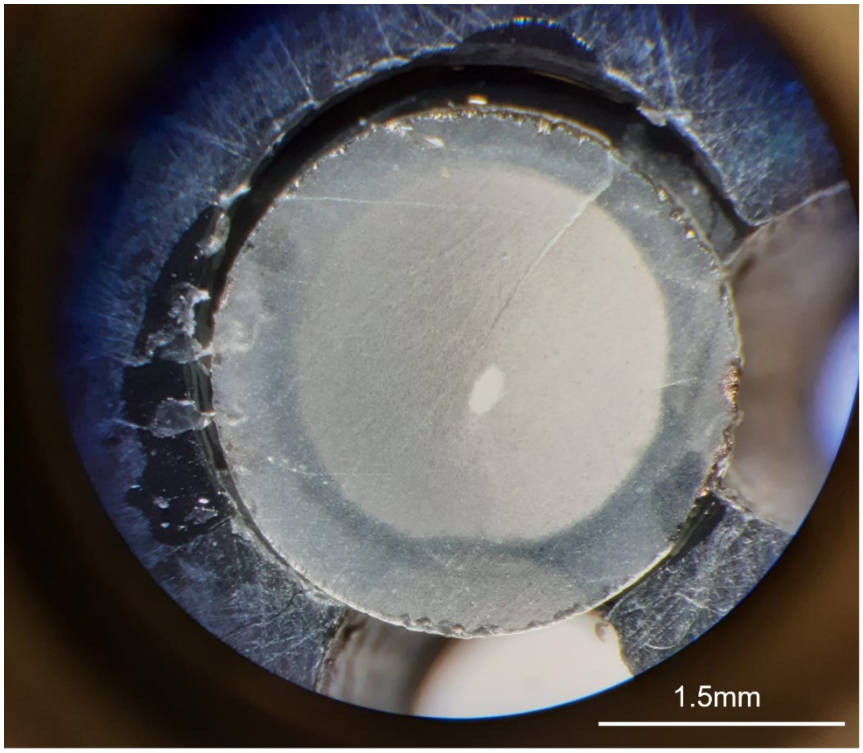

Figure 13. Padre Paraìso topaz sample prepared by means Precision Ion Milling System at CEM – IOM.

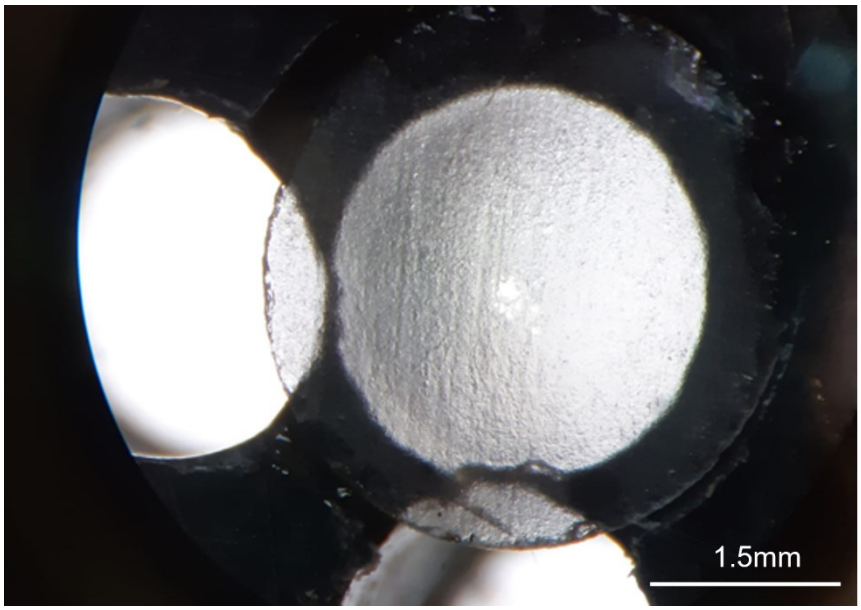

Figure 14. Baoshan topaz sample prepared by means Precision Ion Milling System at CEM – IOM.

4. Materials

4.1 Padre Paraíso blue topaz

4.1.1 Geological setting

The blue topaz crystals studied in this work have been collected in the Padre Paraíso municipality, located in the North-East area of Minas Gerais State in Brazil. From now on this topaz will be referred as PadPar. This locality is very well known for the presence of different kind of gemstones associated with the pegmatitic and the magmatic events that characterized the Eastern Brazilian Pegmatite Province. (Ferreira et al. 2005, Pedrosa-Soares 2011, Precisvalle et al. 2021).

The whole area belongs to the Late Neoproterozoic–Cambrian Araçuaí orogen, a great orogenic body that show up in the eastern part of Brazil (Pedrosa-Soares & Wiedemann-Leonardos 2000, Silva et al. 2005, Pedrosa-Soares 2011). A huge number of plutonic rocks set up this orogeny, as evidence of a long-lasting succession of granitic production events (Pedrosa-Soares 2011). In fact, the whole succession shows formations that runs from the Late Neoproterozoic (630 Ma ca.) to Cambro-Ordovician (480 Ma ca.) (Figure 15a). (Pedrosa-Soares et al. 2008, Pedrosa-Soares 2011). The pegmatitic district belonging to this orogeny form the Eastern Brazilian Pegmatite Province (EBPP) (Figure 15b). (Pedrosa-Soares 2011, Precisvalle et al. 2021) From De Campos et al. (2004) the granite that form the EBPP has been grouped in 5 different suites, characterized by different age, geochemical data and structural features called G1 to G5. Pedrosa-Soares (2011), stating the fact that suite is more suitable to a small batholith or rock bodies, decided to change the nomenclature from “suite” to “supersuite”. In this work, I will follow his wording. The blue topaz samples come from the G5 supersuite.

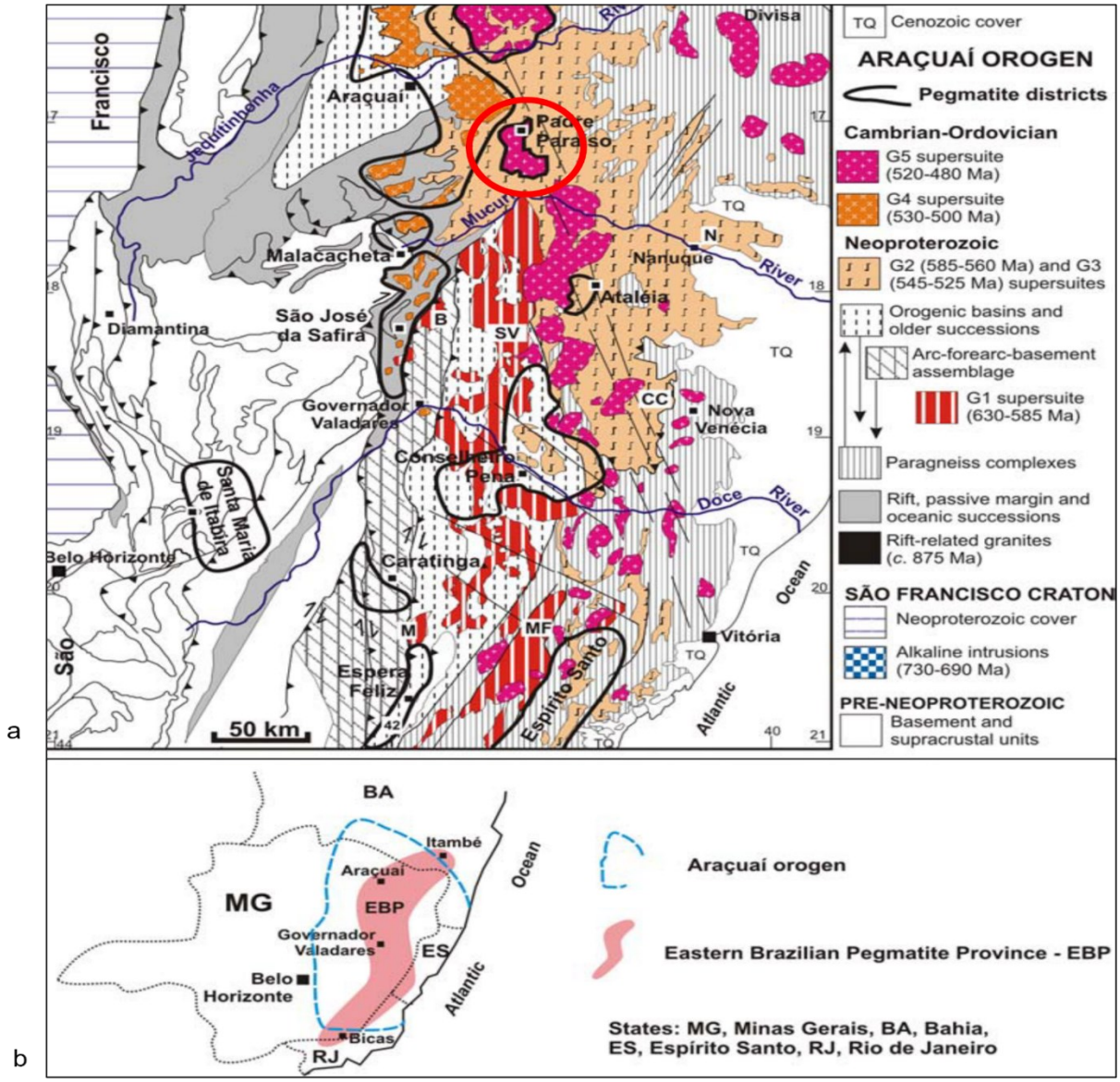

Figure 15 a, b. In a is shown a geological map of the Araçuaí orogeny with a small portion of the San Francisco Craton. The colours highlight the different supersuites that compose the EBPP. The red circle emphasises the Padre Paraìso municipality. In b is showed the extension of the EBPP in the Minas Gerais state. These maps have been modified from Pedrosa-Soares (2011).

The G5 supersuite is a magmatic event of post-collisional origin related to the gravitational collapse of the Araçuaí orogen (Pedrosa-Soares 2011, Precisvalle et al. 2021); zircon and monazite U-Pb ages and zircon Pb-Pb ages constrain the evolution of the G5 supersuite from 520 to 480 Ma. (Pedrosa-Soares 2011, Mendes et al. 2005, Pedrosa-Soares et al. 2006, Precisvalle et al. 2021) The supersuite bodies occur along the North-East part of the pre-collisional magmatic arc, following

a NE trend to the south of 208 S parallel, and NW trends to the north of this latitude. (Pedrosa-Soares 2011)

The G5 unit is a porphyritic biotite granitoid, classified as a Type-I granite that is metaluminous and K-rich (Pedrosa-Soares 2011, Precisvalle et al. 2021). Associated to the "G5 granite" is the Padre Paraíso charnockite (Pedrosa-Soares 2011, Precisvalle et al. 2021), which is a porphyritic biotite rich granitoid that has a greenish colour. Charnokites is also an important genetic indicator, in fact they are associated to high CO_2 fluid pressure indicator (Pedrosa-Soares 2011, Precisvalle et al. 2021). Its primary mineral assemblage is composed of K-feldspar, plagioclase, biotite, hornblende, and hypersthene (Pedrosa-Soares 2011, Precisvalle et al. 2021). As per the pegmatite rocks in Padre Paraìso district, they come from the residual melts of the G5 granites and are the main mineral sources. The most abundant are the so-called internal pegmatites, i.e., pegmatites that are hosted by the parent granite. (Pedrosa-Soares 2011) These pegmatites are very small to small in size, with a pegmatite size in relation to thickness from less than 0.5m to 5m. Other minerals that can be hosted by these ores are aquamarine, quartz, goshenite, chrysoberyl. (Pedrosa-Soares 2011). Most pegmatites of the Padre Paraíso districts represent residual melts crystallized inside their parent G5 granites and charnockites. These are relatively simple post collisional, I- to A2-type, high-K and high-Fe pegmatite–granite systems, emplaced in deep crustal levels (Pedrosa-Soares 2011). This iron richness is the main factor in the formation of deep-blue aquamarine crystals, and it is probably connected to the PadPar samples intense blue.

4.1.2 Sample description

The sample description applies to all the collected specimens and not only to the ones selected for this work. The Padre Paraíso topaz are all centimetric in size, from 1 to 2 cm, with irregular shape and no recognizable form (Figure 16).

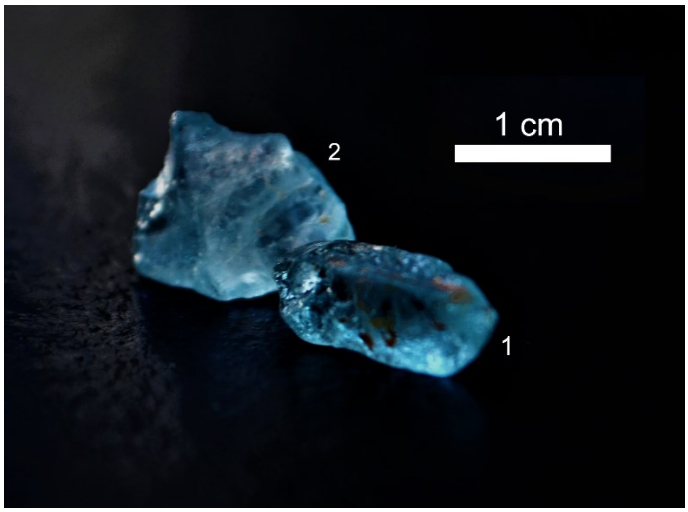

Figure 16. In the picture, the blue topaz samples from Padre Paraíso that has been studied in this work. The sample numbered as 1 is the sample further on labelled as "PadPar3", while the sample numbered as 2 is the sample "PadPar1". The image is taken from Precisvalle et al. 2021

The refractive index, measured with a bench optical refractometer, are pretty high with average values from 1.620-1.631 to 1.634-1.642. No pleochroism has been noted for any specimen and no response from the UV light both long and short. The average calculated (from immersion method) specific gravity is 3.52. These topazes present a clear to intense light blue colouration, with no fades or colour flaws in all the samples collected. All crystals have good transparency with medium-high clarity. They are very poorly to poorly included, with solid and biphasic inclusions. The solid inclusions are sporadic and are mostly represented by small quartz, micas and very rare sulphides and oxides. In PadPar3 a large yellow to orange inclusion has been identified as probable chalcedony. The biphasic inclusions are liquid/gaseous, mostly (but not all) with an elongated aspect grouped in cloud with a recognizable isorientation (Figure 17 a, b). No identification of any thermal or irradiation treatment has been recognized in the selected samples (PadPar3 and PadPar1).

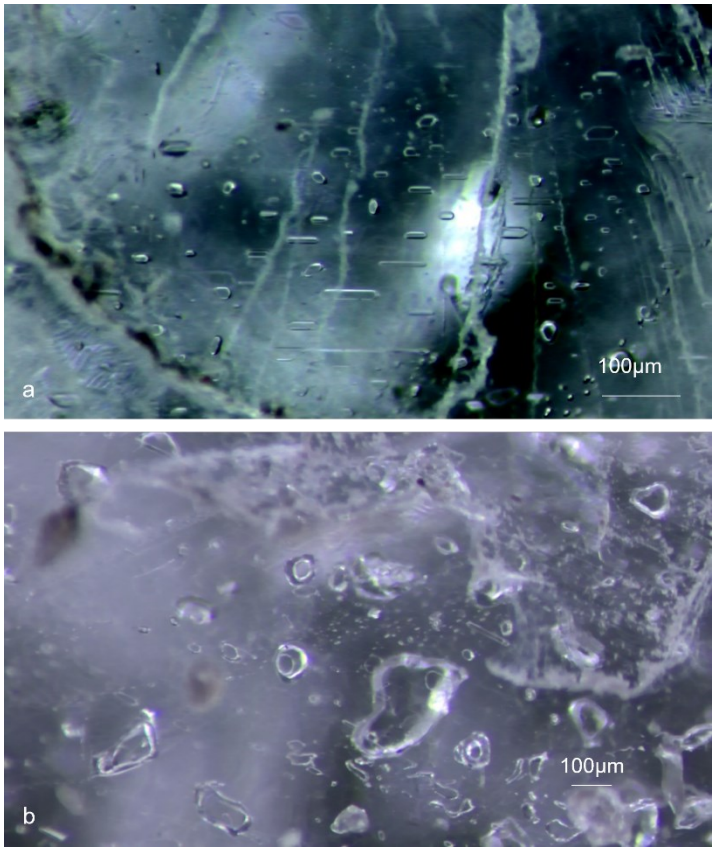

Figure 17 a, b. In this picture are given some examples of inclusion found in PadPar topaz. In figure L a are recognizable a cluster of elongated biphasic inclusion, following the same direction. In figure L b, otherwise, the biphasic inclusion are less regular in form probably because originated from crystal dissolution. It is also possible to appreciate some solid inclusion such as sulphides (black dots in the central-upper part of the photo) and a colourless crystal in the upper-left corner.

4.2 Baoshan colourless topaz

4.2.1 Geological setting

The colourless topaz studied in this work comes from the Baoshan ores area in the Yunnan province of China. From now on this topaz will be referred as Bao. The area, famous for several mineral deposits and metallogenic resource, is part of the Sanjiang region that comprehend the SE Tibet Plateau and the NW Yunnan, formed from the amalgamation of the Gondwana derived continental blocks and arc terranes as a result of oceanic subduction that occurred before the late Paleozoic tectonic events that lead to the continental collision. (Deng et al 2014) The topaz deposits in the Yunnan province are related to the Thetys Sn metallogenic domain, in particular the Tengchong-Baoshan block with its hydrothermal vein type mineralization (Figure 18).

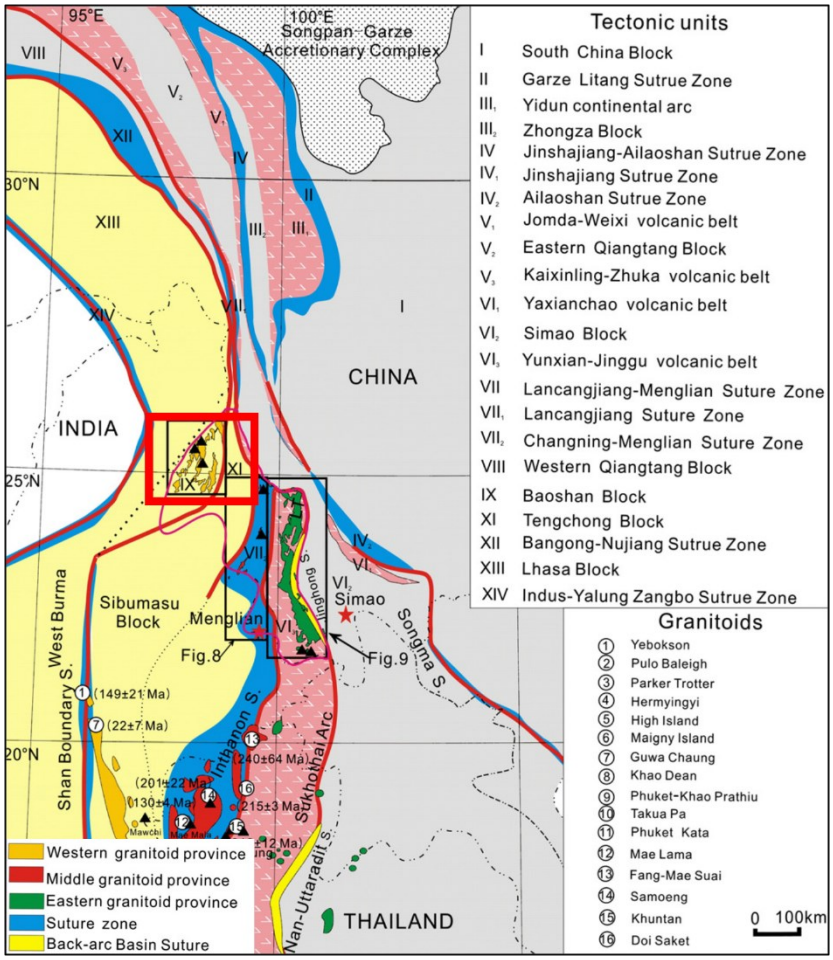

Figure 18. Geological map of the southwestern Sanjiang Tethys, with the relative tectonic units and granitoids. Squared in red, the Baoshan and Tengchong blocks. Modified from Wang et al. 2013

To the Tengchong-Baoshan block belongs the Tengchong- Baoshan granitoid province, as the last northern segment of the Sibumasu Terrane. The rocks that compose this province are mostly monzogranites and granodiorites, with minor tonalites and quartz diorites. In general, the granitoids are all members of calc-alkaline series. (Yang et al. 2006, Hou et al. 2008, Yang et al. 2009, Wang et al. 2013)

The magmatism is dominated by crustal melting (S-type granitoids) with an age that ranges from Early Cretaceous to Late Cretaceous/Early Cenozoic. (Wang et al 2013) The Early Cretaceous granitoids are the results of several episodes of crustal melting that happened during the west Burma - Tengchong-Baoshan blocks collision. (Tao et al. 2009, Yang et al. 2009, Wang et al. 2013) On the other hand, the Late Cretaceous/Early Cenozoic granitoids derived by the mantle wedge partial melting during the crustal thickening related to the subduction of the Neo-Tethyan plate subsequent the Indian – Asian plates collision (Yang et al. 2006, Hou et al. 2008, Yang et al. 2009, Wang et al 2013). The Tengchong-Baoshan granitoid province host one of the richest group of ores in the world, and one of the primary sources for gemstones in China (the Tengchong-Baoshan Sn-polymetallic metallogenic belt). In Tengchong and Baoshan there are eight principal metallic deposits, bearing Sn, Nb, Ta and Li (besides hundreds of smaller mineralization) (Hou et al. 2008, Wang et al. 2013). The deposit types are several, but all related to low metamorphization due to hydrothermal fluids. The most important deposits are: Dadongchang, Tiechang and Shiganhe that are hydrothermal vein type Sn deposits (Hou et al. 2008. Li et al. 2009, Wang et al. 2013); Baihuanao, Xiaolonghe, Dasongpo and Lailishan that are Greisen type deposits (Li et al. 2009, Wang et al 2013); Diantan is the only skarn type Sn deposits. (Dong et al. 2005, Wang et al 2013)

4.2.2 Sample description

The sample description applies to all the collected specimens and not only to the ones selected for this work. The Baoshan topaz arrived in different shape and size. They run from small chips from 0.5 to 1 cm to bigger euhedral samples circa 3cm x 2cm. The refractive index, measured with a bench optical refractometer, have average values from 1.615-1.618 to 1.626-1.627. The average calculated (from immersion method) specific gravity is 3.50. No pleochroism has been noted for any specimen and no response from the UV light both long and short. These topazes are perfectly colorless, with no pale-yellow shades. All crystals have a good transparency and high clarity. They are very poorly included, with solid and biphasic inclusion and sometimes radiated internal fractures. The solid inclusions are predominant, the most recognizable are tantalite, quartz, tourmaline, oxides and sulphides (which species has not been determined) (Figure 19). Tourmaline, in its variety elbaite, is present in Bao1 growing along an internal fracture (Figure 20). The biphasic inclusions are liquid/gaseous. No identification of any thermal or irradiation treatment has been recognized in the selected samples.

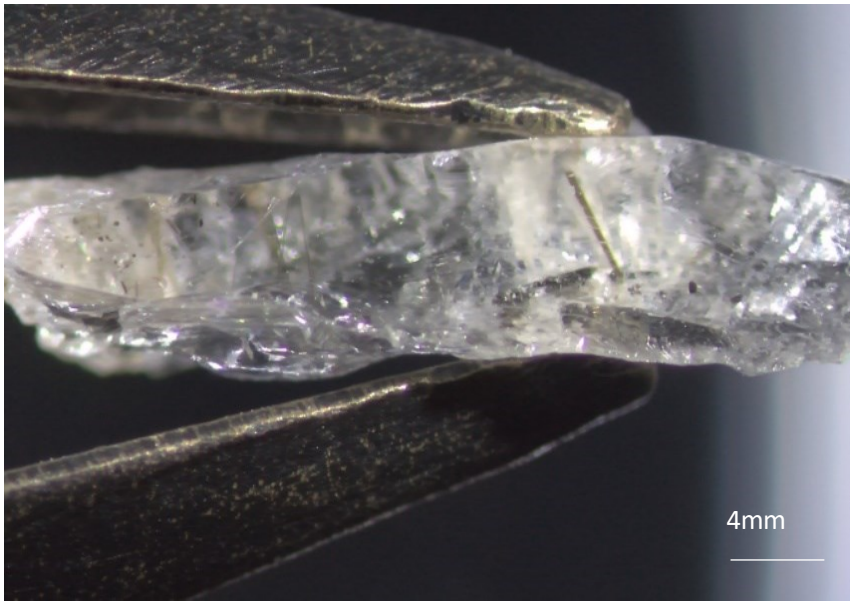

Figure 19. A specimen of Baoshan topaz, an olive-green tourmaline can be seen between the clips. On the left part a cloud of small oxides crystals is visible.

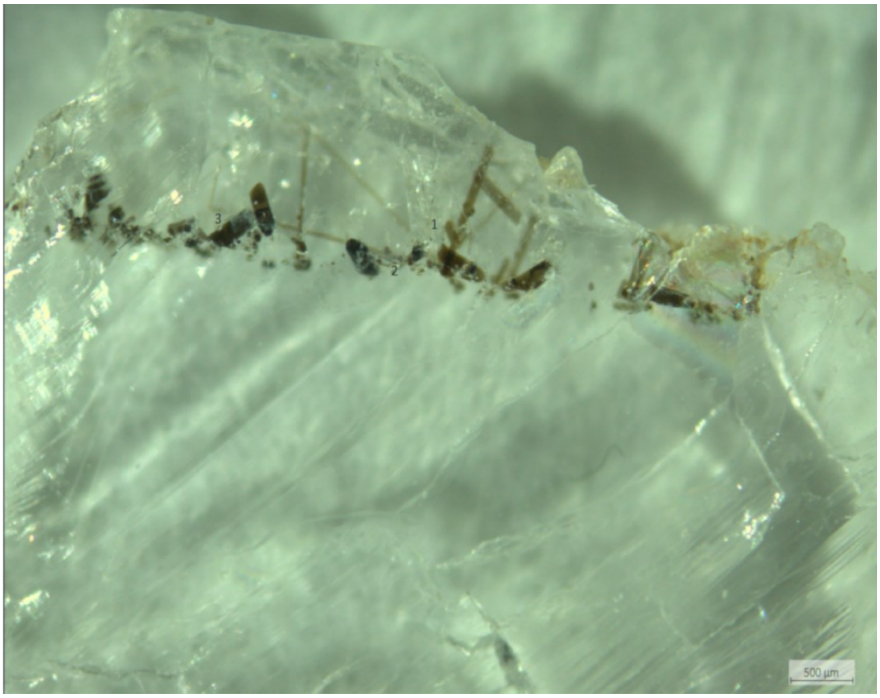

Figure 20. The isorientated tourmaline in Bao1 sample.

5. Results

This section presents the results of the analysis of the reference samples. I have decided to present them separately for the two populations, despite the same analytical procedure. Some of the results concerning the blue topaz sample from the pegmatites of Padre Paraíso (Minas Gerais state, Brazil) have already been published (Precisvalle et al.; 2021).

5.1 Scan electron microscopy and EDS microanalysis

5.1.1 Padre Paraíso topaz chemistry outcome (from Precisvalle et. al 2021)

The two Padre Paraíso topazes (PadPar1, PadPar3) show compositional homogeneity, with a very low fluorine content (F =9.95-10.00 wt.%), SiO_2 = 33.18-33.58 wt.% and Al_2O_3 = 56.42-56.87 wt.%. The OH/(OH + F) ratio ranges from 0.474 to 0.476. Recalculation on the basis of three cations indicates an almost ideal Si and Al occupancy, which suggests that the hydroxyl site possibly contains small amount of water to balance the scarceness of F in the site (Table 1 and 2, for PadPar 1 and 3, respectively).

Table 1. Chemical data for PadPar1

topaz	PadPar1						
Analysis spots	01 core	02 core	03 core	04 core	05 core	**average**	σ
SiO_2 (wt.)	32.87	34.38	34.40	33.20	33.05	**33.58**	0.61
Al^2O_3	57.11	56.61	56.45	54.56	57.36	**56.42**	0.90
CaO	0.00	0.00	0.00	0.00	0.02	**0.00**	0.01
Na2O	0.10	0.00	0.00	0.00	0.00	**0.02**	0.04
F	10.03	9.01	9.15	12.24	9.58	**10.00**	1.07
O=F, Cl	4.00	3.61	3.65	4.85	3.83	**3.99**	0.41
a.f.u							
Si	0.984	1.020	1.022	1.022	0.985	**1.01**	0.02
Al	2.016	1.980	1.978	1.978	2.015	**1.99**	0.02
Ca	0.000	0.000	0.000	0.000	0.000	**0.00**	0.00
Na	0.000	0.000	0.000	0.000	0.000	**0.00**	0.00
F	1.055	0.949	0.963	1.288	1.009	**1.05**	0.11
OH°	0.945	1.051	1.037	0.712	0.991	**0.95**	0.11
X_{OH}	0.472	0.526	0.518	0.356	0.496	**0.47**	0.06

OH° = by stoichiometric formula; X_{OH} =OH/(F+OH); atomic formula units (a.f.u): normalized to 3 cations and F+OH = 2 a.f.u. from neutron diffraction.

Table 2. Chemical data for PadPar3

topaz	PadPar3						
Analysis spots	01 core	02 core	03 core	04 core	05 core	**average**	σ
SiO_2 (wt.)	33.07	33.05	34.13	32.94	32.69	**33.18**	0.49
Al^2O_3	57.92	54.90	57.85	56.43	57.22	**56.86**	1.12
CaO	0.00	0.01	0.00	0.00	0.00	**0.00**	0.00
Na2O	0.00	0.00	0.00	0.03	0.00	**0.01**	0.01
F	9.01	12.05	8.02	10.62	10.09	**9.96**	1.38
O=F, Cl	3.61	4.78	3.21	4.23	4.02	**3.97**	0.54
a.f.u							
Si	0.979	1.014	1.001	0.994	0.979	**0.99**	0.01
Al	2.021	1.986	1.999	2.006	2.021	**2.01**	0.01
Ca	0.000	0.000	0.000	0.000	0.000	**0.00**	0.00
Na	0.000	0.000	0.000	0.000	0.000	**0.00**	0.00
F	0.949	1.269	0.845	1.118	1.062	**1.05**	0.14
OH°	1.051	0.731	1.155	0.882	0.938	**0.95**	0.14
X_{OH}	0.526	0.366	0.578	0.441	0.469	**0.48**	0.07

OH° = by stoichiometric formula; X_{OH} =OH/(F+OH); atomic formula units (a.f.u): normalized to 3 cations and F+OH = 2 a.f.u. from neutron diffraction.

5.1.2 Baoshan topaz chemistry outcome

The Baoshan samples show compositional homogeneity for crystals 1 and 2 while some differences has been encountered in crystal 3. The fluorine content ranges between 14.48 and 16.32 wt.%, the SiO_2 = 30.98-31.29 wt.% and Al_2O_3 = 53.96-52.07 wt.%. The OH/(OH + F) ratio ranges from 0.24 to 0.141. Differently from the PadPar topaz, here it has also been recorded a small amount of Na between 0.02 and 0.01 wt.%. The data for Bao1, 2 and 3 are given in the table below (Table 3, 4 and 5, respectively).

Table 3. Chemical data for major elements in Bao1

topaz	Bao 1					
Analysis spots	01 core	02 core	03 core	04 core	**average**	σ
SiO_2 (wt.)	31.11	30.69	31.42	30.70	**30.980**	0.31
Al_2O_3	55.01	54.35	53.46	53.00	**53.955**	0.78
CaO						
Na_2O	0.85	0.84	0.43	0.47	**0.648**	0.20
F	13.03	14.12	14.69	15.83	**14.418**	1.01
O=F, Cl						
a.f.u.						
Si	0.964	0.963	0.994	0.984	**0.976**	0.01
Al	2.010	2.011	1.993	2.002	**2.004**	0.01
Ca						
Na	0.026	0.026	0.013	0.015	**0.020**	0.01
F	1.372	1.486	1.546	1.666	**1.518**	0.11
OH°	0.628	0.514	0.454	0.334	**0.482**	0.11
X_{OH}	**0.314**	**0.257**	**0.227**	**0.167**	**0.241**	0.05

OH° = by stoichiometric formula; X_{OH} =OH/(F+OH); atomic formula units (a.f.u): normalized to 3 cations and F+OH = 2 a.f.u. from neutron diffraction.

Table 4. Chemical data for major elements in Bao2

Topaz3	Bao 2				
Analysis spots	01 core	02 core	03 core	**average**	σ
SiO_2 (wt.)	30.90	31.59	31.04	31.18	0.30
Al_2O_3	53.42	54.48	53.22	53.71	0.55
CaO					
Na_2O	0.70	0.87	0.15	0.57	0.31
F	14.98	13.07	15.59	14.55	1.07
O=F, Cl					
a.f.u.					
Si	0.980	0.981	0.992	0.984	0.01
Al	1.998	1.993	2.004	1.998	0.00
Ca					
Na	0.022	0.026	0.005	0.017	0.01
F	1.577	1.376	1.641	1.531	0.11
OH°	0.423	0.624	0.359	0.469	0.11
X_{OH}	**0.212**	**0.312**	**0.179**	**0.234**	0.06

OH° = by stoichiometric formula; X_{OH} =OH/(F+OH); atomic formula units (a.f.u): normalized to 3 cations and F+OH = 2 a.f.u. from neutron diffraction.

Table 5. Chemical data for major elements in Bao3

	Bao 3			
Analysis spots	01 core	02 core	**average**	σ
SiO_2 (wt.)	31.53	31.04	**31.29**	0.25
Al_2O_3	51.34	52.80	**52.07**	0.73
CaO				
Na_2O	0.10	0.55	**0.33**	0.23
F	17.03	15.61	**16.32**	0.71
O=F, Cl				
a.f.u.				
Si	1.027	0.993	**1.010**	0.02
Al	1.970	1.990	**1.980**	0.01
Ca				
Na	0.003	0.017	**0.010**	0.01
F	1.793	1.643	**1.718**	0.07
OH°	0.207	0.357	**0.282**	0.07
X_{OH}	**0.104**	**0.178**	**0.141**	0.04

OH° = by stoichiometric formula; X_{OH} =OH/(F+OH); atomic formula units (a.f.u): normalized to 3 cations and F+OH = 2 a.f.u. from neutron diffraction.

5.2 Structural analyses

5.2.1 X-ray and neutron powder diffraction measurements and structure determination for Padre Paraíso topaz (from Precisvalle et. al 2021)

All data processing was carried out by the full profile Rietveld analysis using the GSAS package (Von Dreele and Larson 2004) with the EXPGUI interface (Toby 2001). The profile was modelled by a pseudo-Voigt function which uses an accurate description of the reflection asymmetry due to axial divergence described by (Finger et al. 1994) as an implementation of the peak shape function described by (Laar and Yelon 1984). The background was empirically fitted using a Chebyschev polynomial with 20 and 14 polynomial coefficients for synchrotron and neutron refinements, respectively. The scale factor, 2θ-zero shift, unit-cell parameters and thermal displacement parameters were accurately refined. Final crystal and refinement data for four selected temperatures (298, 776, 1073 and 1273 K) are reported in Table 6(a, b). The thermal expansion coefficients were investigated for both samples from 298 to 1273 K (Table 7) by the EosFit7-GUI software (Gonzales et al 2016). Positional and thermal parameters, fractions at four selected temperatures (298, 776, 1073 and 1273 K) can be found in Table 8 and 9, for synchrotron and neutron refinements, respectively.

Table 6a: Refinement details of the synchrotron data collection and unit cell parameters of PadPar topaz at 298, 776, 1073 and 1273 K

	298 K	**776 K**	**1073 K**	**1273 K**
Space Group	*Pbnm*	*Pbnm*	*Pbnm*	*Pbnm*
a (Å)	4.65237(2)	4.66991(2)	4.68036(2)	4.68413(1)
b (Å)	8.80479(3)	8.83312(4)	8.85117(4)	8.85763(1)
c (Å)	8.38936(3)	8.42725(1)	8.44936(4)	8.45630(1)
V (Å^3)	343.655(2)	347.623(3)	350.029(3)	350.851(6)
2θ range (°)	10-55	10-55	10-55	10-55
R_{wp} (%)	7.81	7.49	8.4	9.26
R_p (%)	5.89	5.62	6.25	6.95
R_F^2 (%)	5.16	4.75	7.31	9.35
No. of reflections	5631	5631	5631	5631
N_{obs}	184	184	186	186
N_{Var}	98	98	98	98

$$R_p = \Sigma[Y_{io}-Y_{ic}]/\Sigma Y_{io};\ R_{wp} = [\Sigma wi(Y_{io}-Y_{ic})^2/\Sigma wi Y_{io}^2]^{0.5};\ R_{F2} = \Sigma|F_o^2-F_c^2|/|F_o^2|$$

Table 6b: Refinement details of the neutron data collection and unit cell parameters of PadPar topaz at 298, 776, 1073 and 1273 K.

	298 K	**776 K**	**1073 K**	**1273 K**
Space Group	*Pbnm*	*Pbnm*	*Pbnm*	*Pbnm*
a (Å)	4.6445(1)	4.6597(1)	4.6703(3)	4.6845(8)
b (Å)	8.7877(6)	8.8132(5)	8.8298(5)	8.8518(16)
c (Å)	8.3742(6)	8.4066(5)	8.4286(6)	8.4610(17)
V (Å^3)	341.79(4)	345.23(4)	347.58(4)	350.85(11)
2θ range (°)	22-142	22-142	22-142	22-142
R_{wp} (%)	8.95	8.55	7.80	6.45
R_p (%)	6.47	6.08	5.67	5.04
R_F^2 (%)	5.03	7.69	10.26	11.52
No. of reflections	2409	2406	2406	2366
N_{obs}	412	377	377	655
N_{Var}	98	98	98	98

$$R_p = \Sigma[Y_{io}-Y_{ic}]/\Sigma Y_{io};\ R_{wp} = [\Sigma wi(Y_{io}-Y_{ic})^2/\Sigma wi Y_{io}^2]^{0.5};\ R_{F2} = \Sigma|F_o^2-F_c^2|/|F_o^2|$$

Table 7. Thermal expansion coefficient for all crystallographic values calculated from synchrotron and neutron diffraction data, respectively. Thermal expansion coefficients were calculated by EosFit7-GUI software.

	a	*b*	*c*	*V*
298-1300 K	a_0= 4.6524(1)	b_0 = 8.8048(1)	c_0 = 8.3894(1)	V_0 = 343.66(1)
Synchrotron data	α_0= 0.64(2)	α_0= 0.51(2)	α_0= 0.83(3)	α_0= 1.96(6)
	α_1= 0.12(3)	α_1= 0.19(2)	α_1= 0.04(5)	α_1= 0.36(9)
	α_2= 0.00000	α_2= 0.00001	α_2= 0.00000	α_2= 0.00002
298-1300 K	a_0= 4.6441(6)	b_0 = 8.7879(1)	c_0 = 8.3738(13)	V_0 = 341.77(14)
Neutron data	α_0= 0.57(11)	α_0= 0.45(10)	α_0= 0.60(12)	α_0= 1.50(30)
	α_1= 0.26(15)	α_1= 0.29(12)	α_1= 0.42(16)	α_1= 1.20(40)
	α_2= 0.00010	α_2= 0.00002	α_2= 0.00001	α_2= 0.00008

Table 8. Atomic coordinates, fractions, and thermal parameters for synchrotron data diffraction at 298, 776, 1073 and 1273K from in situ time resolved data.

Atom	Site	298K	776K	1073K	1273K
Si	*x*/*a*	0.3978(2)	0.3976(3)	0.3968(3)	0.3963(3)
	y/*b*	0.9412(1)	0.9409(1)	0.9406(1)	0.9406(1)
	z/*c*	0.25	0.25	0.25	0.25
	Frac	1.0	1.0	1.0	1.0
	Uiso*100	0.27(1)	0.57(1)	1.07(1)	2.13(1)
Al	*x*/*a*	0.9042(2)	0.9033(2)	0.9034(2)	0.9034(2)
	y/*b*	0.1311(1)	0.1313(1)	0.1312(1)	0.1316(1)
	z/*c*	0.0823(1)	0.0821(1)	0.0822(1)	0.0823(1)
	Frac	1.0	1.0	1.0	1.0
	Uiso*100	0.29(1)	0.59(1)	1.09(1)	2.18(1)
O1	*x*/*a*	0.7937(4)	0.7962(4)	0.7983(5)	0.7975(5)
	y/*b*	0.5320(2)	0.5323(3)	0.5324(3)	0.5324(3)
	z/*c*	0.25	0.25	0.25	0.25
	Frac	1.0	1.0	1.0	1.0
	Uiso*100	0.47(1)	0.76(1)	2.07(1)	4.04(1)
O2	*x*/*a*	0.4569(5)	0.4581(5)	0.4590(5)	0.4576(5)
	y/*b*	0.7563(3)	0.7573(3)	0.7573(3)	0.7571(3)
	z/*c*	0.25	0.25	0.25	0.25
	Frac	1.0	1.0	1.0	1.0
	Uiso*100	0.46(1)	0.76(1)	2.06(1)	4.15(1)
O3	*x*/*a*	0.7900(3)	0.7915(3)	0.7918(4)	0.7916(4)
	y/*b*	0.0111(2)	0.0120(2)	0.0122(2)	0.0118(2)
	z/*c*	0.9074(2)	0.9065(2)	0.9058(2)	0.9062(2)
	Frac	1.0	1.0	1.0	1.0
	Uiso*100	0.43(1)	0.73(1)	2.03(1)	4.12(1)
F	*x*/*a*	0.9003(3)	0.9007(3)	0.9001(4)	0.9012(4)
	y/*b*	0.7529(2)	0.7526(2)	0.7527(2)	0.7530(2)
	z/*c*	0.0573(2)	0.0569(2)	0.0561(2)	0.0568(2)
	Uiso*100	0.41(1)	0.71(1)	2.01(1)	4.02(1)
O4	*x*/*a*	0.9003(3)	0.9007(3)	0.9001(4)	0.9012(4)
	y/*b*	0.7529(2)	0.7526(2)	0.7527(2)	0.7530(2)
	z/*c*	0.0573(2)	0.0569(2)	0.0561(2)	0.0568(2)
	Uiso	0.41(1)	0.71(1)	2.01(1)	4.02(1)
H	*x*/*a*	0.0318(28)	0.022(13)	0.030(14)	0.024(14)
	y/*b*	0.7154(30)	0.7030(90)	0.7150(110)	0.7110(110)
	z/*c*	0.1352(26)	0.1230(90)	0.1170(110)	0.1270(100)
	Uiso*100	0.69(1)	0.90(1)	4.09(1)	6.09(1)

Table 9. Atomic coordinates, fractions and thermal parameters for neutron data diffraction at 298, 776, 1073 and 1273K from *in situ* time resolved data.

Atom	***Site***	***298K***	***776K***	***1073K***	***1273K***
Si	*x*/*a*	0.3815(21)	0.3899(20)	0.3892(20)	0.3823(28)
	y/*b*	0.9453(10)	0.9432(10)	0.9427(11)	0.9400(15)
	z/*c*	0.25	0.25	0.25	0.25
	Occ	1.0	1.0	1.0	1.0
	Uiso*100	0.21(1)	0.58(1)	1.10(1)	2.37(5)
Al	*x*/*a*	0.8936 (20)	0.8984(18)	0.8967(19)	0.8945(33)
	y/*b*	0.1324(8)	0.1313(8)	0.1318(9)	0.1288(14)
	z/*c*	0.0798(11)	0.0807(11)	0.0810(11)	0.0837(17)
	Occ	1.0	1.0	1.0	1.0
	Uiso*100	0.31(1)	0.52(1)	1.80(1)	2.12(5)
O1	*x*/*a*	0.8131(15)	0.8032(14)	0.8035(14)	0.8061(24)
	y/*b*	0.5320(8)	0.5344(7)	0.5337(8)	0.5273(19)
	z/*c*	0.25	0.25	0.25	0.25
	Occ	1.0	1.0	1.0	1.0
	Uiso	0.47(1)	0.72(1)	2.60(1)	4.16(3)
O2	*x*/*a*	0.4612(15)	0.4572(15)	0.4568(15)	0.4757(34)
	y/*b*	0.7552(11)	0.7579(10)	0.7585(11)	0.7593(18)
	z/*c*	0.25	0.25	0.25	0.25
	Occ	1.0	1.0	1.0	1.0
	Uiso*100	0.46(1)	0.76(1)	2.10(1)	4.02(3)
O3	*x*/*a*	0.7926(11)	0.7907(10)	0.7914(11)	0.8055(18)
	y/*b*	0.0127(5)	0.0110(5)	0.0101(6)	0.0166(13)
	z/*c*	0.9089(6)	0.9091(6)	0.9078(6)	0.9092(13)
	Occ	1.0	1.0	1.0	1.0
	Uiso*100	0.43(1)	0.74(1)	2.08(1)	4.02(3)
F	*x*/*a*	0.9055(11)	0.8963(11)	0.8951(11)	0.8977(26)
	y/*b*	0.7505(7)	0.7547(7)	0.7538(8)	0.7583(12)
	z/*c*	0.0552(5)	0.0545(5)	0.0538(5)	0.0528(13)
	Occ	0.5163(2)	0.5135(2)	0.5190(1)	0.3150(1)
	Uiso	0.41(1)	0.71(1)	2.15(1)	4.25(3)
O4	*x*/*a*	0.9055(11)	0.8963(11)	0.8951(11)	0.8977(26)
	y/*b*	0.7505(7)	0.7547(7)	0.7538(8)	0.7583(12)
	z/*c*	0.0552(5)	0.0545(5)	0.0538(5)	0.0528(13)
	Occ	0.4840(2)	0.4833(2)	0.4840(1)	0.4816(2)
	Uiso*100	0.411(1)	0.71(1)	2.15(1)	4.25(3)
H	*x*/*a*	0.3026(15)	-0.035(9)	0.001(20)	0.0338(8)
	y/*b*	0.7325(11)	0.774(6)	0.748(16)	0.7177(9)
	z/*c*	0.1476(11)	0.1609(20)	0.153(7)	0.1290(7)
	Occ	0.4840(2)	0.4833(2)	0.4840(1)	0.4816(2)
	Uiso*100	0.59(3)	0.96(3)	3.446(3)	5.53(7)

5.2.1.1 Crystal structure at room temperature

Synchrotron X-ray powder diffraction of PadPar topaz yields higher quality powder diffraction patterns than when compared to diffraction, hence this data set was chosen for the initial structural investigation. The indexing process performed by EXPO2014 via the N-TREOR09 program (Altomare 2009) unambiguously suggested the *Pbnm* space group. Consequently, PadPar structural refinements of data collected at room temperature were carried out in the space group *Pbnm* starting from the atomic coordinates reported by (Gatta et al. 2006) without the proton position and using only the (neutral) atomic scattering factors of Al, Si, and O. When the convergence was achieved, no peaks larger than ±0.32 $e^-/Å^3$ were present in the final difference Fourier map. Lattice parameters refined from synchrotron X-ray are *a*=4.652373(18) Å, *b*=8.804789(34) Å, *c*= 8.389362(32) Å, *V*=343.6548(23) $Å^3$.

The structural refinement with the neutron diffraction data collected at room temperature was performed in the space group *Pbnm*, starting with the atomic coordinates obtained from the X-ray structural refinement.

The F-amount of our sample refined on the basis of the neutron diffraction data is 1.032 a.f.u; this corresponds to 10.94 wt.%, in agreement with the EDS microanalysis. When convergence was achieved, the final difference Fourier map revealed the occurrence of a peak at *x=0.020, y=0.707, z=0.141* which was then refined with the H scattering length. The O-H bond distance was initially fixed and the constrain was completely removed in the last cycles of refinement (O4-H 0.979 difference <2σ) whereas the proton occupancy factor was fixed as a function of the oxygen at the F/O4 site (for the F/O4 site, %O = 100 -%F).

The unit cell parameters obtained from the neutron data are a = 4.64453(3) Å, b = 8.7877(6) Å, c = 8.3742(6) Å and V= 341.79 Å3, in very good agreement with those obtained from synchrotron diffraction data. The H and F occupancies refined from neutron diffraction were then fixed in the synchrotron structure refinement. The bond distances and angles between the proton site and the surrounding anions revealed the occurrence of potential H···O/F interactions (Fig. 20 a, b). Two of

them (H···O1 and H···O2) are slightly stronger than the others (Table 10). This OH topological configuration reveals shorter H···O/F bond distances and longer H-H bond distances longer [H-H 1.715(6) Å] than those previously described [1.463(5) Å (Gatta et al. 2006)] (Fig.1 a, b; Table 5).

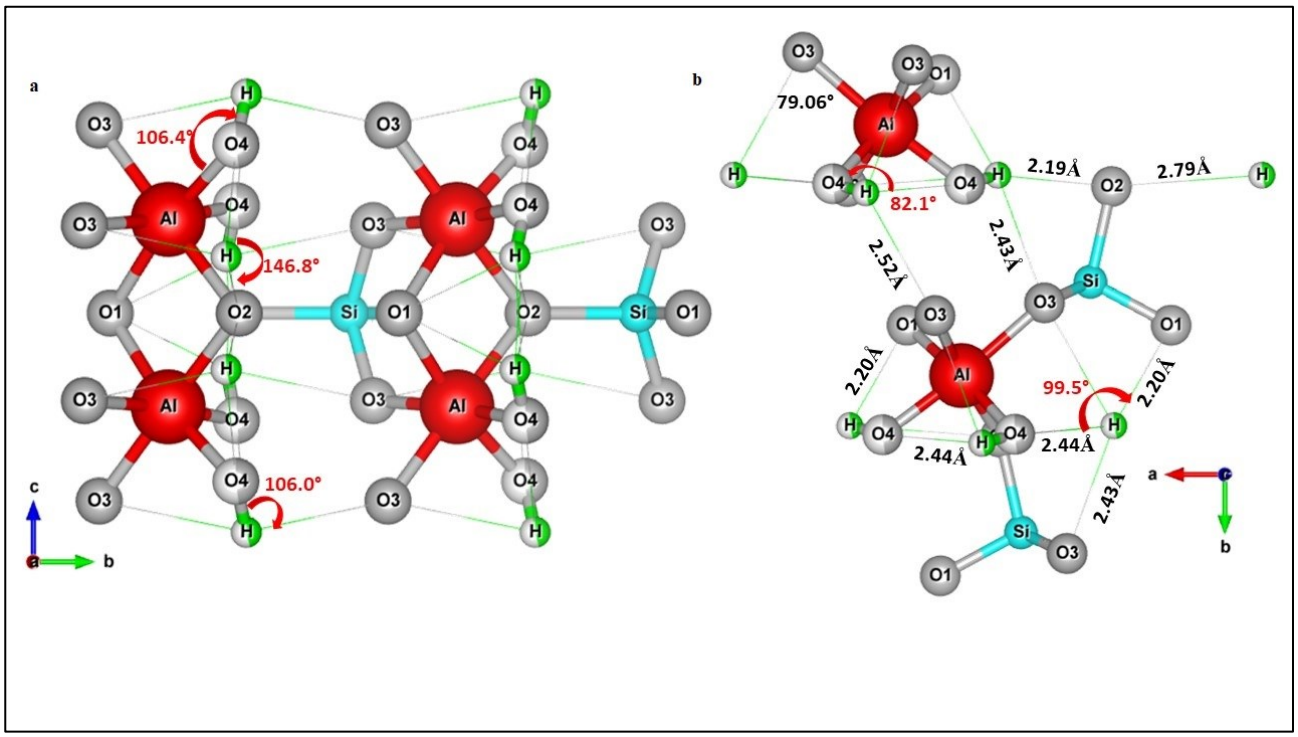

Figure 20a, b. Hydrogen-bond system of topaz PadPar. Schematic representation of hydrogen bonding (green thin dotted lines) at room temperature. The main interactions between H atoms and the surrounding polyhedral environment are viewed along the *a* (**a**) and *c* axes (**b**). The bond distance and angle between the proton site and the surrounding anions revealed the occurrence of potential H···O/F interactions, where two of them (H···O1 and H···O2) are slightly stronger than the others. The H sphere appears partially green coloured due to the OH/F substitution, according to the refined occupancies from neutron diffraction data. The structure image has been obtained using VESTA Version 3

Table 10. The refined neutron bond distances between the proton site and the surrounding anions in PadPar topaz. The corresponding values refined by Gatta et al (2006) are reported for

	This work	Gatta et al.
F/O4···F/O4 (Å)	3.262(7)	3.195(3)
H···O1 (Å)	2.204(9)	2.307(6)
H···O2 (Å)	2.186(7)	2.216(5)
H···O3 (Å)	2.432(7)	2.380(5)
H···F/O4 (Å)	0.979(7)	0.989(5)
H···H (Å)	1.715(7)	1.463(5)

5.2.1.2 Temperature-dependent variation of the unit cell parameters and structural modifications

The XRPD temperature ramp (Fig. 21a, b) analysis revealed that PadPar topaz maintains its crystallinity and symmetry up to the highest investigated temperature (T = 1273 K). Instead in neutron data (Fig. 21c, d), a progressive broadening peak was observed from ~1170 K, thus highlighting a progressive loss of crystallinity. This result can be explained by the different heating rate used during the data collection, as discussed below. The evolution of the cell parameters of the PadPar samples during the *in situ* heating process in the 298-1273 K range from both synchrotron and neutron data are reported in Figure 22 a and b, respectively. To better understand these differences and to allow a better comparison between the two systems and among their whole cell parameters, we reported normalized dimensionless values defined as $V(T)/V_0$, $a(T)/a_0$, $b(T)/b_0$, and $c(T)/c_0$, being the reference values obtained in the refinement of the first recorded pattern (T) 298 K. In both samples *a*, *b* and *c* increase as the temperature increases up to 1010 K, indicating that the thermal expansion is the physical mechanism dominating this stage of the experiment. Unit-cell axes refined from synchrotron data do not show any other modifications until the maximum temperature is reached. A strong change in the unit cell parameters evolution is detected from neutron data. In particular, up to this temperature *a* and *b* cell-axes have a similar expansion rate while the *c*-axis undergoes a significant increase up to about 1273 K. These variations are reflected in the evolution of the unit-cell volume, V_S (δV = 2%) and V_N (δV = 2.65%). The thermal expansion coefficients were investigated for both samples from 298 to 1273 K using the EosFit7-GUI software (Gonzales Plata et al. 2016). The temperature evolution was properly described using a polynomial expression:

$$\alpha = \alpha_0 + \alpha_1 T + \alpha_2 T^{-1} \quad (1)$$

where the mean thermal expansion coefficient α is expressed in K^{-1}, and constants α_0, α_1, and α_2, derived from the experimental data are expressed in K^{-1}, K^{-2}, and K, respectively (Fei 1995).

The PadPar coefficients along the crystal axes are $\alpha_a = 6.40(20)\times10^{-6}\ K^{-1}$, $\alpha_b = 5.09(17)\times10^{-6}\ K^{-1}$, $\alpha_c = 8.30(30)\times10^{-6}\ K^{-1}$, $\alpha_V = 1.96(6)\times10^{-5}\ K^{-1}$, then the ratio of thermal expansion coefficients $\alpha_a:\alpha_b:\alpha_c$ is

0.77:0.61:1. These values are in very good agreement with those reported by Tennakoon et. al. (2018) (Tennakoon et al. 2018). For neutron data the coefficients are $\alpha_a = 5.70(11)\times10^{-6}\ K^{-1}$, $\alpha_b = 4.50(10)\times10^{-6}\ K^{-1}$, $\alpha_c = 6.00(12)\times10^{-6}\ K^{-1}$, $\alpha_V = 1.50(3)\times10^{-5}\ K^{-1}$, then the ratio of thermal expansion coefficients $\alpha_a:\alpha_b:\alpha_c$ is *0.95:0.75:1*. These coefficients have been compared in Figure 23a, b. PadPar coefficients are in-line-with those reported by (Komatsu et al. 2003) showing a significant anisotropy due to the presence of a strong cleavage along {001} (Day et al. 1995). These changes are reflected on $[SiO_4]^{4-}$ tetrahedra and $Al[O_4(F,OH)_2]$ octahedra. In fact, Si–O and Al-O distances and angles refined from synchrotron data increase linearly until the maximum temperature is reached, resulting in a positive expansion of the polyhedra (Figure 24).

A very different situation was encountered for *in situ* neutron data where the octahedral expansion is regularly counterbalanced by a tetrahedral contraction, up to 1170 K. Above this temperature, this trend suddenly changes as a result of the structural modifications induced by the fluorine loss, in close agreement with the evolution of refined occupancy fractions reported in Figure 25.

In neutron analyses, the main diffraction peaks associated with the topaz phase declined rapidly with continued heating, indicating a rapid decomposition of the sample. A second phase appeared to grow at the same rate as the peak from the previous phase declined thus revealing the formation of mullite $Al_{4+2x}Si_{2-2x}O_{10-x}$ ((120) and (210) reflections, at 25.90 and 26.09 2θ°, respectively). Mullite occurrence is well known in literature (Day et al. 1995) (Peng et al 2004), but always at higher temperature. When the highest temperature was reached, the Rietveld refinement indicated ~ 30 and 70% in weight of topaz and mullite, respectively. At the same time, the fluorine content decreased from 0.77 to 0.63 a.f.u.

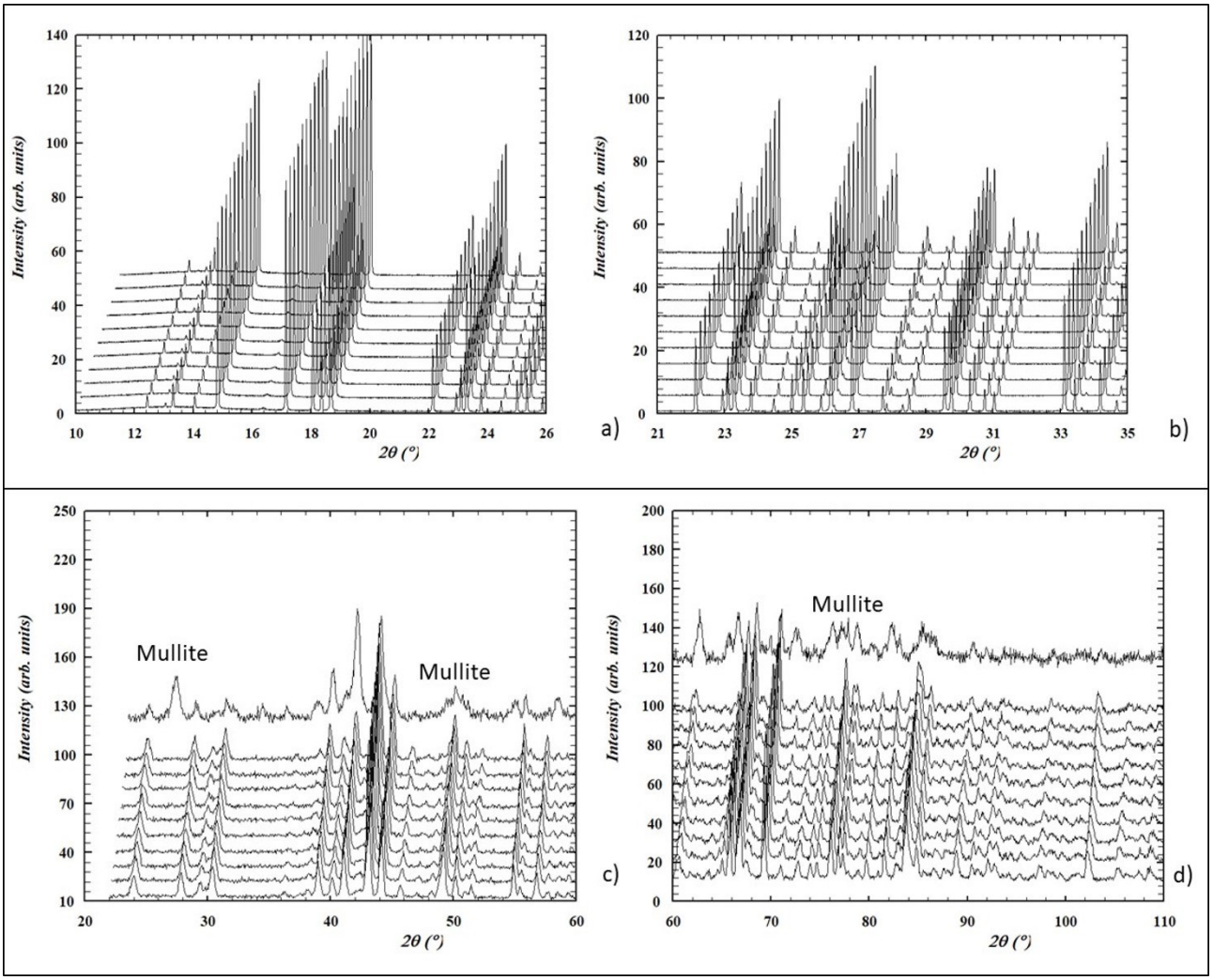

Figure 21a, b, c, d. Cascade plots of PadPar topaz from Synchrotron (**a**, **b**) and Neutron (**c**, **d**) diffraction data. The samples were heated from room temperature to 1273 K (heating rate 5 K and 2 K/min for Synchrotron and Neutron data collection, respectively). Powder diffraction patterns recorded every 100 K are also shown. In neutron analyses, the rapid decomposition of the sample upon heating revealed the formation of mullite $Al_{4+2x}Si_{2-2x}O_{10-x}$. This image has been obtained with WinPLOTR from FullProf Suite

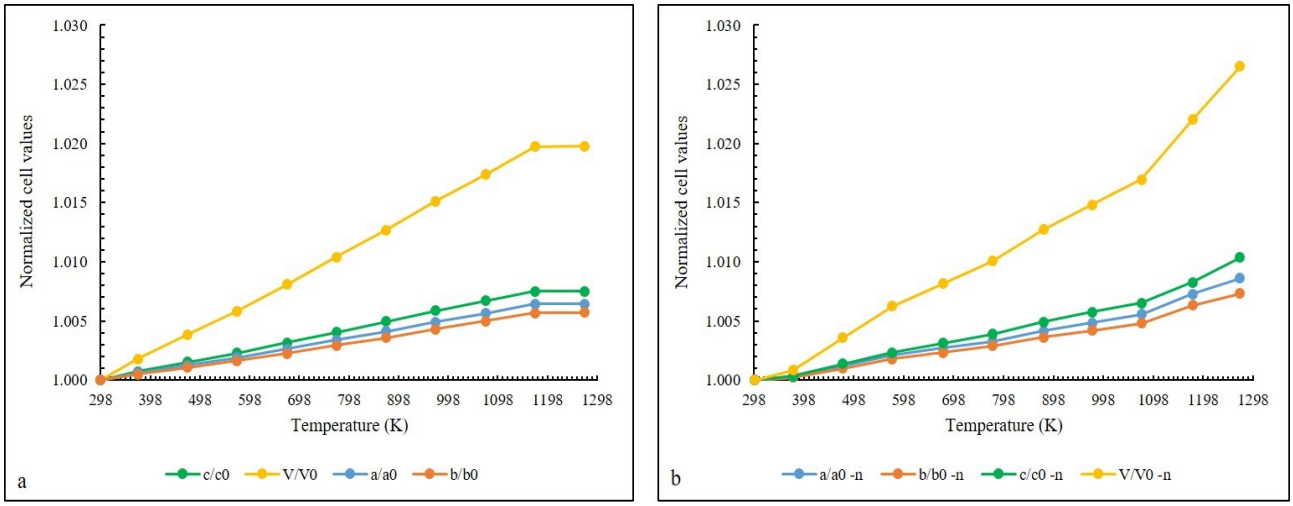

Figure 22a, b. Evolution of unit cell parameters for PadPar topaz normalized with respect to room temperature values (a/a_0, b/b_0, c/c_0, V/V_0) from in situ synchrotron (**a**) and neutron diffraction (**b**) data. A strong change in the unit cell parameters evolution is detected from neutron data (**b**), in particular, up to 1075 K *a* and *b* cell-axes have a similar expansion rate while the *c*-axis undergoes an increase up to about 1273 K. Standard deviation errors are within

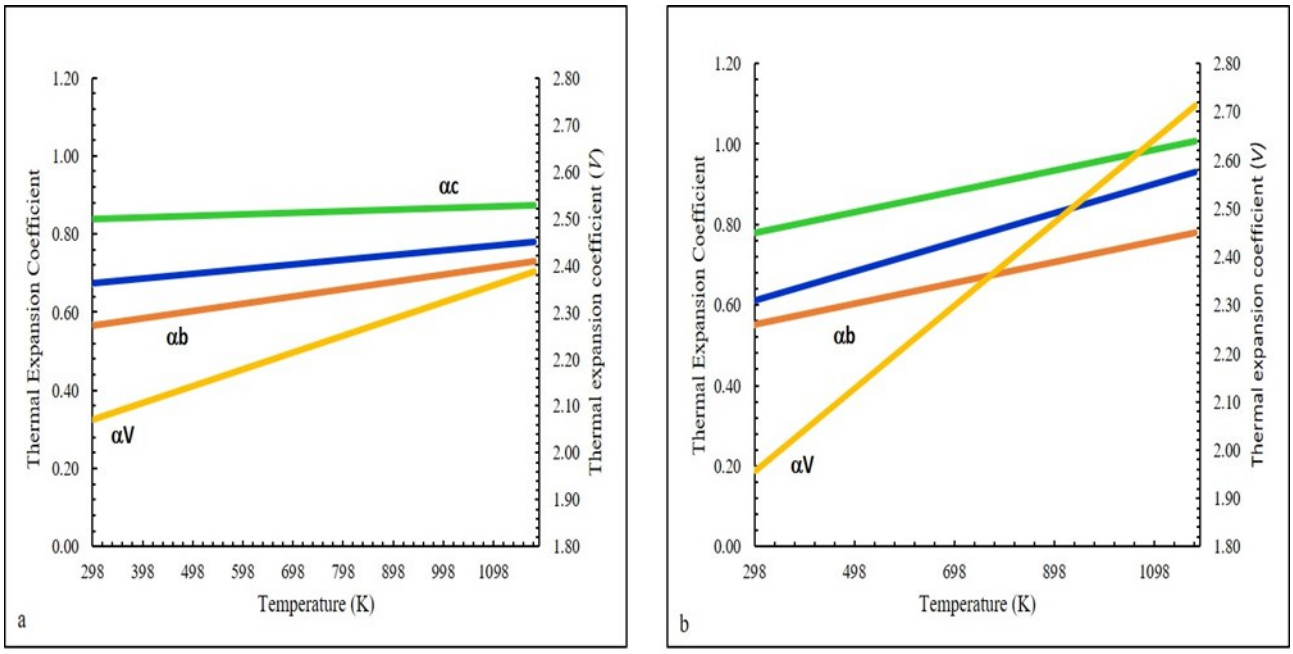

Figure 23a, b. Thermal expansion model for in situ heating of the PadPar topaz, obtained from synchrotron (**a**) and neutron diffraction (**b**) analyses in the temperature range of 298 to 1273 K. Orange, yellow, green and blue symbols refer to Temperature *vs* Volume data selected for the EoS fitting (see text for details). Standard deviation errors are within the symbol size.

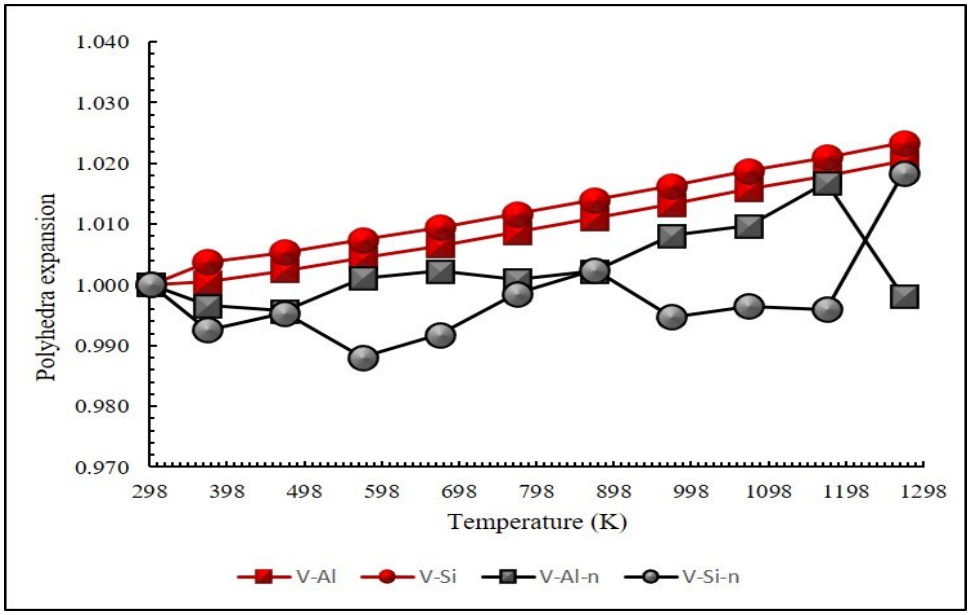

Figure 24. Polyhedral evolution of PadPar topaz expressed as $V/V_{0,}$ with V–Al and V–Si indicating octahedral and tetrahedral volume respectively, as obtained from synchrotron (red symbols) and neutron (grey symbols) data. For in situ neutron data the octahedral expansion is regularly counterbalanced by a tetrahedral contraction, up to 1170 K. Above this temperature, the fluorine loss induced a structural modification that suddenly change this trend. Standard deviation errors are within the symbol size.

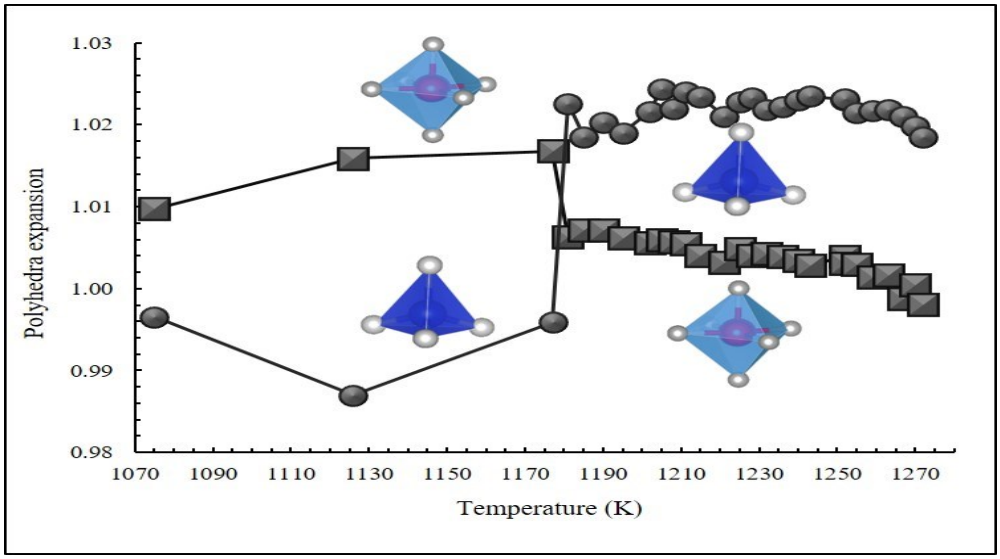

Figure 25. Polyhedral evolution of PadPar topaz in the critical zone (1071–1273 K) expressed as V/V0 as obtained from neutron data. The octahedral expansion (square symbols) is continuously balanced by a tetrahedral contraction (circle symbol) up to 1170 K, where a strong F loss, accompanied by a crystallinity loss and a phase change are envisaged. At higher temperature the concomitant expansion and contraction of tetrahedra and octahedra, respectively, is minimized. For sake of clarity octahedra (light blue) and tetrahedra (dark blue)

5.2.2 X-ray and neutron powder diffraction measurements and structure determination for Baoshan topaz

Data processing was carried out by the full profile Rietveld analysis using the GSAS package (Von Dreele and Larson, 2004) with the EXPGUI interface (Toby 2001). The profile was modelled by a pseudo-Voigt function which uses an accurate description of the reflection asymmetry due to axial divergence described by (Finger et al. 1994) as an implementation of the peak shape function described by (Laar and Yelon 1984). The background was empirically fitted using a Chebyschev polynomial with 20 and 14 polynomial coefficients for synchrotron and neutron refinements, respectively. The scale factor, 2θ-zero shift, unit-cell parameters and thermal displacement parameters were accurately refined. Final crystal and refinement data for four selected temperatures (298, 776, 1073 and 1273 K) are reported in Table 10(a, b). The thermal expansion coefficients were investigated for both samples from 298 to 1273 K (Table 11) by the EosFit7-GUI software (Gonzales et al 2016). Positional and thermal parameters, fractions at four selected temperatures (298, 776, 1073 and 1273 K) and (330, 776, 1073 and 1273 K) can be found in Table 12 and 13, for synchrotron and neutron refinements, respectively.

Table 10a: Refinement details of the synchrotron data collection and unit cell parameters of Bao topaz at 298, 776, 1073 and 1273 K

	298 K	**776 K**	**1073 K**	**1273 K**
Space Group	*Pbnm*	*Pbnm*	*Pbnm*	*Pbnm*
a (Å)	4.6493(1)	4.6632(1)	4.6735(1)	4.6806(1)
b (Å)	8.7964(1)	8.8200(1)	8.8380(1)	8.8507(1)
c (Å)	8.3901(1)	8.4207(1)	8.4431(1)	8.4572(1)
V (Å^3)	343.13(1)	346.34(1)	348.74(1)	350.35(1)
2θ range (°)	10 - 65	10 - 65	10 - 65	10 - 65
R_{wp} (%)	7.41	7.27	7.25	7.66
R_p (%)	5.62	5.55	5.55	5.8
R_F^2 (%)	4.43	4.29	4.91	5.88
No. of reflections	6885	6885	6885	6885
N_{obs}	301	303	301	303
N_{Var}	56	56	56	56

$R_p = \Sigma[Y_{io}-Y_{ic}]/\Sigma Y_{io}$; $R_{wp} = [\Sigma wi(Y_{io}-Y_{ic})^2/\Sigma wi Y_{io}^2]^{0.5}$; $R_{F2} = \Sigma|F_o^2-F_c^2|/|F_o^2|$

Table 10b: Refinement details of the neutron data collection and unit cell parameters of Bao topaz at 330, 776, 1073 and 1273 K.

	330 K	**776 K**	**1073 K**	**1273 K**
Space Group	*Pbnm*	*Pbnm*	*Pbnm*	*Pbnm*
a (Å)	4.6406(1)	4.6559(1)	4.6666(1)	4.6760(1)
b (Å)	8.7767(1)	8.8025(1)	8.8205(1)	8.8334(1)
c (Å)	8.3743(1)	8.4083(1)	8.4311(1)	8.4481(1)
V (Å^3)	341.08(1)	344.58(1)	346.98(1)	348.95(1)
2θ range (°)	22.8-120	22.8-120	22.8-120	22.8-120
R_{wp} (%)	11.23	11.02	10.92	10.23
R_p (%)	7.69	7.58	7.67	7.52
R_F^2 (%)	3.47	4.03	4.59	5.74
No. of reflections	1945	1945	1945	1945
N_{obs}	410	417	419	657
N_{Var}	56	56	56	56

$$R_p = \Sigma[Y_{io}-Y_{ic}]/\Sigma Y_{io};\ R_{wp} = [\Sigma wi(Y_{io}-Y_{ic})^2/\Sigma wi Y_{io}^2]^{0.5};\ R_{F2} = \Sigma|F_o^2-F_c^2|/|F_o^2|$$

Table 11. Bao topaz thermal expansion coefficient for all crystallographic values calculated from synchrotron and neutron diffraction data, respectively. Thermal expansion coefficients were calculated by EosFit7-GUI software.

			a	*b*	*c*	*V*
298-1300 K	a_0=	b_0 =	c_0 = 8.	V_0 = 343.13(1)		
Synchrotron	4.6494(1)	8.7966(1)	3901(1)	α_0= 2.1(1)		
data	α_0= 0.69(1)	α_0= 0.53(1)	α_0= 0.83(1)	α_1= 0.27(1)		
	α_1= 0.07(1)	α_1= 0.18(1)	α_1= 0.07(1)	α_2= 0.00000		
	α_2= 0.00000	α_2= 0.00000	α_2= 0.00000			
298-1300 K	a_0=	b_0 =	c_0 =	V_0 = 341.36(1)		
Neutron data	4.6415(1)	8.7786(1)	8.3783(1)	α_0= 2.1(3)		
	α_0= 0.73(2)	α_0= 0.57(1)	α_0= 0.84(1)	α_1=0.3(4)		
	α_1= 0.06(1)	α_1= 0.12(2)	α_1= 0.07(2)	α_2= 0.00000		
	α_2= 0.00001	α_2= 0.00005	α_2= 0.00005			

Table 12. Bao topaz atomic coordinates, fractions, and thermal parameters for synchrotron data diffraction at 298, 776, 1073 and 1273K in situ time resolved data.

Atom	Site	298K	776K	1073K	1273K
Si	*x*/*a*	0.3973(2)	0.3965(2)	0.3962(2)	0.3956(3)
	y/*b*	0.9408(1)	0.9409(1)	0.9408(1)	0.9409(1)
	z/*c*	0.25	0.25	0.25	0.25
	Frac	1.00	1.00	1.00	1.00
	Uiso*100	0.47(1)	0.88(1)	0.88(1)	1.13(1)
Al	*x*/*a*	0.9038(2)	0.9033(2)	0.9030(2)	0.9032(2)
	y/*b*	0.1310(1)	0.1310(1)	0.1312(1)	0.1313(1)
	z/*c*	0.0827(1)	0.0825(1)	0.08274(1)	0.0827(1)
	Frac	1.00	1.00	1.00	1.00
	Uiso*100	0.65(1)	1.19(1)	1.28(1)	1.58(1)
O1	*x*/*a*	0.7952(4)	0.7974(4)	0.7991(4)	0.7990(4)
	y/*b*	0.5319(2)	0.5322(2)	0.5323(2)	0.5322(2)
	z/*c*	0.25	0.25	0.25	0.25
	Frac	1.00	1.00	1.00	1.00
	Uiso*100	0.33(6)	.79(6)	0.88(6)	1.10(7)
O2	*x*/*a*	0.4573(5)	0.4583(4)	0.4586(4)	0.4581(5)
	y/*b*	0.7570(2)	0.7568(23)	0.7571(2)	0.7574(3)
	z/*c*	0.25	0.25	0.25	0.25
	Frac	1.00	1.00	1.00	1.00
	Uiso*100	0.34(6)	0.83(6)	0.94(6)	1.22(7)
O3	*x*/*a*	0.7903(3)	0.7906(3)	0.7910(3)	0.7916(3)
	y/*b*	0.0106(2)	0.0112(2)	0.0113(2)	0.0113(2)
	z/*c*	0.9074(2)	0.9065(2)	0.9061(2)	0.9063(2)
	Frac	1.00	1.00	1.00	1.00
	Uiso*100	0.32(4)	0.83(6)	0.92(1)	1.14(5)
F	*x*/*a*	0.9020(3)	0.9010(3)	0.9007(3)	0.9004(3)
	y/*b*	0.7526(1)	0.7527(2)	0.7528(1)	0.7528(2)
	z/*c*	0.0568(2)	0.0561(1)	0.0558(1)	0.0560(2)
	Uiso*100	0.67(4)	1.57(4)	1.85(1)	2.25(5)
O4	*x*/*a*	0.9020(3)	0.9010(3)	0.9007(3)	0.9004(3)
	y/*b*	0.7526(1)	0.7527(1)	0.7528(1)	0.7528(2)
	z/*c*	0.0568(1)	0.0561(1)	0.0558(1)	0.0560(2)
	Uiso	0.67(4)	1.57(4)	1.85(1)	2.25(5)
H	*x*/*a*	0.045(12)	0.034(12)	0.029(15)	0.027(16)
	y/*b*	0.698(9)	0.697(11)	0.662(6)	0.664(7)
	z/*c*	0.120(16)	0.115(12)	0.029(14)	0.033(15)
	Uiso*100	0.69(1)	2.90(1)	4.09(1)	6.09(1)

Table 13. Bao topaz atomic coordinates, fractions and thermal parameters for neutron data diffraction at 330, 776, 1073 and 1273K from *in situ* time resolved data.

Atom	Site	330K	776K	1073K	1273K
Si	x/a	0.3952(12)	0.3923(14)	0.3917(14)	0.3903(14)
	y/b	0.9414(7)	0.9396(8)	0.9383(8)	0.9424(7)
	z/c	0.25	0.25	0.25	0.25
	Frac	0.10(1)	0.29(1)	1.66(1)	2.37(1)
	Uiso*100	1.00	1.00	1.00	1.00
Al	x/a	0.9026(10)	0.9026(13)	0.9029(13)	0.9001(12)
	y/b	0.1299(5)	0.1308(6)	0.1299(6)	0.1297(6)
	z/c	0.0823(7)	0.0832(9)	0.0852(9)	0.0839(8)
	Frac	1.00	1.00	1.00	1.00
	Uiso*100	0.16(1)	0.26(1)	1.37(1)	2.36(1)
O1	x/a	0.7956(9)	0.7970(10)	0.7964(10)	0.7971(11)
	y/b	0.5324(5)	0.5332(6)	0.5333(6)	0.5333(7)
	z/c	0.25	0.25	0.25	0.25
	Frac	1.00	1.00	1.00	1.00
	Uiso*100	0.12(1)	0.44(1)	1.30(1)	4.30(1)
O2	x/a	0.4576(10)	0.4580(11)	0.4591(11)	0.4634(12)
	y/b	0.7560(6)	0.7582(7)	0.7585(7)	0.7612(6)
	z/c	0.25	0.25	0.25	0.25
	Frac	1.00	1.00	1.00	1.00
	Uiso*100	0.16(1)	0.35(1)	1.21(1)	4.63(1)
O3	x/a	0.7900(6)	0.7916(7)	0.7925(7)	0.7948(9)
	y/b	0.0102(3)	0.0103(4)	0.0107(4)	0.0113(5)
	z/c	0.9080(4)	0.9080(4)	0.9079(4)	0.9075(5)
	Frac	1.00	1.00	1.00	1.00
	Uiso*100	0.11(1)	0.17(1)	1.35(1)	4.34(1)
F	x/a	0.9034(7)	0.9012(8)	0.9007(8)	0.9032(9)
	y/b	0.7530(4)	0.7541(5)	0.7551(5)	0.7544(6)
	z/c	0.0572(3)	0.0557(4)	0.0551(4)	0.0555(5)
	Frac	0.7995(1)	0.7995(1)	0.7995(1)	0.6215
	Uiso*100	0.60(1)	1.06(1)	2.18(1)	4.22(1)
O4	x/a	0.9034(7)	0.9012(8)	0.9007(8)	0.9032(9)
	y/b	0.7530(4)	0.7541(5)	0.7551(5)	0.7544(6)
	z/c	0.0572(3)	0.0557(4)	0.0551(4)	0.0555(5)
	Frac	0.1969(1)	0.1969(1)	0.1969(1)	0.3016
	Uiso	0.60(1)	1.06(1)	2.18(1)	4.22(1)
H	x/a	0.026(5)	0.053(8)	0.058(7)	0.051(4)
	y/b	0.726(4)	0.687(4)	0.653(4)	0.6941(25)
	z/c	0.1486(27)	0.119(5)	0.071(6)	0.1180(27)
	Frac	0.1969(1)	0.1969(1)	0.1969(1)	0.3016
	Uiso*100	0.58(1)	0.96 (1)	3.53(1)	5.65(1)

5.2.2.1 Crystal structure models at room temperature

Also in this case, the synchrotron X-ray powder diffraction of Bao topaz yields higher quality powder diffraction patterns than when compared to diffraction, hence this data set was chosen for the initial structural investigation. The indexing process performed by EXPO2014 via the N-TREOR09 program (Altomare 2009) unambiguously confirmed the *Pbnm* space group. So, the Bao structural refinements of data collected at room temperature were carried out in this space group starting from the atomic coordinates reported by (Precisvalle et al. 2021) without the proton position and using only the (neutral) atomic scattering factors of Al, Si, and O. When the convergence was achieved, no peaks larger than ±0.32 e^- /Å^3 were present in the final difference Fourier map. Lattice parameters refined from synchrotron X-ray are *a*= 4.649277(15) Å, *b*= 8.796429(27)Å, *c*= 8.390047(24)Å, *V*= 343.1281(18)Å^3.

The structural refinement with the neutron diffraction data collected at room temperature was performed in the space group *Pbnm*, starting with the atomic coordinates obtained from the X-ray structural refinement.

The F-amount of our sample refined on the basis of the neutron diffraction data is 1.599 a.f.u; this corresponds to 16.91 wt.%, in agreement with the EDS microanalysis. When convergence was achieved, the final difference Fourier map revealed the occurrence of a peak at *x=0.045, y=0.698, z=0.120* which was then refined with the H scattering length. The O-H bond distance was initially fixed and the constrain was completely removed in the last cycles of refinement (O4-H 0.982 difference <2σ) whereas the proton occupancy factor was fixed as a function of the oxygen at the F/O4 site (for the F/O4 site, %O = 100 -%F).

The unit cell parameters obtained from the neutron data are a = 4.64058(22)Å, b = 8.7767(4)Å, c = 8.3743(4)Å and V= 341.075(28)Å^3, in very good agreement with those obtained from synchrotron diffraction data. The H and F occupancies refined from neutron diffraction were then fixed in the synchrotron structure refinement. The bond distances and angles between the proton site and the surrounding anions revealed the occurrence of potential H···O/F interactions (Fig. 26 a, b). One of

them (H···O1 and H···O2) are slightly stronger than the others (Table 14). This OH topological configuration reveals shorter H···O/F bond distances and longer H-H bond distances longer (H-H 1.700(5) Å) than those previously described by Gatta et al. (2006) (1.463(5)Å), but smaller then Precisvalle et al. (2021) (1.715 (7)Å) (Fig.20a, b; Table 10).

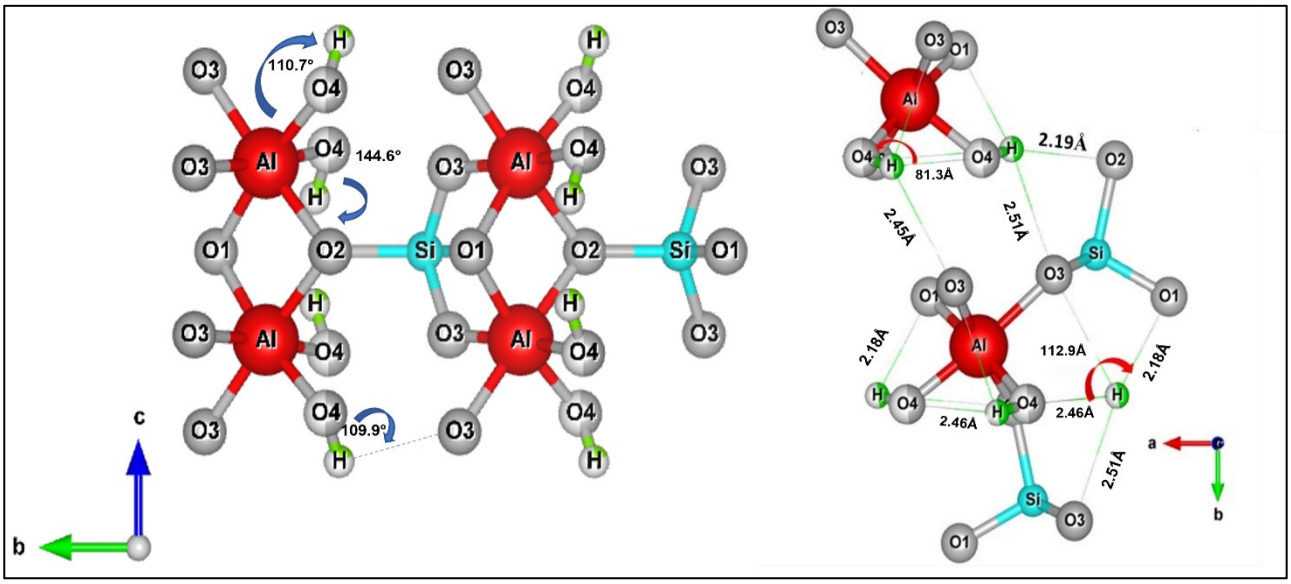

Figure 26a, b. Hydrogen-bond system of Bao topaz. Schematic representation of hydrogen bonding (thing green dotted lines) at room temperature. The main interactions between H atoms and the surrounding polyhedral environment are viewed along the *a* (**a**) and *c* axes (**b**). The bond distance and angle between the proton site and the surrounding anions revealed the occurrence of potential H···O/F interactions, where two of them (H···O1 and H···O2) are slightly stronger than the others. The H sphere appears partially green coloured due to the OH/F substitution, according to the refined occupancies from neutron diffraction data. The structure image has been obtained using VESTA Version 3

Table 14. The refined neutron bond distances for Bao topaz between the proton site and the surrounding anions. The corresponding values refined by Gatta et al (2006) are reported for

	Bao topaz	Gatta et al.
F/O4···F/O4 (Å)	3.228(5)	3.195(3)
H···O1 (Å)	2.180(22)	2.307(6)
H···O2 (Å)	2.191(17)	2.216(5)
H···O3 (Å)	2.46(4)	2.380(5)
H···F/O4 (Å)	0.982(15)	0.989(5)
H···H (Å)	1.700(5)	1.463(5)

5.2.2.2 Temperature-dependent variation of the unit cell parameters and structural modifications

The XRPD temperature ramp (Fig. 27a) analysis revealed that Bao topaz maintains its crystallinity and symmetry up to the highest investigated temperature (T = 1273 K). Instead in neutron data (Fig. 27b), a progressive broadening peak was observed from ~1225 K, thus highlighting a progressive loss of crystallinity. This result can be explained by the different heating rate used during the data collection, as discussed in Precisvalle et al. (2021). The evolution of the cell parameters of the Bao samples during the *in situ* heating process in the 298-1273 K range from both synchrotron and neutron data are reported in Figure 28 a and b, respectively. To better understand these differences and to allow a better comparison between the two systems and among their whole cell parameters, we reported normalized dimensionless values defined as $V(T)/V_0$, $a(T)/a_0$, $b(T)/b_0$, and $c(T)/c_0$, being the reference values obtained in the refinement of the first recorded pattern (T) 298 K for synchrotron and 330 K for neutron diffraction. In both samples *a*, *b* and *c* increase as the temperature increases up to 1273 K, indicating that the thermal expansion is the physical mechanism dominating the experiment. Unit-cell axes refined from synchrotron data do not show any other modifications until the maximum temperature is reached. A change in the unit cell parameters evolution is detected from neutron data. In particular, up to this temperature *a* and *c* cell-axes have a similar expansion rate while the *b*-axis undergoes a small decrease around 1176 K. These variations are reflected in the evolution

of the unit-cell volume, V_S (δV = 2.1%) and V_N (δV = 2.3%). The thermal expansion coefficients were investigated for both samples from 298 to 1273 K using the EosFit7-GUI software (Gonzales Plata et al. 2016).

The Bao coefficients along the crystal axes are α_a= 6.91(2)×10^{-6} K^{-1}, α_b= 5.29(2)×10^{-6} K^{-1}, α_c= 8.26(3)×10^{-6} K^{-1}, α_V= 2.10(1)×10^{-5} K^{-1}, then the ratio of thermal expansion coefficients α_a:α_b:α_c is *0.83:0.64:1*. These values are a bit higher than those reported by Tennakoon et al. (2018) and Precisvalle et al. (2021). For neutron data the coefficients are α_a= 7.3(2)×10^{-6} K^{-1}, α_b= 4.7(2)×10^{-6} K^{-1}, α_c= 8.4(3)×10^{-6} K^{-1}, α_V= 2.06(3)×10^{-5} K^{-1}, then the ratio of thermal expansion coefficients α_a:α_b:α_c is *0.87:0.68:1*. These coefficients have been compared in Figure 29a, b. Bao coefficients are higher than those reported by (Komatsu et al. 2003), but they still show a significant anisotropy linked to the strong cleavage along {001} (Day et al. 1995). These changes are reflected on $[SiO_4]^{4-}$ tetrahedra and $Al[O_4(F, OH)_2]$ octahedra. Al-O distances and angles refined from synchrotron data increase linearly until the maximum temperature is reached, resulting in a positive expansion of the polyhedra (Fig. 30) while the Si-O tetrahedra shows a slightly contractional trend with a positive expansion only in the last stage of heating.

A different situation is shown by *in situ* neutron data where the octahedral expansion is regularly counterbalanced by a tetrahedral contraction, up to 1273 K. In general, Al-O and Si-O show a regular expansion trend in the same order and the structural modifications induced by the fluorine loss around 1225 K does not affect too much the general tendency, in agreement with the evolution of refined occupancy fractions reported in Figure 31. In neutron analyses, the main diffraction peaks associated with the topaz phase have a progressive still not strong decline with continued heating, indicating a slight decomposition of the sample. A second phase appeared to grow at the same rate as the peak from the previous phase declined thus revealing the formation of mullite $Al_{4+2x}Si_{2-2x}O_{10-x}$ [(120) and (210) reflections, at 26.07 and 26.36 2θ°, respectively]. When the highest temperature was reached, the Rietveld refinement indicated ~ 83 and 17% in weight of topaz and mullite, respectively. At the same time, the fluorine content decreased from 1.33 to 1.24 a.f.u

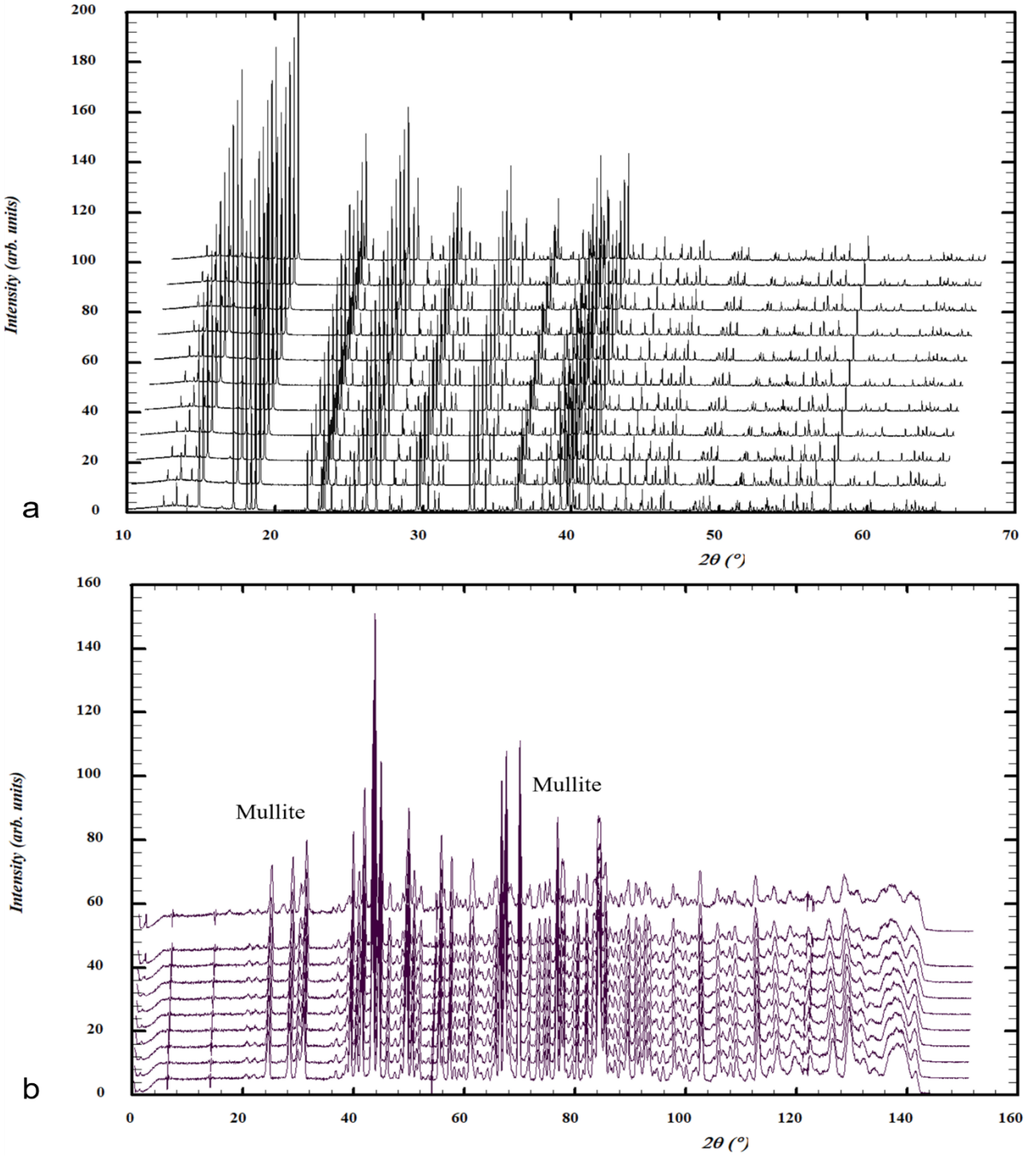

Figure 27a, b. Cascade plots of Baoshan topaz from Synchrotron (**a**) and Neutron (**b**) diffraction data. The samples were heated from 298 K and 330 K to 1273 K (heating rate 5 K and 2 K/min for Synchrotron and Neutron data collection, respectively). Powder diffraction patterns recorded every 100 K are also shown. In neutron analyses, the decomposition of the sample upon heating revealed the formation of mullite $Al_{4+2x}Si_{2-2x}O_{10-x}$. This image has been obtained with WinPLOTR from FullProf Suite

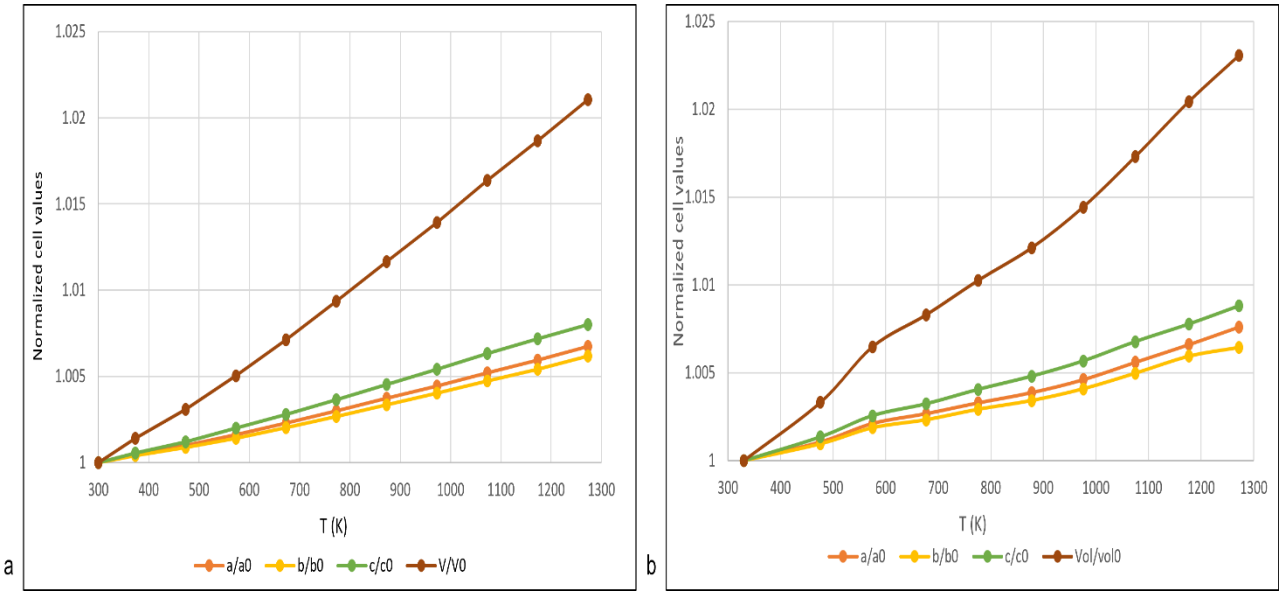

Figure 28a, b. Evolution of unit cell parameters for Bao topaz normalized with respect to room temperature values (a/a_0, b/b_0, c/c_0, V/V_0) from in situ synchrotron (**a**) and neutron diffraction (**b**) data. Standard deviation errors are within the symbol size.

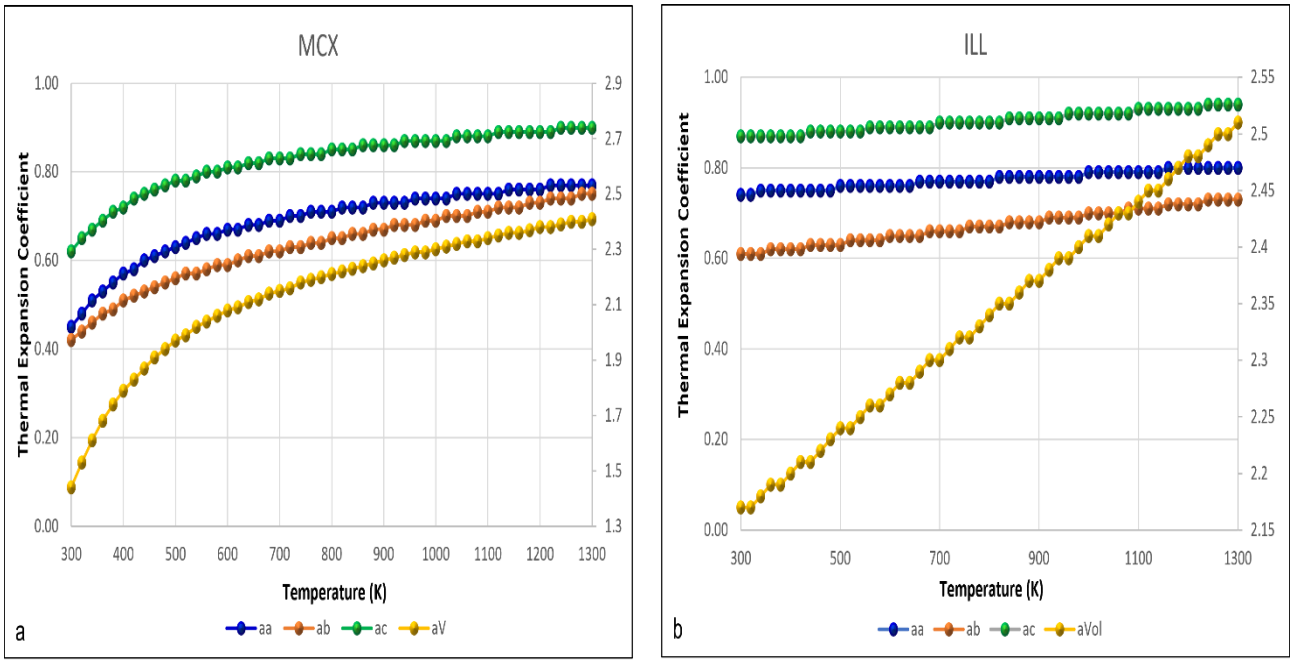

Figure 29a, b. Thermal expansion model for in situ heating of the Baoshan topaz, obtained from analyses in the temperature range of 298 to 1273 K and 356 to 1273 K for synchrotron (**a**) and neutron diffraction (**b**), respectively. Orange, yellow, green and blue symbols refer to Temperature *vs* Volume data selected for the EoS fitting (see text for details). Standard deviation errors are within the symbol size.

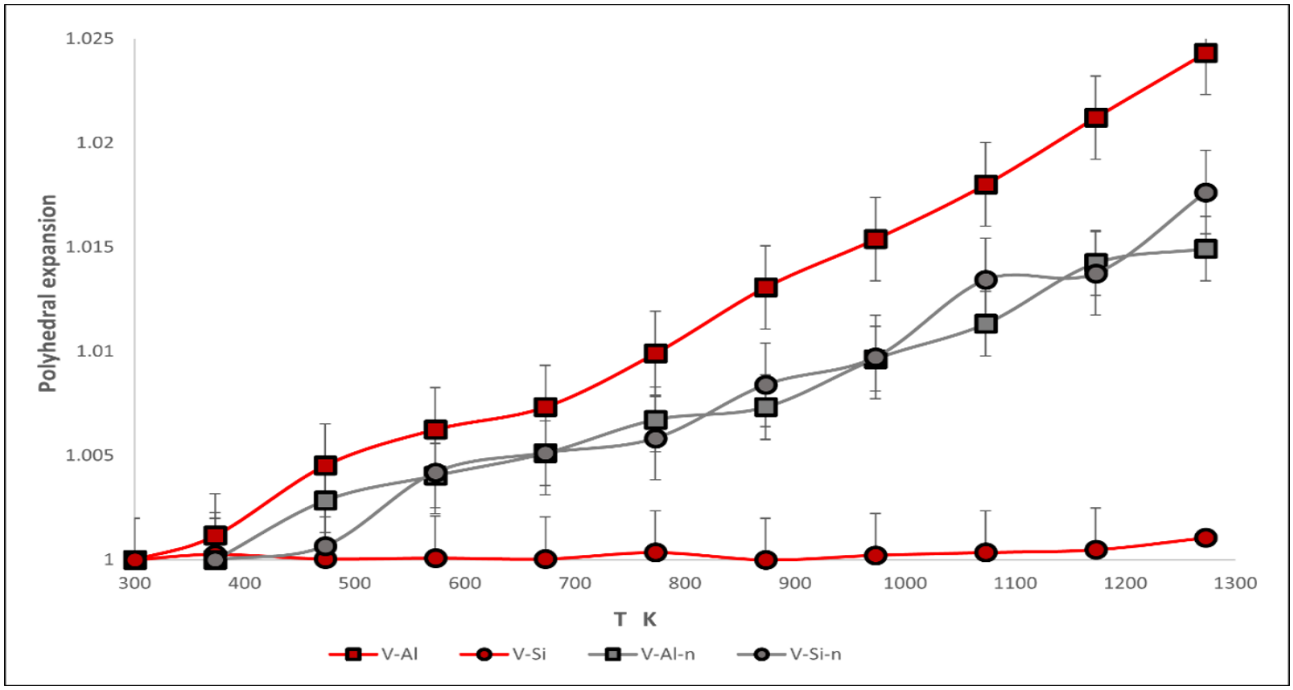

Figure 30. Polyhedral evolution of Bao topaz expressed as V/V_0, with V–Al and V–Si indicating octahedral and tetrahedral volume respectively, as obtained from synchrotron (red symbols) and neutron (grey symbols) data. More details are reported in Fig. 6. Standard deviation errors are represented by bar errors.

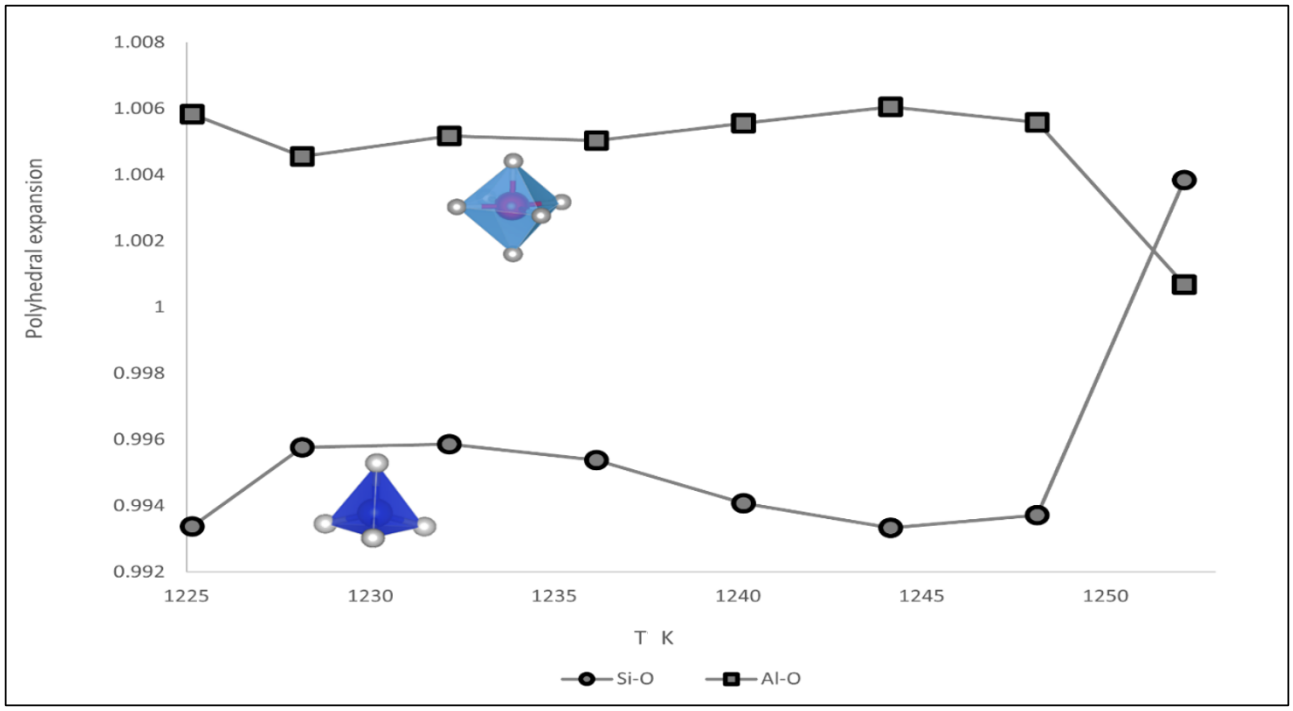

Figure 31. Polyhedral evolution of Bao topaz in the critical zone (1225–1273 K) expressed as V/V0 as obtained from neutron data. The octahedral expansion (square symbols) is continuously balanced by a tetrahedral contraction (circle symbol). For sake of clarity octahedra (light blue) and tetrahedra (dark blue) are also represented.

5.3 Laser Ablation Inductively Couple Plasma Mass Spectroscopy

5.3.1 Trace element characterization for Padre Paraíso topaz

The trace elements in Padre Paraíso topaz are not homogeneous, but despite spatial variations it is not possible to recognise a zoning. In these samples a good amount of lithophile and chalcophile elements have been detected. Among the lightest elements (Li, Be and B) I have recorded an enrichment for boron that runs from 0.8 to 4.6 ppm and 0.7 to 3.6 ppm for PadPar1 and PadPar3 respectively. Lithium is less present, but still spread along the transect with an amount that runs from 0.5 to 0.8 ppm and 0.9 to 2.2 ppm, PadPar1 and PadPar3 respectively. Both samples are very depleted in Be, that is present with a good grade of confidence in just one point for each sample. PadPar1 presents a higher amount of calcium total compared to PadPar3, 227.9 ppm and 145.9 ppm in average respectively; despite this, there is a certain difference if we distinguish between the calcium isotopes investigated. In fact, PadPar 1 is poorer than PadPar3 in Ca44; in addition to this Ca in PadPar1 has a more punctual concentration compared to the more uniform distribution in PadPar3. Titanium is present in both samples with a good homogeneity along the transect and goes from 47.1 to 59.4 ppm and 34 to 45.1 ppm, in Padpar3 and PadPar1 respectively. Iron is present in both samples with a good homogeneity in PadPar1 (62.9 to 68.3 ppm), while it is more scattered in PadPar3 (53.8 to 72.8 ppm). Fe content is pretty low if compared with other Minas Gerais state topaz like Gauzzi et al. (2018).

Gallium has a regular trend for both samples. It ranges from 7.8 to 8.4 ppm and 10.5 to 15.5 ppm, in Padpar3 and Padpar1 respectively. Germanium has the same grade of variability in PadPar3 with concentrations that can range from 44.2 to 48.4 ppm, while it goes from 50.5 to 57.5 ppm in PadPar1. Nb occurs very differently in the two samples. While in PadPar1 its content is well below 1 ppm (0.007 on average), in PadPar3 its content is quite variable, ranging from 13.8 to 18.1 ppm. The same thing occurs with tantalum, which content remain below 1 ppm (0.05 on average) in

PadPar1, while it remains fairly homogeneous in PadPar3 (3.9 – 5.7 ppm). In terms of rare earth contents, the two samples show different behaviour. Light rare earths are contained in both samples, with a total average content of 0.05 ppm for PadPar3 and 0.03 for PadPar1. As for rare earths, they are only contained in the sample PadPar3 (0.04 ppm total average), while they are below the detectable level in PadPar1. In figure 32 a and b, the analysed points for PadPar1 and PadPar3. The average content for the trace elements found in PadPar1 and Padpar3 is given in Table 14. Full analyses can be found in Appendix A1.

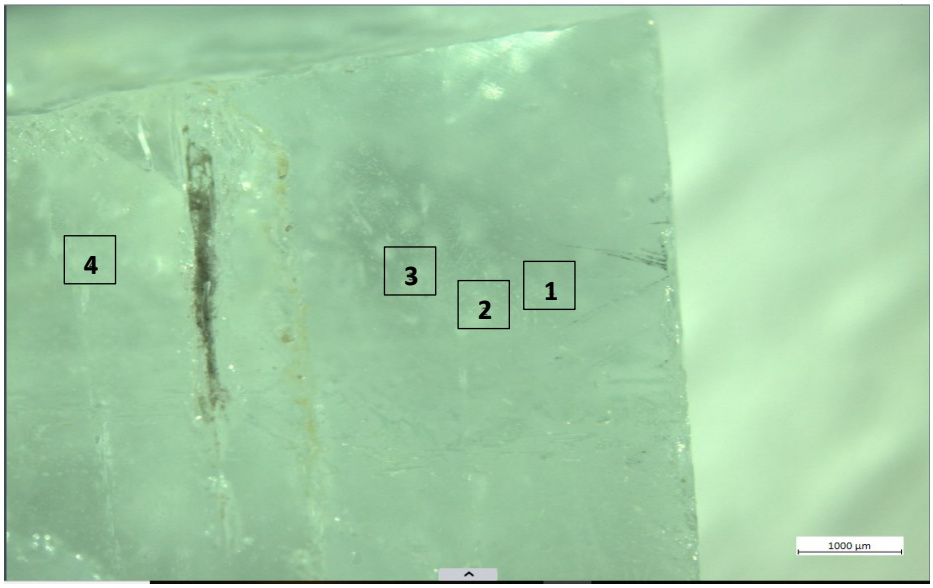

Figure 32 a, b. Collected points from PadPar1 (upper photo) and PadPar3 (lower photo). In PadPar 1 the points go from the outer part through the centre 1 to 4. In PadPar3 the points run from 1 to 5.

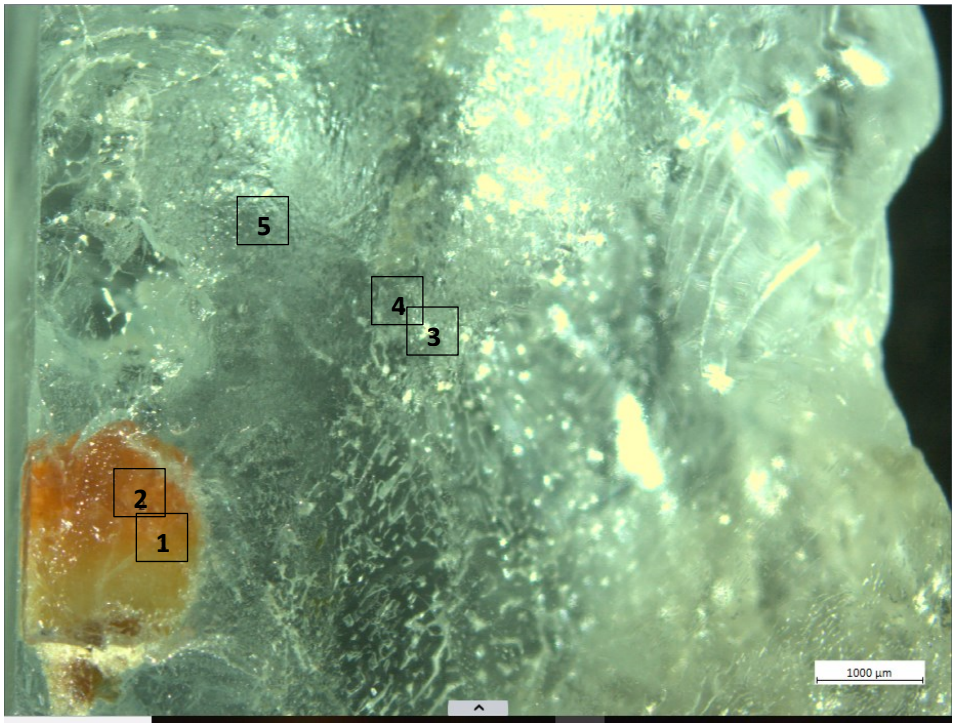

Table 14. Average content expressed in ppm for PadPar1 and PadPar3. The elements marked as (-) are below detection limit.

Element ppm	Padpar1 n=4	σ	Padpar3 n=5	σ
Li	0.695	0.21	1.61	0.5
Be	0.077	0.00	0.152	0.0
B	2.85	1.34	2.28	1.0
Mg	2.94	0.37	6.42	0.9
Ca	236	0.00	140	48.1
Sc	1.15	0.05	3.68	0.2
Ti	36.8	4.30	52.8	4.2
V	0.1262	0.04	0.0604	0.0
Cr	0.919	0.01	0.563	0.2
Mn	0.120	0.02	0.166	0.0
Fe	64.4	2.43	62.3	7.0
Co	0.0020	0.00	0.0037	0.0
Ni	0.0153	0.01	0.0213	0.0
Cu	0.0486	0.02	0.0378	0.0
Zn	0.233	0.00	0.272	0.1
Ga	12.0	1.91	8.14	0.2
Ge	53.5	2.50	46.4	1.7
As	0.307	0.00	0.228	0.2
Rb	0.0106	0.00	0.0219	0.0
Sr	0.0053	0.00	0.0162	0.0
Y	0.0010	0.00	0.0019	0.0
Zr	0.0023	0.00	0.0214	0.0
Nb	0.343	0.08	15.7	1.6
Mo	0.0078	0.00	0.0220	0.0
Cd	0.201	0.08	0.253	0.0
In	0.0020	0.00	0.0017	0.0
Sn	0.0715	0.00	0.371	0.3
Sb	0.0226	0.00	0.0335	0.0
Cs	0.0069	0.00	0.0132	0.0
Ba	0.0123	0.01	0.0134	0.0
La	0.0022	0.00	0.0026	0.0
Ce	0.0041	0.00	0.0044	0.0
Pr	0.0013	0.00	0.0025	0.0
Nd	0.0087	0.00	0.0254	0.0
Sm	-	-	0.013	0.0
Eu	-	-	-	-
Gd	-	-	0.006	0.0
Tb	-	-	-	-
Dy	-	-	-	-
Ho	-	-	0.0011	0.0
Er	-	-	-	-
Tm	-	-	-	-
Yb	-	-	-	-
Lu	-	-	-	-
Hf	-	-	0.0232	0.0
Ta	0.0528	0.03	4.76	0.7
W	0.6516	0.20	0.469	0.0
Au	0.0077	0.00	0.0134	0.0
Pb	0.0193	0.01	0.0562	0.0
Bi	0.0045	0.00	0.0058	0.0
Th	0.0030	0.00	0.0024	0.0
U	0.0021	0.00	0.0018	0.0

5.3.2 Trace element characterization for Baoshan topaz

The trace elements in the Baoshan topaz are equally distributed, with no great differences between the rim zone and the centre of the sample. In general, this topaz is not particularly enriched in trace elements and generally poor. Considering light elements, beryl is not present or at least below the level of detection. Lithium is generally under 1ppm, except in point five where it reaches 1.19 ppm, and the average content is 0.71ppm. Boron otherwise is more present and, apart from point 1 where the content is 0.74 ppm, it runs from 1.8 to 2.2 ppm. Bao1 presents a high amount of Ca that reach the 140.1 ppm in average; by the way it is possible to distinguish between the calcium isotopes investigated. Ca43 is much more present than Ca44, with contents of 116.5 and 15.3 ppm, respectively. Transition metals are generally present in content below the ppm, apart from Ti and Fe. Titanium is concentrated in two points, point 1 with 17.1 ppm and point 3 with 13.6. A sort of concentration in the rim is recognizable in this case and the average content is 10.4 ppm. Iron has a much higher concentration in point 1 (21.3 ppm), while from 2 to 5 it runs between 2.3 ppm to 15 ppm. Gallium is present in good amount and, as per Fe, also in this case we have a higher concentration in point 1 with 11.9 ppm and lower amount from 2 to 5 where the average is 5.7 ppm. A very different situation is given by germanium, in fact, this is one of the trace elements most commonly found in the Baoshan topaz sample. It reaches its maximum on point 2 (197.7 ppm) and the average content is 139.7 ppm. In terms of rare earth content, the sample does not show a different behaviour. Light rare earths are present with a total average content of 0.05 ppm for. As for rare earths in general the total average amount is 0.08 ppm. In figure 33 a and b, the analysed points for Bao 1. The average content for trace elements found in Bao1 is given in table 15. Full analyses can be found in Appendix A2.

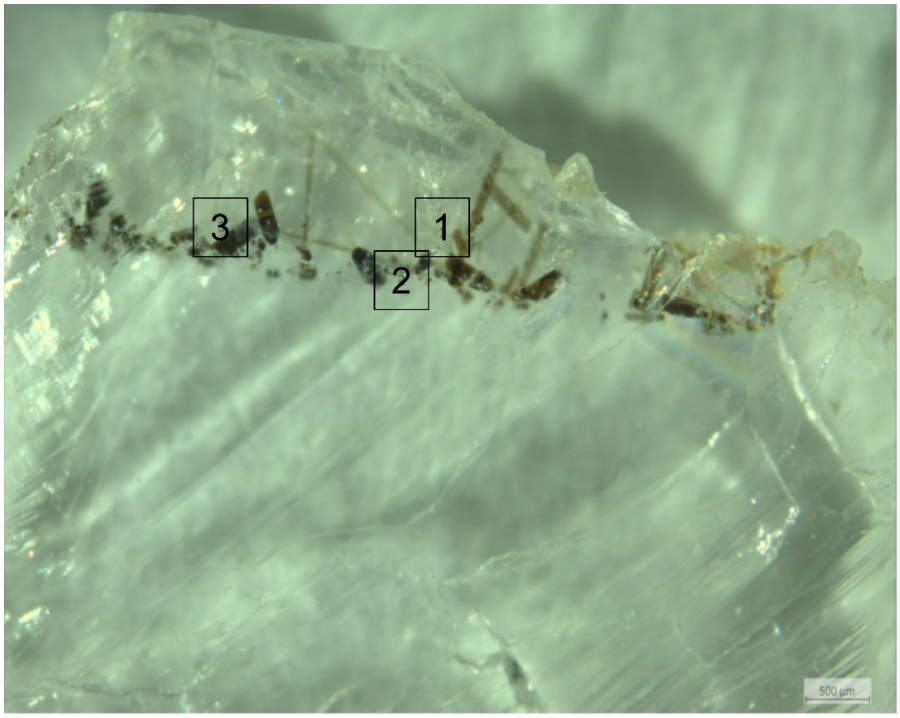

Figure 33 a, b. Collected points from Bao1. The points has been collected on the rim parallel to the elbaite inclusions (1, 2, 3) and in the inner part (4, 5).

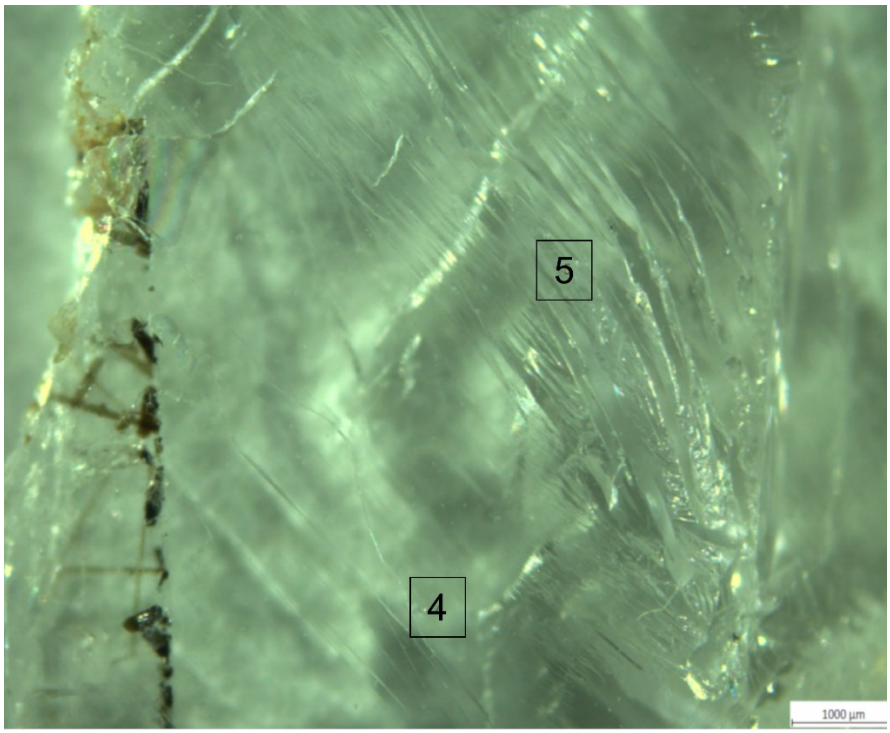

Table 15. Average content expressed in ppm for Bao1. The elements marked as (-) are below detection limit.

Element	Bao1 n=5	σ
Li	0.709	0.31
Be	-	-
B	1.99	0.15
Mg	1.91	2.11
Ca	132	40.35
Sc	0.711	0.59
Ti	10.4	4.29
V	0.0427	0.03
Cr	0.593	0.12
Mn	0.2185	0.06
Fe	12.9	6.13
Co	0.0050975	0.00
Ni	0.0281	0.01
Cu	0.137	0.08
Zn	0.460	0.32
Ga	6.91	3.13
Ge	140	42.85
As	0.086	0.00
Rb	0.0082	0.00
Sr	0.0082	0.00
Y	0.0529	0.05
Zr	0.0041	0.00
Nb	0.0230	0.01
Mo	0.0096	0.00
Cd	0.305	0.16
In	0.0020	0.00
Sn	0.0465	0.01
Sb	0.0330	0.02
Cs	0.0157	0.00
Ba	0.0113	0.00
La	0.0061	0.01
Ce	0.0178	0.01
Pr	0.0024	0.00
Nd	0.0189	0.01
Sm	-	-
Eu	-	-
Gd	-	-
Tb	-	-
Dy	0.0109	0.00
Ho	0.0065	0.00
Er	0.0082	0.00
Tm	0.0018	0.00
Yb	0.0064	0.00
Lu	0.0050	0.00
Hf	0.0062	0.00
Ta	0.0057	0.00
W	0.189	0.22
Au	-	-
Pb	0.0379	0.03
Bi	0.0041	0.00
Th	0.0052	0.00
U	0.0025	0.00

5.4 TwinMic - Low energy X-ray fluorescence (LEXRF)

5.4.1 XRF mapping on Padre Paraíso topaz

XRF mapping of PadPar topaz were obtained dividing the samples into 4 mini sections side by side along the radius (Figure 36). In this way, it is possible to observe the detected element from rim to core.

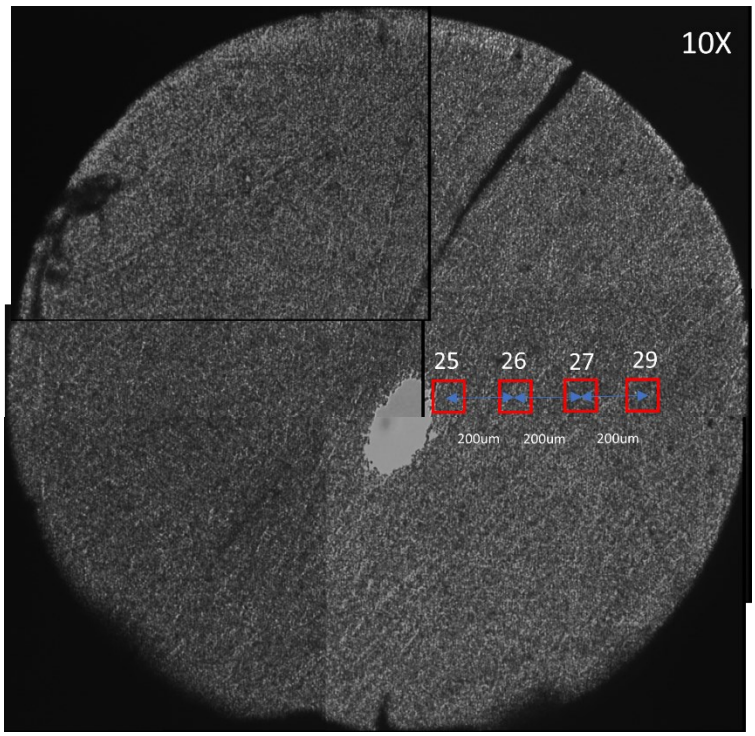

Figure 36. Image of Padre Paraìso sample, in red the four XRF mapping zone. Some internal features of the samples can be recognized, such as internal fracturation (N-NW sector), fluid inclusion (N-E sector). Blue arrows can be used as scale

Maps for Si show no particular trend for this element, the counts are regular along the transect. In the last section there is a predominance of green colour, but this is due to the higher counts respect to the other areas (Figure 37 a). The same homogeneity is showed by Al, with some blue spot (low count) probably due to substitution effect (Figure 37 b). Fluorine presence is recorded in all the sectors, with 26 and 27 that present a higher counting rate respect to 25 and 29 (Figure 37 c). Oxygen, like Si and Al is regular remains regular along the entire length of the transect (Figure 37 d). Ga and Ge, vicariant of Si and Al respectively, detected by XRF mapping appear very different from LA ICP MS analysis (Figure 37 e). While the LA ICP MS measurements recorded a higher content of Germanium than Gallium, in this case much higher counts are visible for Ga than for Ge. I also decided to report the

presence of arsenic in my analysis because of the anomalous count obtained (Figure 37 f). Previous studies (Ribbe and Rosenberg 1971; Ribbe 1982; Northrup and Reeder 1994) have reported the presence of As for Si in the tetrahedral site. While in the LA-ICP-MS analysis, arsenic was present in quantities of less than 1 ppm (Table 14), its presence seems to be very well detectable by XRF. It is likely that it enters the structure in place of aluminium, but only in the surface parts of the crystal, i.e., at the solid-liquid interface. Substitution of various cations into the octahedral and tetrahedral sites in topaz influences the OH stretching frequencies due to the next-nearest-neighbour (NNN) effects.

Figure 37 a, b, c, d, e, f, g. XRF map for Si, Al, F, O, Ga, Ge and As. The maps are n° 25 to 29 from left to right.

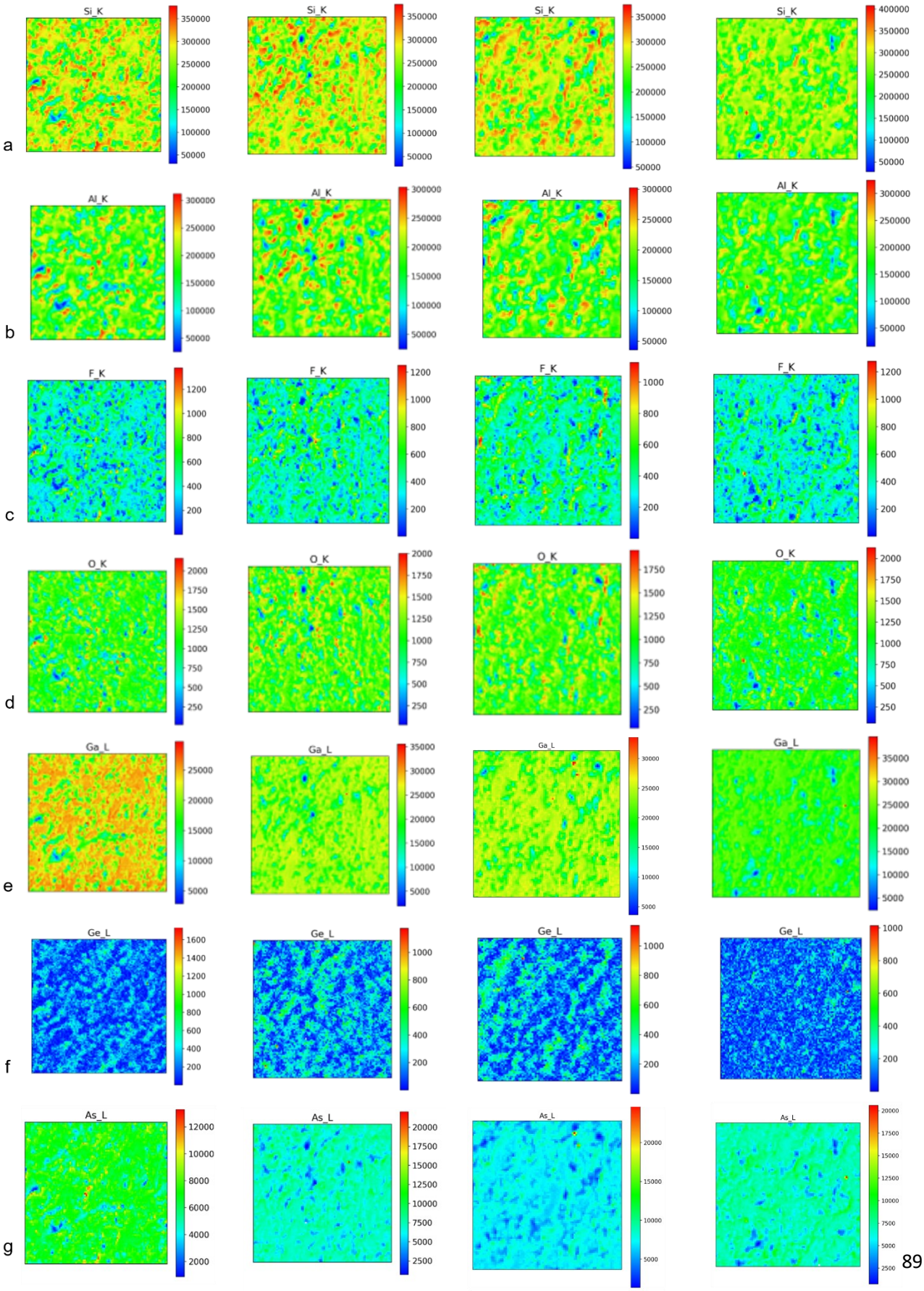

5.4.2 XRF mapping on Baoshan topaz

The XRF mapping dividing the sample into 4 mini sections side by side along the radius is shown in Figure 38. In this way, I would have the possibility to observe the element presence from rim to core. The sample has been prepared from the superficial part of the topaz crystal, on the crystal – environment interface.

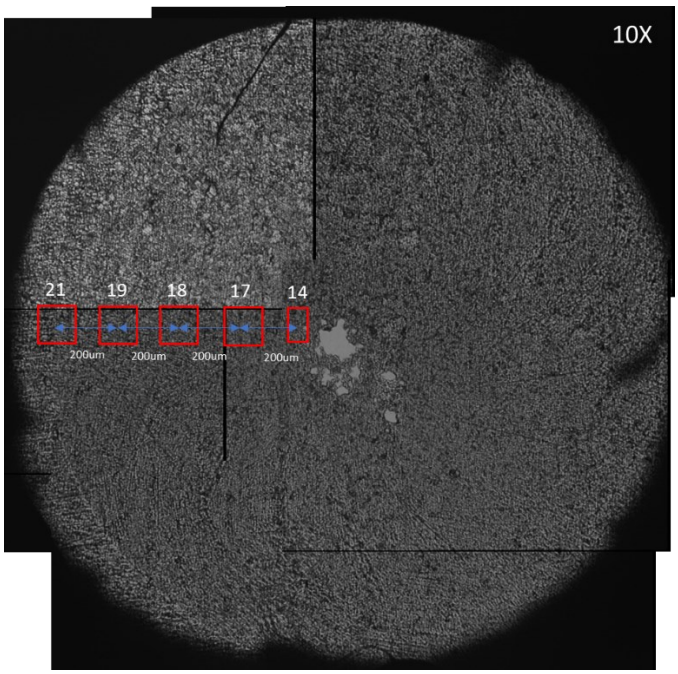

Figure 38. Image of Baoshan sample, in red the four XRF mapping zone. Blue arrows can be used as scale

The silicon presence in the sample is regular along the transect, with no particular trend from rim to centre. The apparent lower count in the third square is due to the different count scale (Figure 39 a). Aluminium shows the same grade of homogeneity, with the concentration spot nearly in the same places of Si (Figure 39 b). Fluorine presence is recorded in all the windows, with a banded distribution recognizable in 14, 17 and 18 is, while in 19 and 21 the Al and Si appears more homogeneous (Figure 39 c and Figure 39 d). The oxygen count rate is regular along the transect. Ga is widespread along the transect (Figure 39 e), at the same time, some spot attesting high Ge content are presents in 18 and 19 (Figure 39 f). Arsenic was present in quantities of less than 1 ppm, its presence seems to be very well detectable by XRF.

Figure 39 a, b, c, d, e, f, g. XRF map for Si, Al, F, O, Ga, Ge and As. The maps are n° 14, 17, 18, 19, 21 from left to right

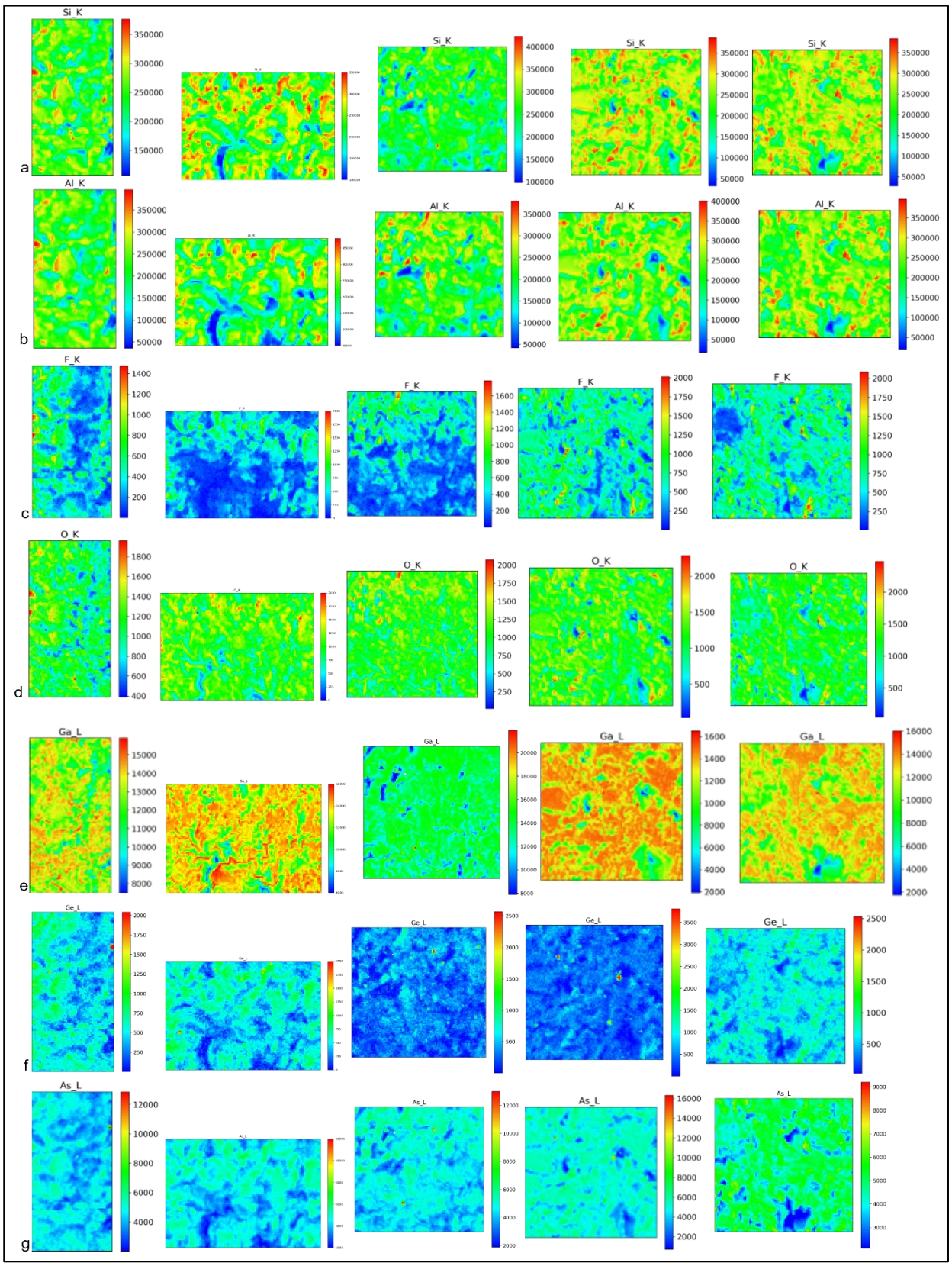

6. Discussion

6.1 Topaz to mullite phase changing

In Baoshan topaz, like in Padre Paraíso topaz, at high temperature there is a topaz destabilization and a progressive growing of mullite phase. The decomposition starts in the last steps of the heating process, around 1180K for PadPar topaz (Precisvalle et al., 2021) and 1225 K for Bao (Figure 40). Mullite, $Al_{4+2x}Si_{2-2x}O_{10-x}$, is an orthorhombic mineral belonging to *Pbam* space group. It is known in literature the topaz-mullite relationship (Hampar & Zussmann 1984, Day et al. 1995, Miao 1998, Peng et al. 2004, Monteiro and Sabioni 2014). By the way, the starting mechanism of this transformation was not well defined, Hampar & Zussmann (1984) and Monteiro and Sabioni (2014) linked this transformation to the loss of hydroxyl (around 1460 K, in Monteiro and Sabioni, 2014) and consequently the defluorination. Day at al. (1995), Miao (1998) and Peng et al. (2004), on the other hand, explain this phenomenon as an effect of de-fluorination. By the neutron diffraction analysis emerged how the two fractions are inversely related (Precisvalle et al.,2021)

In all the quoted studies, the topaz-mullite transformation happened at higher temperature than those recorded in our experiments for both PadPar and Bao samples. In Figure 39 a comparison of weighted fraction evolution for both samples is given. It is interesting to notice that at 1225 K there is the inversion of topaz and mullite content for PadPar topaz but also the starting of mullite formation for the Bao topaz.

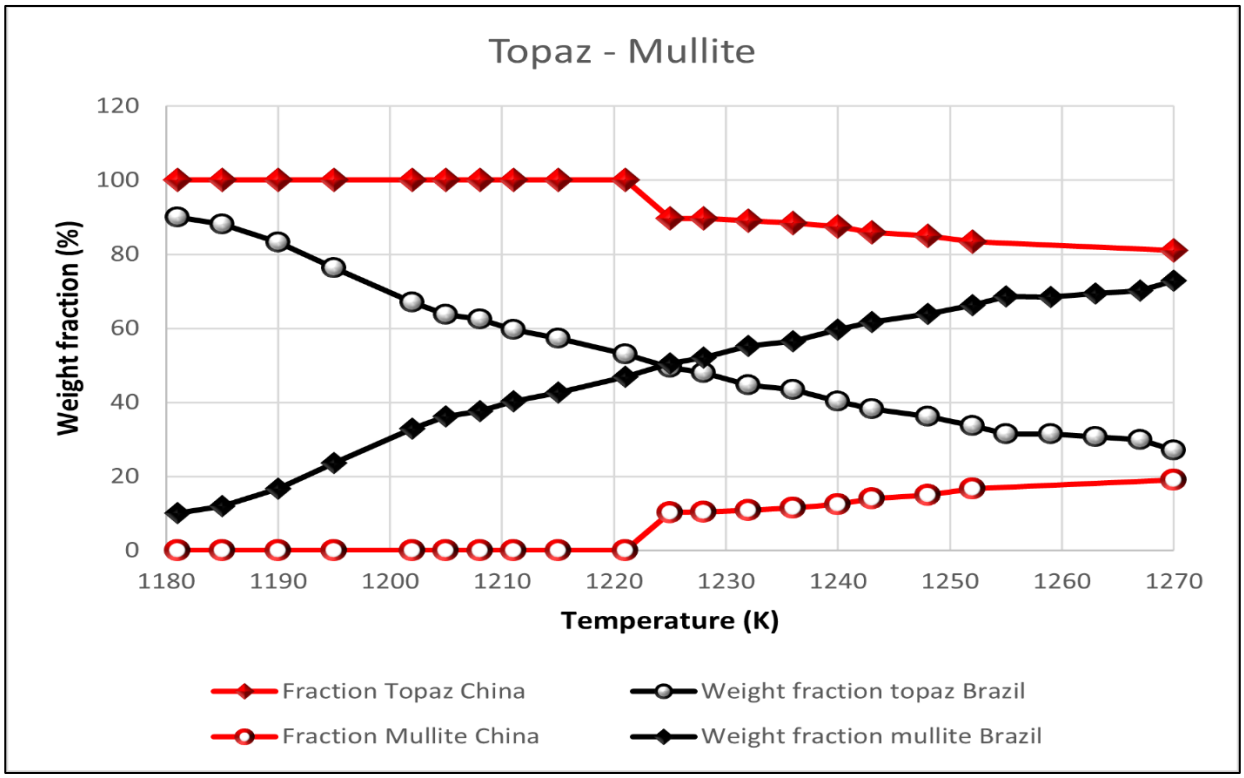

Figure 40. Comparison of weighted fraction evolution for PadPar topaz (black) and Bao topaz (red). The 1225 K seems to be a critical temperature for F, in fact here there is the inversion of topaz and mullite content for PadPar topaz but also the starting of mullite formation for the Bao topaz.

In PadPar, topaz population with an exceptionally low F content [OH/(OH+F) = 0.484], topaz transformation takes place pretty quickly and in 100-degree heating range three main steps can be recognized in the fluorine behavior. The first step is from 1181 K to 1225 K, where topaz destabilization starts opening the way to its full transformation in mullite. In this range there is no huge changes in F content, at the same time at 1225 K the weighted fraction for topaz and mullite is 0.49 (±0.02) and 0.51 (±0.02), respectively. The second step from 1225 K to 1252 K is where the mullite starts its growth over topaz, the fluorine content undergoes a big drop going from 1.036 a.f.u. to 0.764 a.f.u. The third step is another flat, similar to the first one, from 1252 K to 1300 K. Here, the weighted fraction for topaz goes from 0.36 (±0.02) at 1252 K to 0.30 (±0.02) while for mullite it goes from 0.64 (±0.02) to 0.70% (±0.02). At the same time, the fluorine content goes from 0.768 a.f.u. to 0.63 (Figure 41). At 1181 K topaz decomposition starts together with the appearance

of a mullite phase (up to 0.10 wt. fract). F remains strongly partitioned in topaz up to 1225 K but is reduced the weight fraction of this phase in the system by 50%. At higher temperatures, in a very narrow increasing interval, fluorine is largely released by the topaz structure, reaching 0.80 a.f.u. at 1252 K and concurrently mullite becomes the dominant phase (~ 70%). This F content is stabilized in the remnant topaz (~ 30%) up to 1270 K (Figure 41). From predictive calculation, the Padre Paraíso topaz will probably be completely turned to mullite around 1304 K.

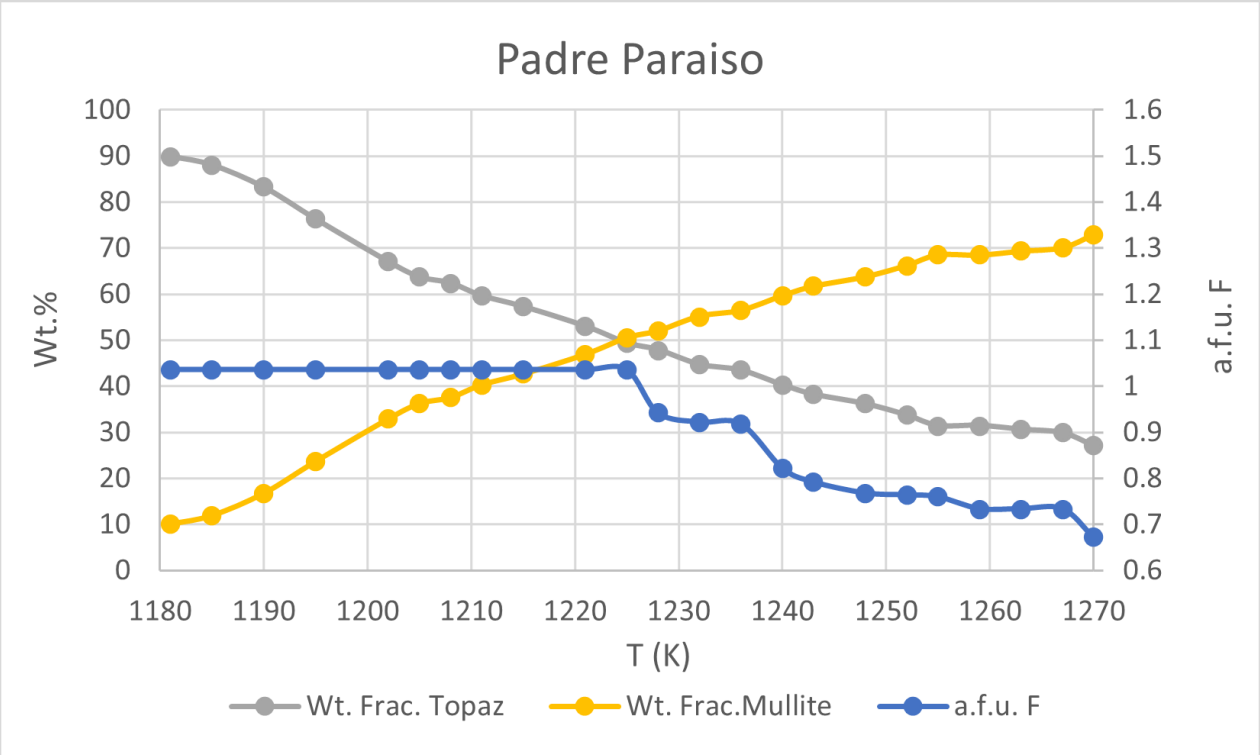

Figure 41. Fluorine behaviour in topaz-mullite transition zone for Padre Paraìso topaz from neutron diffraction refinements. F atoms in topaz (atomic formula unit, a.f.u.: blue pattern); weight fractions (wt. fract.) of topaz and mullite in grey and yellow patterns, respectively.

Also, in Baoshan topaz, which contains larger amount of F with respect to the PadPar topaz [OH/(OH+F) = 0.24], the stepping trend for F is respected, even if the topaz – mullite transformation is less evident.

The first step of topaz degradation here starts at 1225 K and continues to 1232 K. In this range there is a sort of plateau with near no fluorine loss. Also, the weighted fraction for topaz and mullite shows very poor differences with topaz that goes from 90% (±1) to 89% (±1) and mullite from

10% (±1) to 11% (±1). The second step from 1232 K to 1243 K is steeper, here there is also the biggest loss in topaz against mullite. By the way, in contrast to what happens to PadPar topaz, here there is no inversion in the content of topaz and mullite. The fluorine content undergoes a drop from 1.325 a.f.u. to 1.292 a.f.u. In the end, the F content goes down to 1.243 a.f.u, while the topaz wt.% and the mullite wt.% are 83% (±1) and 17% (±1), respectively (Figure 42). At 1225 K topaz decomposition starts together with the appearance of a mullite phase (up to 10 wt. fract%). F remains strongly partitioned in topaz up to 1232 K but is reduced the weight fraction of this phase in the system by 7%. Very little fluorine is released by the topaz structure, reaching 1.24 a.f.u. at 1273 K and concurrently mullite appears as minor phase (~ 17%). This F content is stabilized in the remnant topaz (~ 83%) up to 1273 K (Figure 42).

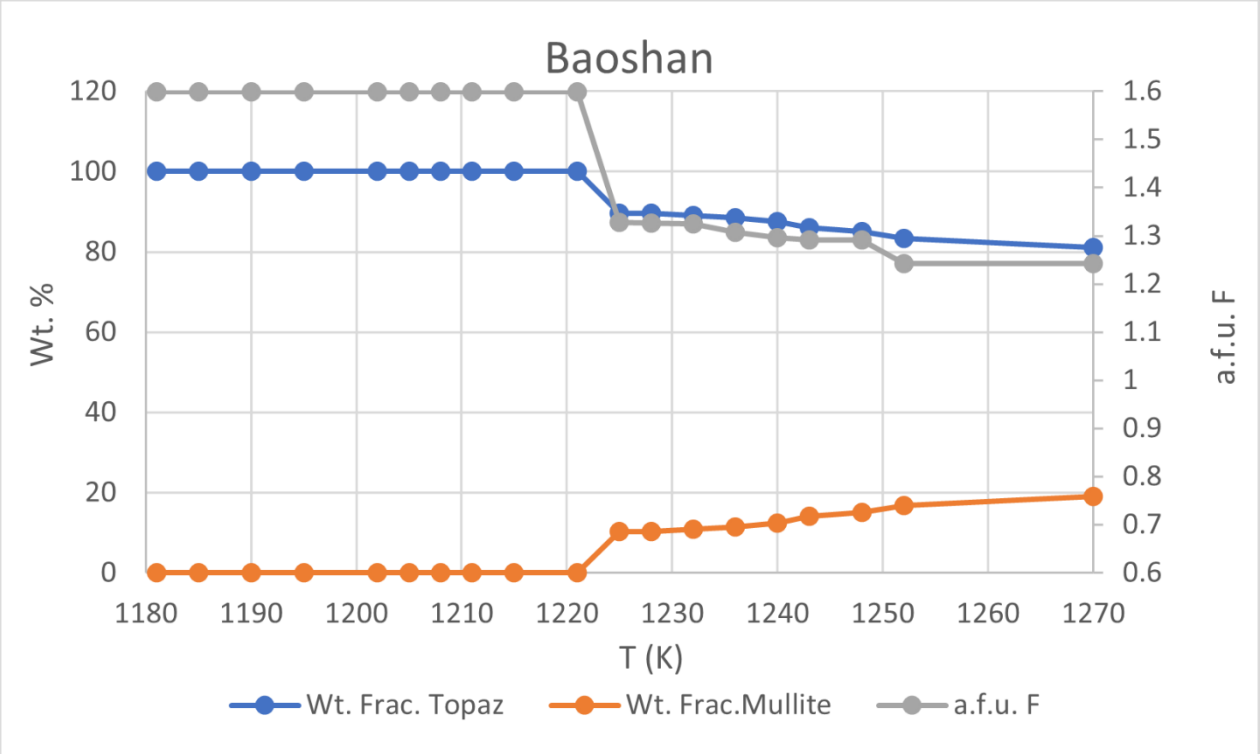

Figure 42. Fluorine behaviour in topaz-mullite transition zone for Baoshan topaz from neutron diffraction refinements. F atoms in topaz (atomic formula unit, a.f.u.: grey pattern); weight fractions (wt. fract.) of topaz and mullite in blue and orange patterns, respectively.

In this work, the transformation of topaz into mullite was reconstructed for the first time through diffraction analysis. In previous work, this phase change was only observed in its final step after a long calcination phase (Hampar & Zussmann 1984, Day et al. 1995, Miao 1998, Peng et al. 2004, Monteiro and Sabioni 2014). It is therefore possible to state that the temperatures measured here are the actual temperatures at which the transformation takes place and that this is mainly linked to the percentage of fluorine contained in the topaz.

6.2 Relationship between mineral chemistry, structure, and formation environment

A natural crystal contains several pieces of information that can be used to learn about its evolutionary history and, most important, its forming environment. In the case of topaz, this can come not only from its inclusions (whether fluid, gaseous or solid), but also from its bulk trace element content and distribution, its structural characteristics and the ratio of fluorine to oxygen. Combined synchrotron and neutron diffraction data collected in this study allowed us to infer with a rigorous analytical strategy that the real symmetry of PadPar and Bao topaz is orthorhombic *Pbnm.* For the investigated samples there are no evidence of any different symmetry at any given temperature. Hydrogen atoms are hosted in only one site in good agreement with those reported for a natural topaz, with differences <2σ (Gatta et al. 2006; Zemann et al. 1979). Based on the neutron diffraction data, the F-amount corresponds to ~1.03 a.f.u. for Padre Paraíso topaz and ~1.6 a.f.u. for Baoshan topaz. In view of this, the chemical composition can be inferred as being $Al_{1.92}Si_{0.96}O_{4.00}F_{1.032}OH_{0.968;}$ (OH/(OH+F) = 0.484) and $Al_{1.99}Si_{0.99}O_{4.00}F_{1.599}OH_{0.394;}$ (OH/(OH+F) = 0.198) respectively. For both samples the fluorine content (10.94% PadPar, 15.16% Bao) determined by neutron diffraction results in very good agreement with that measured by EDS, but both remarkably lower with respect to the values obtained

with the correlation equation (~18.5 % wt. and 19.1 % wt., respectively) proposed by Alberico et al. (2003). This empirical relationship between F contents and lattice parameters is widely used to estimate the fluorine content in topaz but our results, as well as those reported by Gatta et al. (2006) reveal that this empirical correlation between F contents and lattice parameters is not always satisfactory. Unit cell parameters increase as the temperature increases up to 1181 K indicating a positive thermal expansion that dominate this stage of the experiment. Above this temperature, in PadPar topaz both fluorine content and topaz crystallinity decrease, and mullite starts its growth over topaz, while in Bao topaz this reaction is shifted at higher temperature (1225 K). According to Peng, and Sorrell (2004) mullite nuclei may form randomly on the surface of powdered topaz or pellets from the very beginning thus protecting it from further decomposition. This reaction is self-catalysed by SiF_4, and its occurrence is strongly dependent on several factors such as air flow, heating rate and fluorine concentration. The analytical strategy applied here, therefore, was successful in determining the fluorine content in topaz, and its behaviour with increasing temperature. The F/OH ratio in this phase is crucial not only for the forming gem process, but also to better understand the circulation of fluids (H_2O/HF) in the forming environment.

6.2.1 Variation of $\log(f H_2O/f HF)^{fluid}$ of the inferred fluid based on F–OH concentrations of topaz.

The topaz forming system is H_2O saturated peraluminous, melt or/and fluid(s) with low calcium and F contents >1 wt.% (Burt et al., 1982; Lukkari et al., 2006) In the late and post-magmatic evolution of any intrusive events, the residual melts (volatile - saturated in composition) and fluids tend to escape to higher structural levels, or lose their identity due to the interaction with the already crystallized phases, or due to a continuous interaction with the host rock (i.e.,: Thompson 1995; Bakker and Elburg 2006; Smirnov 2015) For the sake of clarity, in the following sections we use the equilibrium equations and formalism applied to the fluid state.

The OH-F substitution in the topaz solid solution was estimated to not exceed X_{OH} = 0.5 [X_{OH} = OH/(OH + F)] due to proton–proton avoidance (Barton, 1982). However, OH-rich topaz with X_{OH} = 0.54 occurred in samples from ultrahigh-pressure rocks of the Sulu terrane, eastern China (Alberico et al 2003), as well as in high pressure experimental products, indicating that depending on the P–T–X-conditions, topaz might be stable along the complete (OH,F)-solid solution series (Wunder et al 1999, Wunder et al. 1993).

The effective ionic radius and electronegativity of F and OH are very close (Shannon 1976, Zhu & Sverjensky 1992), therefore it is reasonable to assume an ideal site mixing of F and OH in various F-OH minerals, including topaz (Zhu & Sverjensky 1992).

Biotite is the most widely used mineral to estimate the halogen content of fluids in various magmatic-hydrothermal systems, according to the experimentally well calibrated exchange reaction (Munoz & Swenson 1981):

$$xBio(OH)_2 + 2HX = xBio(X)_2 + H_2O$$

where X= F and Cl and xBio = Mg cation numbers/sum octahedral cation numbers in biotite. Various empirical equations are thus proposed to estimate the halogens fugacity for the fluids in equilibrium with biotite (Bao et al. 2016, Selby et al. 2000), and the application of this method facilitated the investigation of the F–Cl–OH partitioning between biotite and fluids in various magmatic-hydrothermal systems (Selby et al. 2000, Coulson et al 2001, Marshall & Oliver 2008, Monteiro et al. 2008, Afshooni et al. 2013, Zhang et al. 2016, Markl & Piazolo 1998, Andersson et al. 2018, Gauzzi et al. 2018).

Following the same line of reasoning, we calculated the fluorine fugacity [expressed as the ratio $\log(fH_2O/fHF)$] of possible fluids (or H_2O-HF saturated) coexisting with PadPar topaz and Bao topaz. The refinement of F/OH occupancy from neutron data, allowed the consolidation of the chemical data for the F contents in both topazes. Padre Paraíso topaz is anomalously fluorine-poor, with X_{OH} = (0.456-0.476), close to the physical proton–proton avoidance. As mentioned above, low to very low fluorine content (X_{OH} = 0.54) of natural topaz was observed in ultrahigh pressure metamorphic

terrains (Zhang et al. 2002) but is rarely observed in topaz of late or post magmatic origin (i.e., as in Minas Gerais fields, Gauzzi et al. 2018). Notwithstanding, it is worth noting that among the worldwide late or post magmatic topaz, (Dewonck et al. 1998, Breiter et al. 2013, Agangi et al. 2014, Agangi et al. 2016) those from the Padre Paraíso pegmatite are undoubtedly a fluorine poor type (PadPar: F ~ 10.0-10.94 wt.% versus worldwide average F ~ 18 wt.%). On the other hand, the Baoshan topaz presents a fair amount of fluorine in their structure (F ~ 15.09-15.16 wt.%), even if a bit below the world average.

To the best of my knowledge, both the topazes suites (from Minas Gerais pegmatites and the Tengchong-Baoshan block (China) are recognised as minerals of gemmological interests, but so far, they have never been investigated for crystallochemical and geochemical purposes.

On the basis of the distinct geochemical features of the two topaz suites (Table 16) and the resulting topaz-mullite relationship from the previous section, the destabilisation temperature of the topaz has been interpreted as the potential temperature for topaz formation in a F-H_2O saturated environment. Therefore, it is intriguing to determine the fluid activity (mainly OH and F) in equilibrium with topaz as those studied in this thesis.

It is high challenging to extrapolate the ambient of mineral formation from the crystal itself, since it is often doubtful that collected samples truly represent the in-situ conditions at which minerals formed. However, due to the fairly constant major-element composition of this mineral species, the trace elements contents, OH/F concentration ratio and fully characterized crystal structure (site occupancy) may reflect the nature of the fluid composition from which topaz formed.

The $(fH_2O/fHF)^{fluid}$ are calculated from the concentrations of F, and OH on the mixed site in topaz octahedra using the empirical equations proposed by (Barton 1982, Barton et al. 1982), relating the equilibrium constants of F-OH exchange in topaz:

$$Al_2SiO_4(OH)_2+2HF = Al_2SiO_4(F)_2+H_2O$$

The thermodynamic properties describing the partitioning of F-(Cl)-OH between minerals and late or post magmatic fluids are from (Shannon 1976, Dolejs & Baker 2004).

The resulting T- $fH_2O/fHF)^{fluid}$ space (Figure 43), that traces the fluid composition in equilibrium with topaz in the range of *T* between 573 and 1473 K at constant P = 1 Kbar (Barton, 1982), reveals distinct ambient for the two topaz suites. The topaz – mullite transformation happened at different temperature, 1181 K and 1225 K for PadPar and Bao, respectively. This maximum temperature is interpreted as the potential initial crystallization temperature of topaz fluid system. The fluorine content, expressed as the ratio $log(fH2O/fHF)^{fluid}$, of possible fluids (or H2O-F saturated silicic melt) coexisting with the topaz, was modelled on the basis of the partitioning of F – OH-(Na) behaviour between fluorine bearing minerals and late- post magmatic pegmatitic fluids/gresenization reaction (Figure 43).

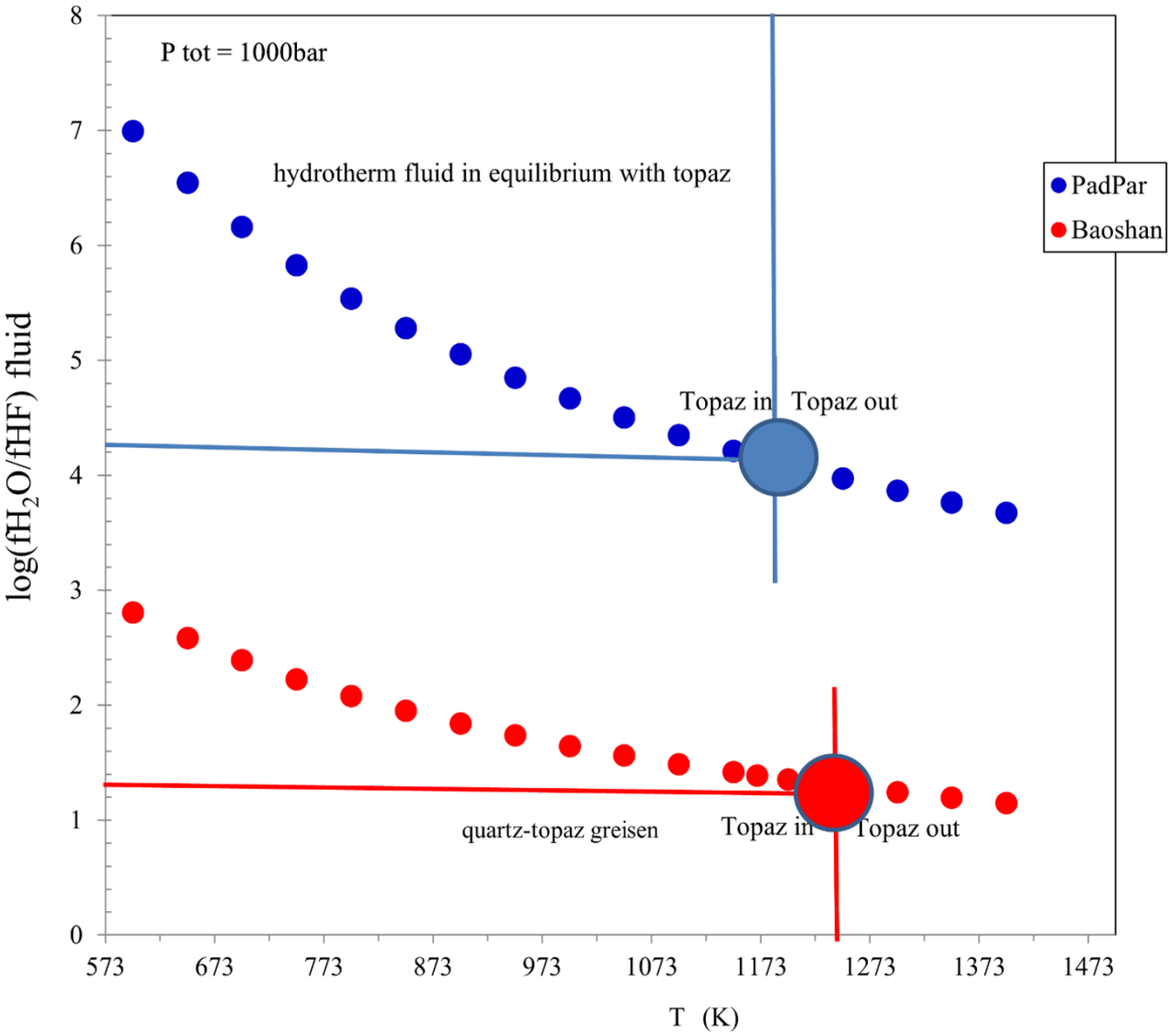

Figure 43. Equilibrium condition for Baoshan topaz (red) and Padre Paraìso topaz (blue). Both dots represent topaz appearance temperature for the two systems.

As expected the topaz-forming fluids of Padre Paraíso is richer of water with respect to Baoshan in the explored temperature range: the Padre Paraìso ($fH_2O/fHF)^{fluid}$ varies from ~ 7 log units (T=~573 K) to ~ 4log units (T=~1373 K), whereas the Baoshan $fH_2O/fHF)^{fluid}$ varies from ~ 2.8 log units (T=~573 K) to ~ 1.5log units (T=~1373 K) The neutron data indicate the temperature of topaz destabilization (Figure 1). This temperature is here interpreted as also the potential temperature of initial topaz formation. In such a view, it is possible to infer that Padre Paraíso topaz nucleates at ~1148-1181 K from a water rich /fluorine poor fluid ($(fH_2O/fHF)^{fluid}$ ~ 4.5 log units.). This value is

coherent with a OH/F ratio as observed in typical pegmatitic-hydrothermal type fluids (Barton,1982; Dolejš and Baker, 2004; Benkó et al. 2018); instead Baoshan topaz started to form at higher temperature ~1203-1225 K from a water poor /fluorine rich fluid $((fH_2O/fHF)^{fluid} \sim 1.2$ log units. This lower value (and relatively high temperature of topaz formation) suggests that Baoshan forming fluids is more influenced by fluorine activity as observed for late magmatic fluid that acts as metasomatic agents for the gresenization reactions. (Barton,1982; Dolejš and Baker, 2004; Benkó et al. 2018). Moreover, the slow increase of OH/F with cooling temperature to equilibrate Baoshan topaz (Figure 1), reveals a metasomatic reaction with, most probably, a granite, rather than a direct crystallization from fluids. In the same line of reasoning the lower initial temperature formation and the rapid increase of OH/F decreasing temperature suggest the PadPar topaz forming fluid has large compositional variations as expected in hydrothermal crystal precipitation.

Another clue to the origin of the two topaz populations is the trace elements measured by LA-ICP-MS (Table 1). All the samples present elemental contents that are in line with the inferred origins. The Baoshan topaz has higher contents of Ge with respect to PadPar topaz. Germanium is main vicariant element for Si (and to lesser extent Al), that is a typical enrichment for minerals from greisen-type deposits from alteration of S-type granites (Breiter et al. 2014, Launay et al. 2021). This result is perfectly in line with that reported by Guo et al. (2014), who in their study on the tin ore deposits of the Tengchong-Baoshan block analyse the granitoids in the area of origin of our samples and describe them as originating from S-type granites. Other indicators of the greisen origin of Baoshan topaz are the presence of Fe and Ti, Ga and the related depletion of Zn, W and Sn that crystallise into other phases such as cassiterite and other oxides (Breiter et al. 2014, Guo et al. 2014, Launay 2021).

On the whole, the Padre Paraíso topaz has remarkably higher contents of trace element contents with respect to Baoshan topaz. The presence of Li – Be – B and Mg (Bradley et al 2017, Gauzzi et al. 2018) suggests a late-stage fractional crystallization from hydrothermal/ pegmatitic fluid. (Bradley et

al 2017, Gauzzi et al. 2018). The high content of Ti and the enrichment of Nb with respect to Ta also infer that the original hydrothermal/ pegmatites fluid could be the mixed type rare-elements low pressure granitic pegmatites (as the Padre Paraíso pegmatites (Černý, 1991, Zagorskyet al. 1999, Černý and Ercit 2005, Martin and De Vito 2005, Muller et al 2007; Pedrosa-Soares et al. (2011). Another good hint of pegmatitic origin is the Fe content, which is a strong geochemical signature of Padre Paraíso gemstones mineralization and like in Padre Paraíso aquamarine, could be related to the strong light-blue coloration (Achtschin 1999; Gandini et al. 2001; Ferreira et al. 2005; Kahwage & Mendes 2003, Pedrosa-Soares et al. 2011). Gallium and germanium, on the other hand, are not particularly indicative of the origin of topaz (apart the decoupling from Ga and Ge contents observed in the case of greisen deposits) as they are compatible elements with similar partition coefficients (Simon et al., 2017; Korh et al., 2017) in magmatic and hydrothermal systems. In any case, the samples analysed here present a quantity of Ga and Ge in line with the content of other topazes originating in pegmatites and granites (Duck 1986, Duck and Cohen 1986, Northrup and Reeder 1994, Breiter and Kronz 2004, Breiter et al 2013).

6.3 Substitution and adsorption phenomena from Twinmic results

As seen in the Twinmic results section for both PadPar and Bao topaz, it is possible to underline a different content for the analysed elements but not a different behaviour in their distribution on the sample surface. Although the sample has been slightly polished in order to be more visible in X-rays and make the mapping more reliable, it is still reasonable to assume that the area analysed here is the outermost area and therefore the one most affected by the effect of the fluids present in the ore formation environment. The distribution of major elements such as Al, Si, O and F is even in fairly all the maps. This is also confirmed by the correlogram made from XRF counts. All these major elements present a direct correlation between them, as it is expected to be silicon and aluminium, which are in structure in tetrahedral and octahedral coordination respectively, are arranged in chains along the *c* axis in a 1:2 ratio.

In figure 44a and 44b some examples for PadPar and Bao Si-Al correlogram are reported.

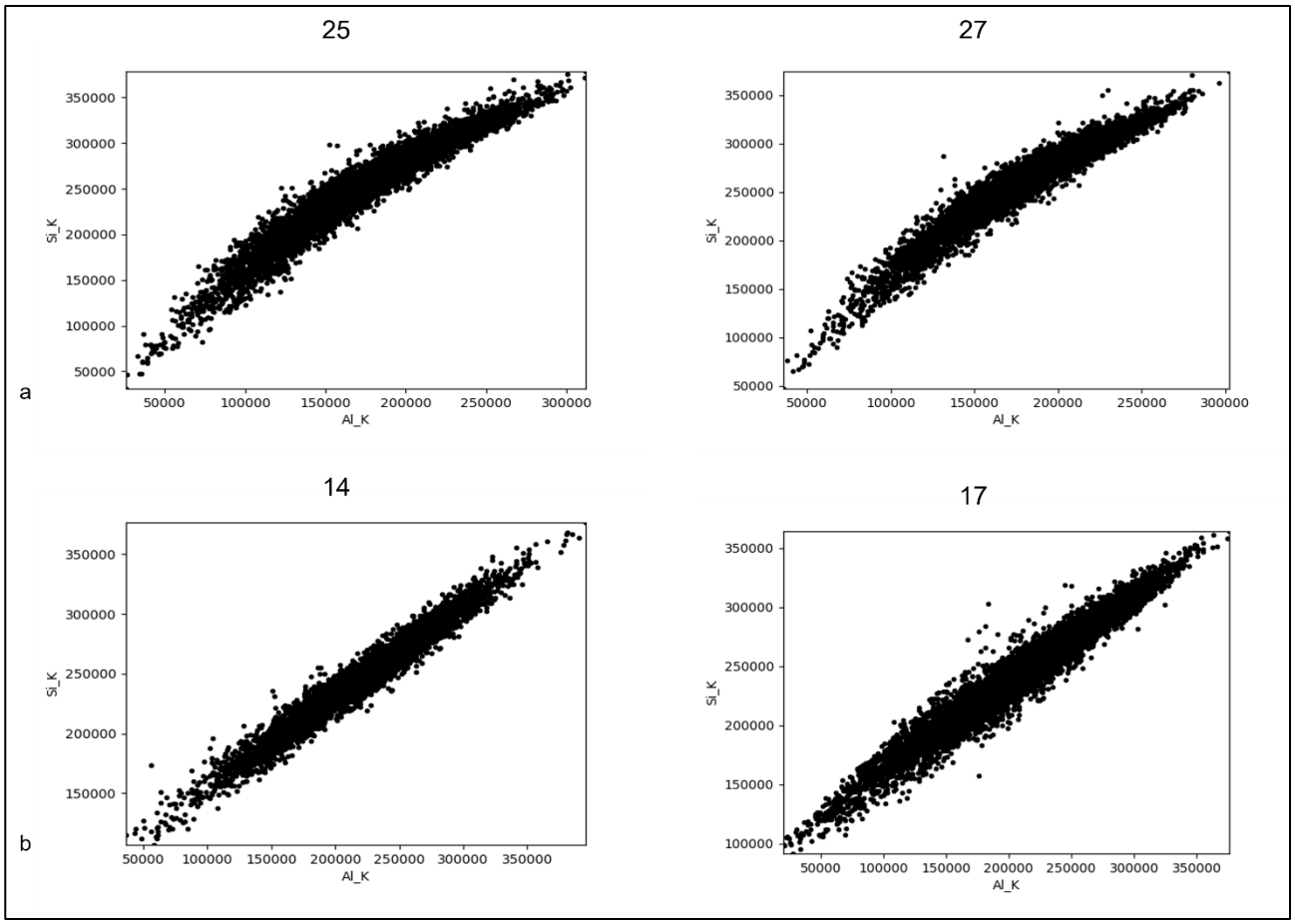

Figure 44 a, b. Two examples of Si-Al correlogram from XRF mapping. In **a** it is reported map 25 and 27 from PadPar topaz, in **b** 14 and 17 from Bao. The direct correlation at similar counts means that the elements are both present with no particular behaviour.

The same trend is followed by O and F. Anyway, an interesting insight given by this experimental technique is the possibility to investigate the O and F distribution inside the topazes. It is well known from literature that in mixed OH/F topaz they are randomly distributed and unpredictable without Raman or FTIR analyses (Zemann et al 1979, Pinheiro et al. 2002, Gatta et al. 2006, Watenphul et al 2010).

The micro-XRF maps taken for this work have shown this effect directly, showing the distribution of both O and F. In these maps where the concentrations are represented by coloured scale grade, dark green indicates areas where only oxygen is present, while red indicates areas where only fluorine is present (Figure 44). The different shades then represent areas where both elements are present. In general, the dominant colour is green, as oxygen is present in greater quantities than fluorine in the

structure of topaz. However, there are some areas, coloured yellow, where F and O are equally distributed. Although the indication we obtain is purely qualitative, since any standard were available, it does show that these elements do not follow a distribution trend within the sample, but rather are distributed in a disorderly fashion over the surface of the topaz. This occurs in both Padre Paraíso and Baoshan topazes and can be presented as visual confirmation of what has previously been reported in literature through probability calculations from FTIR analyses. An example is given in figure 45a and b.

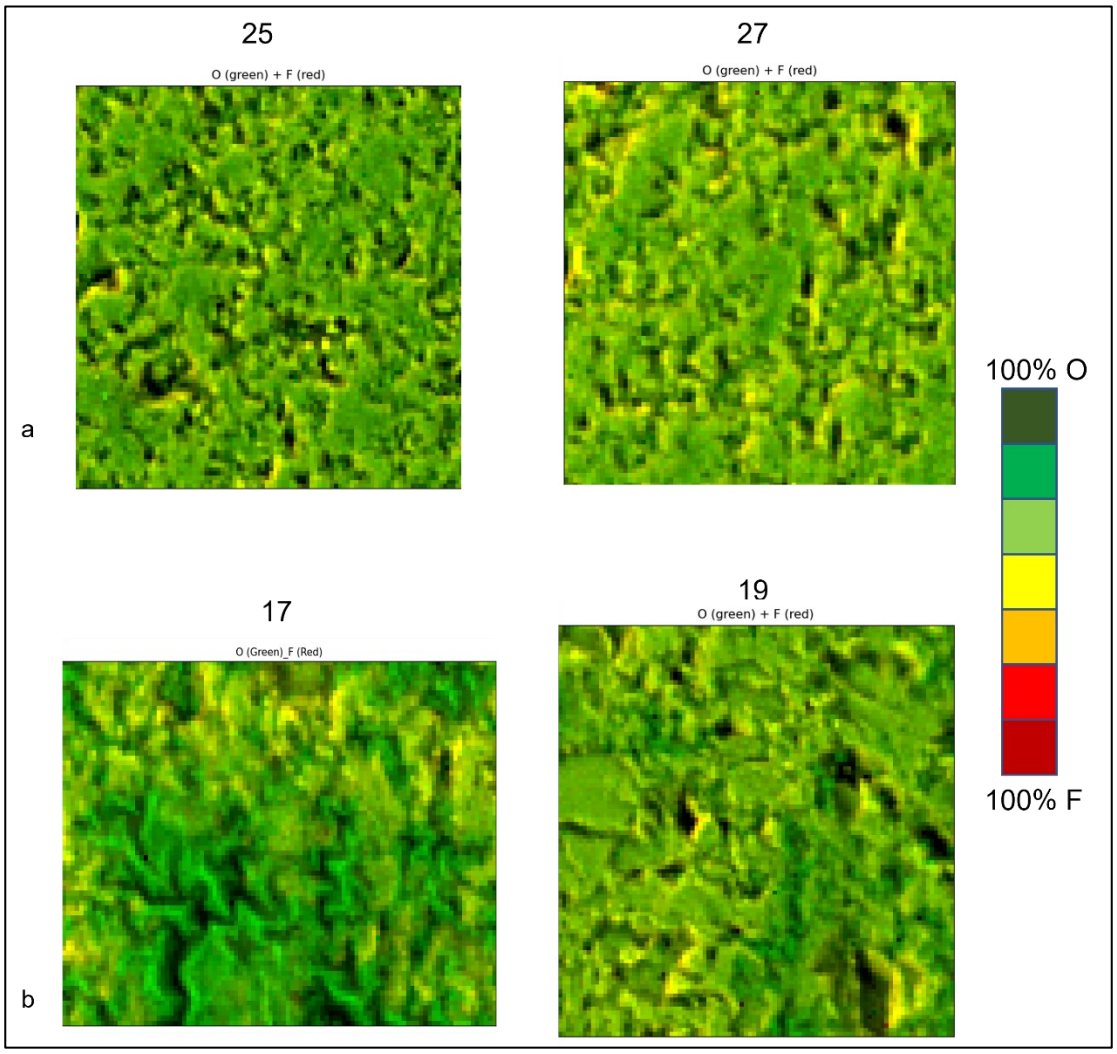

Figure 45 a, b. Spatial distribution of oxygen and fluorine in maps 25 and 27 from PadPar (**a**) topaz and 17 and 19 from Bao (**b**) topaz. The colour scale on the right gives the idea of the presence of each element in any part of the map. The ripple-like forms are representative of the sample surface.

The behaviour of the trace elements revealed by the XRF mapping is substantially different. From Northrup and Reeder (1994) it is known that on the basis of ionic potential (i.e., electrical charge (z) to the radius (r) of an ion), Ga^{3+} can substitute Al and Ge^{4+} can substitute Si in topaz structure. These substitutions are well known and largely investigated (Northrup and Reeder 1994, Gatta et al. 2006) Instead, As behaviour is not well understood yet, As^{5+} may replace Si, with charge balance accommodated on an adjacent Al site. Substitution of As^{3+} for Al^{3+} is also possible. The chaotic distribution in the Ga-Al correlogram for both Padre Paraíso and Baoshan topaz (Figure 46 a, b), suggests the effective substitution of Ga in Al site.

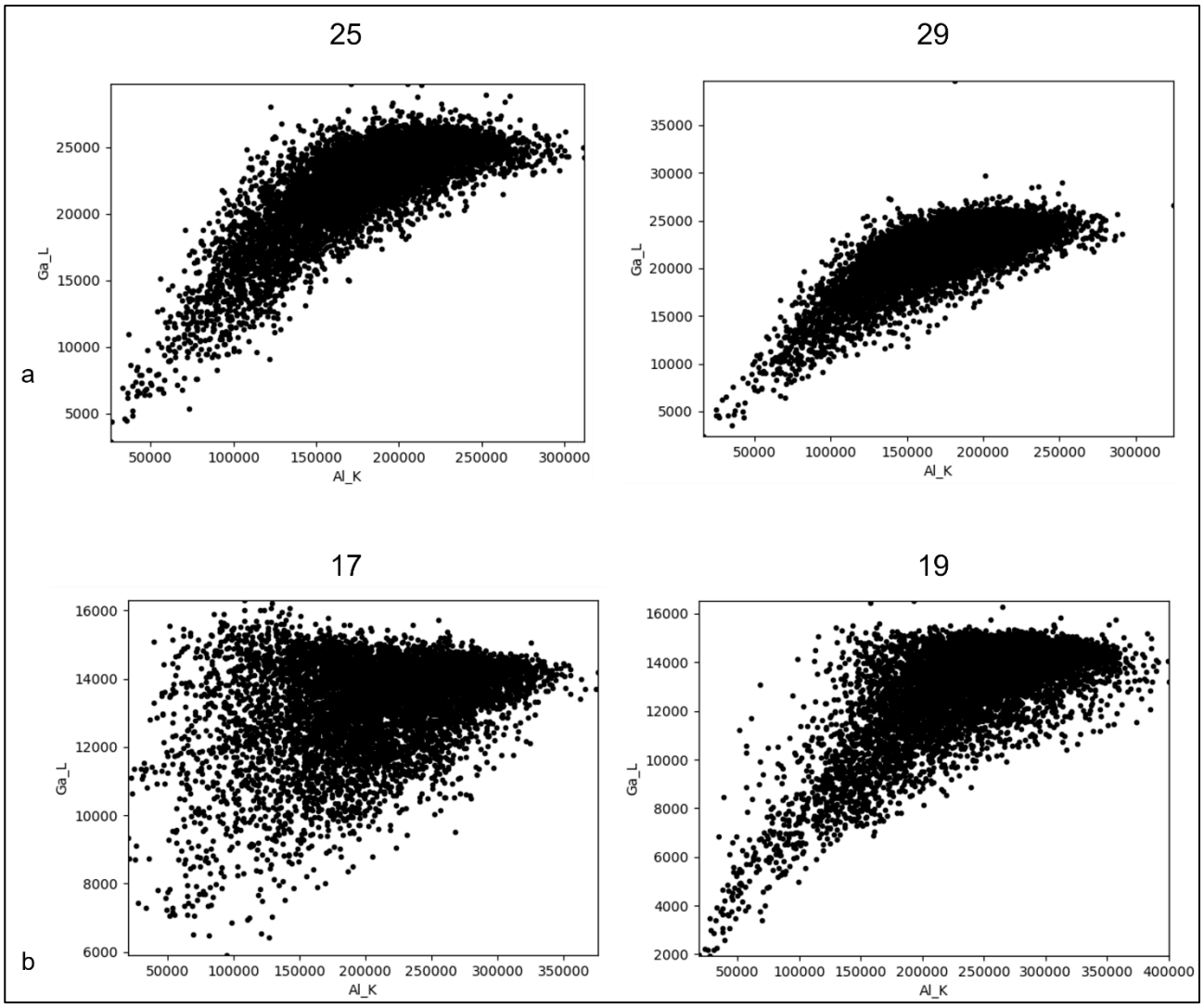

Figure 46 a, b. Two examples of Ga-Al correlogram from XRF mapping. In **a** it is reported map 25 and 29 from PadPar topaz, in **b** 17 and 19 from Bao. The points uneven distribution suggests the substitution in Al sites of Ga.

Another hint of this elemental behaviour is given by the distribution maps of Al *versus* Ga. It is interesting to notice that these substitutions are not equally distributed along all the transect, but they are randomly present along it. Distribution maps of Al and Ga are given in figure 47 a and b for PadPar and Bao respectively.

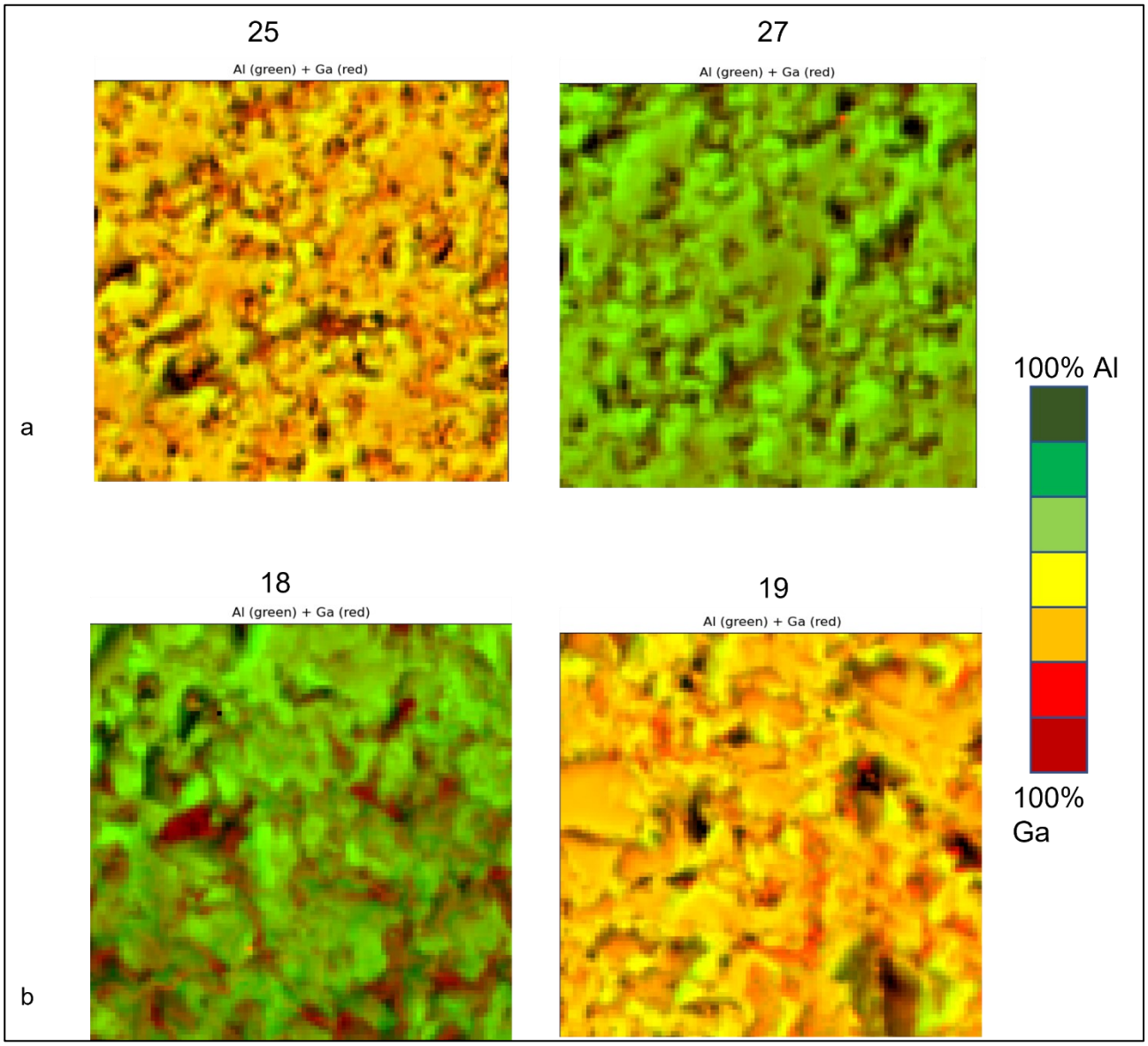

Figure 47 a, b. Spatial distribution of Al and Ga in maps 25 and 27 from PadPar (**a**) topaz and 18 and 19 from Bao (**b**) topaz. The colour scale on the right gives the idea of the presence of each element in any part of the map. The shades of colour suggest Ga substitutions at expense of Al, in some areas of the map these are particularly concentrated.

The same behaviour can be observed for Ge and Si (Figure 48 a, b). In this case it was not possible to observe the substitutions through correlograms, due to the few counts of Ge. But as in the case of Al *vs* Ga, the substitutions of Ge for Si are also visible on the distribution maps. Also, in this case the substitution happens randomly along the sample transect. These distribution maps for Si and Ge are showed in figure K a and b for PadPar and Bao respectively.

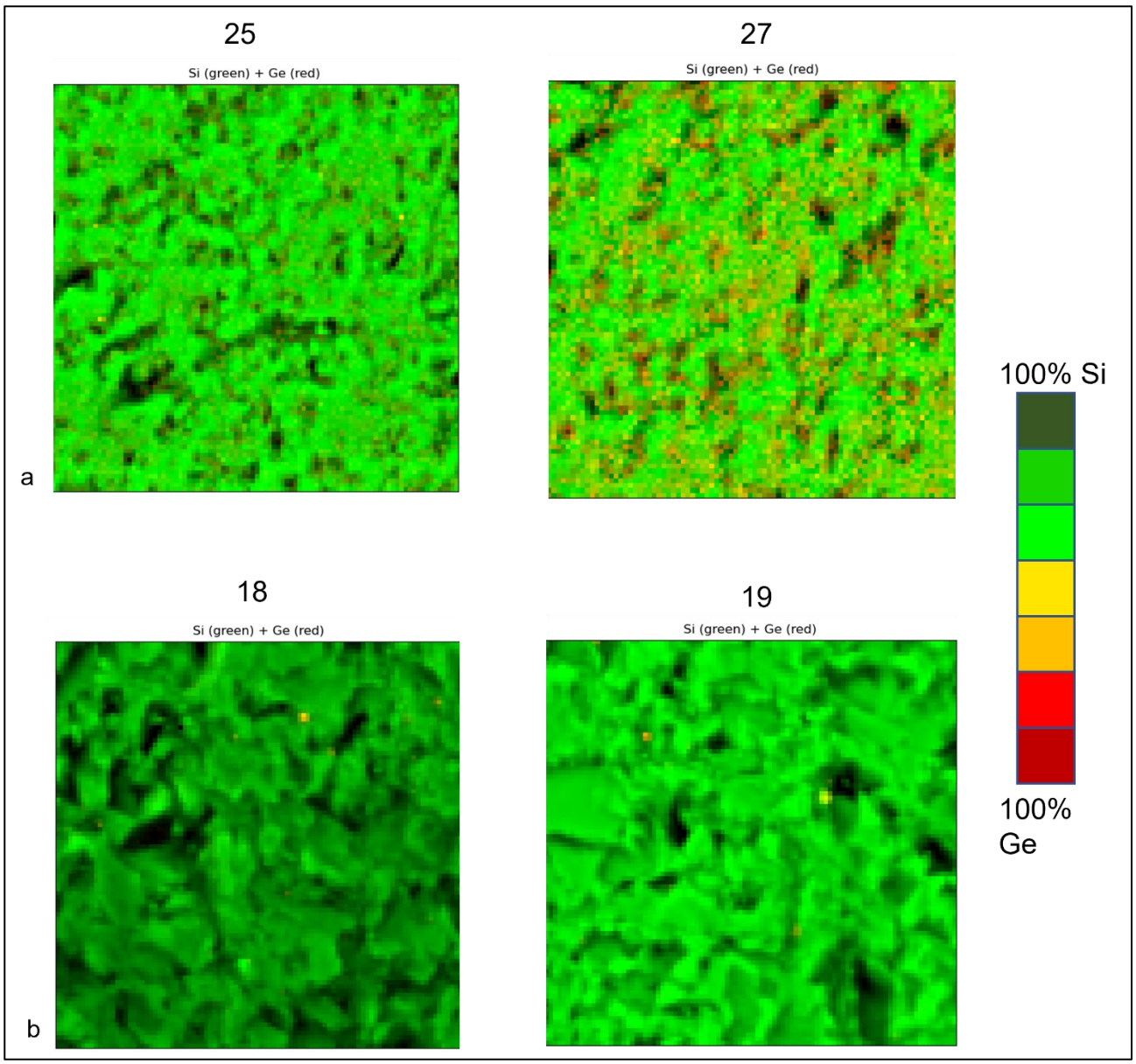

Figure 48 a, b. Spatial distribution of Si and Ge in maps 25 and 27 from PadPar (**a**) topaz and 18 and 19 from Bao (**b**) topaz. The colour scale on the right give the idea of the presence of each element in any part of the map. The shades of colour suggest Ge substitutions at expense of Si.

Coming to As, which is the last trace element detected by mapping, it is not possible to recognize any sort of substitution. The correlogram of As vs Al shows a direct correlation between the counts of the two elements, like in Si *vs* Al, showing no evidence of substitution (Figure 49 a and b). In order to see whether arsenic could actually occupy the position of Si (Ribbe and Rosenberg 1971; Ribbe 1982; Northrup and Reeder 1994) in these samples, a correlogram As *vs* the direct competitor for the Si substitution, Ge, were proposed. from this, it is evident, two different behaviours of arsenic for the two topaz population; Brazilian topaz show no direct correlation between As and Ge. This can be explained by the entrance of As into the tetrahedron in place of Si (of which Ge is a vicariant) (Figure 50 a). On the other hand, Baoshan topaz shows a positive linear relationship between As and Ge (Figure 50 b). Altogether, indicates that As does not enter in structure as vicariant of Si or Al, but it is located in a totally different position. It is reported that in some cases topaz can host atoms in the cavities adjacent to octahedra with a zeolite-like extra framework configuration (Gatta et al. 2006). This type of adsorption may justify the presence of arsenic in Baoshan topaz. The complete sets of correlograms are reported in Appendix B 1 and B 2 for PadPar and Bao, respectively; the elemental distribution maps for PadPar and Bao are reported in Appendix C 1 and C 2

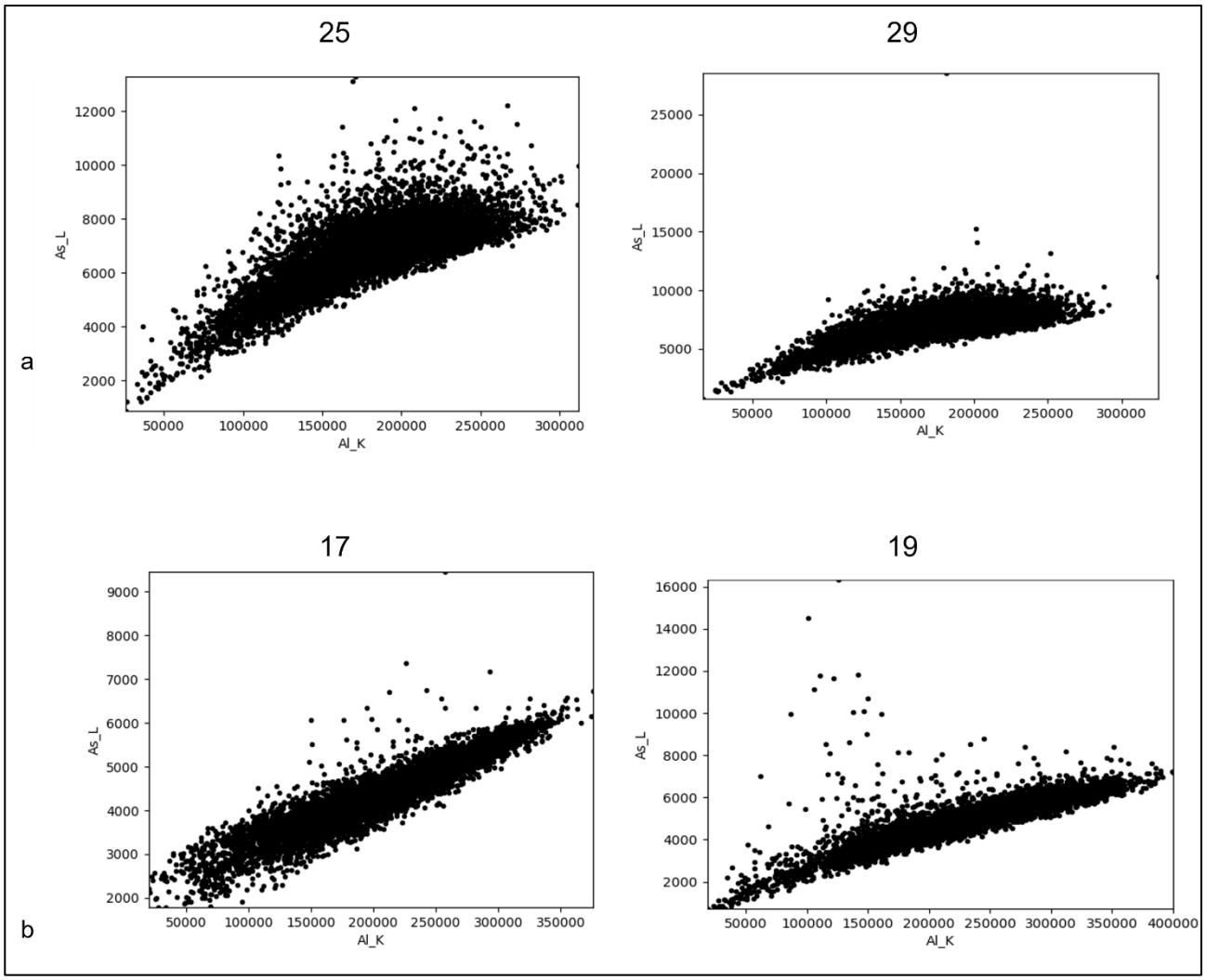

Figure 49 a, b. Two examples of As-Al correlogram from XRF mapping. In **a** it is reported map 25 and 29 from PadPar topaz, in **b** 17 and 19 from Bao. The points are distributed with a direct linear relationship which suggests there is no substitution between As and Al.

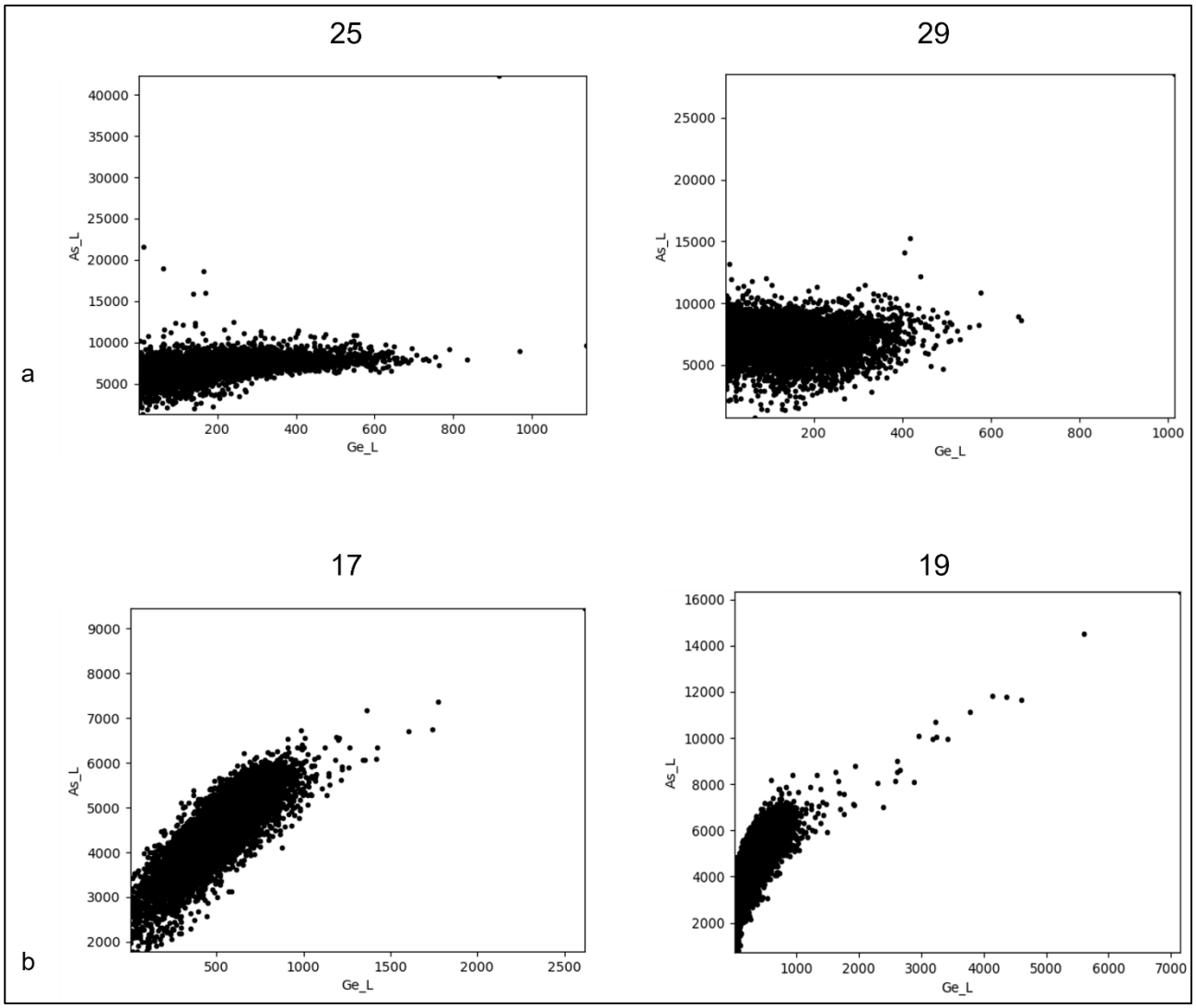

Figure 50 a, b. Two examples of Ge-As correlogram from XRF mapping. In **a** it is reported map 25 and 29 from PadPar topaz, in **b** 17 and 19 from Bao. The correlograms for PadPar show no correlation between As and Ge, suggesting a substitution in Si site. On the other hand, the direct correlation showed in Bao correlograms suggest that As does not enter directly in structure. From Gatta et al. (2006) is reported that cavities in topaz can host atoms with a zeolite-like configuration, As in Bao topazes is probably settled in these cavities through adsorption.

7. Conclusions

The successful strategy to combine EDS microanalyses with synchrotron X-Ray and neutron powder diffraction in situ measurements (from RT to 1273 K) allowed us to accurately determine the mineral structure of topaz, and to reconstruct backwards both the environment and the possible conditions of formation The results, then, have been subsequently supported by the trace element analysis and the micro-XRF mapping helped to better understand the setting-up for trace elements on topazes' surface. The fluorine content obtained from the EDS analyses reveals an average F content of ~1.05 a.f.u for Padre Paraíso topaz and ~1.53 a.f.u. for the Baoshan topaz. These values are in pretty good agreement with those estimated from the refined occupancies of neutron diffraction data of ~1.03 a.f.u (Padre Paraíso) and ~1.59 a.f.u (Baoshan) with OH/(OH+F) = 0.484 (Padre Paraíso) and 0.24 (Baoshan). These results are different from the fluorine amount based on cell parameters and cell volume correlation theorized by Ribbe et al. (1971) and Alberico et al. (2003). In fact, the fluorine calculated according to those correlations turns out to be overestimated with respect to the chemical investigations, especially with respect to Padre Paraìso topaz (F18-19% according to Alberico et al. (2003) and Ribbe et al. (1971) against ~11% in this study). Differently from the PadPar topaz, in Bao it has also be recorded a small amount of Na between 0.02 and 0.01 wt.%.

The study of trace elements by means of micro-XRF mapping showed good results about distribution of major and trace elements on topaz surface. Indeed, here for the first time it has been possible to have a direct observation of elemental substitution in tetrahedral and octahedral site and elemental adsorption. In particular, in the correlograms and the colour maps:

1. The random distribution of O and F in octahedra is demonstrated

2. Al-Ga and Si-Ge substitution has been observed; they showed a random distribution along the topazes' surface.

3. Arsenic, for the first time, has been shown to be included in topaz either as a substitute for Si (as in the case of Padre Paraíso topaz) or absorbed in the cavities between octahedrons (as in Baoshan topaz)

The in situ analyses from both neutron and synchrotron data showed an expansive trend for the topaz structure evolution through heating. It is interesting to notice the different behaviour for Si tetrahedra at increasing temperature for Baoshan topaz; here for the first time a negative αVo has been observed in a topaz. From in situ neutron diffraction, the appearance of mullite phase is observed at different temperature in the two topaz populations (1181 K and 1225 K for Padre Paraíso and Baoshan, respectively). In this work, for the first time the progressive transformation of topaz into mullite was recorded by diffraction analyses unlike previously, where this transformation was only observed at the end of a calcination cycle

The temperatures obtained thus were interpreted as the potential temperatures for the crystallisation of a topaz, depending on the amount of fluorine in the structure, and thus on the fluorine availability in the environment in which the topaz crystallises.

So, from these temperatures and F contents obtained from the neutron diffraction it has been possible to reconstruct the nature of topaz forming fluid system. In order to do this, it has been modified the Barton equation for biotite and adapted to topaz. The fluorine content, expressed as the ratio $\log(f\mathrm{H_2O}/f\mathrm{HF})^{fluid}$, of possible fluids (or H2O-F saturated silicic melt) coexisting with the topaz, was modelled on the basis of the partitioning of F-(Cl)-OH behaviour between fluorine bearing minerals and late- post magmatic pegmatitic fluids/gresenization reaction.

In such a view, it is possible to infer that Padre Paraíso topaz nucleated at ~1148-1181 K from a water rich /fluorine poor fluid ($(f\mathrm{H_2O}/f\mathrm{HF})^{fluid} \sim 4.5$ log units). This value is coherent with a OH/F ratio as

observed in typical pegmatitic-hydrothermal type fluids (instead Baoshan topaz started to form at higher temperature ~1203-1225 K from a water poor /fluorine rich fluid $((fH_2O/fHF)^{fluid} \sim 1.2$ log units). Coherently with the F/OH topaz ratios, the topaz-forming fluids of Padre Paraìso is richer of water with respect to Baoshan. The remarkable high of Li, B and B and low Ge contents confirms the pegmatite origin of the Padre Paraìso blue topaz, in agreement with the pegmatite type composition as reported for Padre Paraìso topaz deposits.

In turn, the presence of Fe and Ti, the high contents of Ge (decoupled with Ga) and the related depletion of Zn, W and Sn point towards the greisen deposit origin for the Baoshan topaz and allows us to reduce the number of possible source deposits presents in the Tengchong-Baoshan Sn-polymetallic metallogenic belt from eight (counting only the main deposits) to four, the greisen type deposits, namely: Baihuanao, Xiaolonghe, Dasongpo and Lailishan.

References

- Achtschin, A. B. (1999). Caracterização geológica, mineralógica e geoquímica dos pegmatitos do Distrito de Padre Paraíso, Minas Gerais, e suas variedades de berilo (Doctoral dissertation, MSc thesis, Instituto de Geociências, Universidade Federal de Minas Gerais).
- Afshooni, S. Z., Mirnejad, H., Esmaeily, D., Haroni, H. A. (2013) Mineral chemistry of hydrothermal biotite from the Kahang porphyry copper deposit (NE Isfahan), Central Province of Iran. *Ore Geology Reviews*, **54**, 214-232.
- Agangi, A. et al. (2014) Crystallisation of magmatic topaz and implications for Nb–Ta–W mineralisation in F-rich silicic melts — The Ary-Bulak ongonite massif. *Lithos* **202-203**, 317-330.
- Agangi, A. et al. (2016) Relation between cathodoluminescence and trace-element distribution of magmatic topaz from the Ary-Bulak massif, Russia. *Mineralogical Magazine,* **80 (5)**, 881-899.
- Akizuki, M., Hampar, M. S., Zussman, J. (1979) An explanation of anomalous optical properties of topaz. *Mineralogical Magazine,* **43 (326)**, 237-241.
- Alberico, A., Ferrando, S., Ivaldi, G., Ferraris G. (2003) X-ray single-crystal structure refinement of an OH-rich topaz from Sulu UHP terrane (Eastern China)—structural foundation of the correlation between cell parameters and fluorine content. *European Journal of Mineralogy,* **15**, 875-881.
- Almeida, A. C. S., Bello, R. M. S., & Gandini, A. L. (2007). Topázio imperial das minas do Vermelhão e JJC, Ouro Preto, MG: Estudos de inclusões fluidas e considerações genéticas. *Geochimica Brasiliensis*, *21*(2).
- Alston, N. A., & West, J. (1928). The structure of topaz [Al (F, OH)] 2 SiO4. *Proceedings of the Royal Society of London. Series A, Containing Papers of a Mathematical and Physical Character*, *121*(787), 358-367.

- Altomare, A. et al. (2009) EXPO2009: structure solution by powder data in direct and reciprocal space. *Journal of Applied Crystallography,* **42**, 1197-1202.
- Andersson, S. S. et al. (2018) Origin of the high-temperature Olserum-Djupedal REE-phosphate mineralisation, SE Sweden: A unique contact metamorphic-hydrothermal system. *Ore Geology Reviews,* **101**, 740-764.
- Ayuso, R. A., Wooden, J. L., Foley, N. K., Seal, R. R., & Sinha, A. K. (2005). U-Pb zircon ages and Pb isotope geochemistry of gold deposits in the Carolina slate belt of South Carolina. *Economic Geology*, *100*(2), 225-252.
- Bakker, R. J., Elburg, M. A. (2006) A magmatic-hydrothermal transition in Arkaroola (northern Flinders Ranges, South Australia): from diopside–titanite pegmatites to hematite–quartz growth. *Contributions to Mineralogy and Petrology,* **152(5)**, 541-569.
- Bao, B. et al. (2016) Compositions of biotite, amphibole, apatite and silicate melt inclusions from the Tongchang mine, Dexing porphyry deposit, SE China: Implications for the behaviour of halogens in mineralized porphyry systems. *Ore Geology Reviews,* **79**, 443-462.
- Barton, M. D. (1982) The thermodynamic properties of topaz solid solutions and some petrologic applications. *American Mineralogist,* **67 (9-10)**, 956-974.
- Barton, M. D., Haselton, H. T., Hemingway, B. S., Kleppa, O. J., Robie, R. A. (1982) The thermodynamic properties of fluor-topaz. *American Mineralogist,* **67 (3-4)**, 350-355.
- Bradbury, S. E., Williams, Q. (2003) Contrasting bonding behaviour of two hydroxyl-bearing metamorphic minerals under pressure: Clinozoisite and topaz. *American Mineralogist,* **88 (10)**, 1460-1470.
- Breiter, K., & Kronz, A. (2004). Phosphorus-rich topaz from fractionated granites (Podlesí, Czech Republic). *Mineralogy and Petrology*, 81(3), 235-247.

- Breiter, K., Ackerman, L., Ďurišová, J., Svojtka, M., & Novák, M. (2014). Trace element composition of quartz from different types of pegmatites: A case study from the Moldanubian Zone of the Bohemian Massif (Czech Republic). *Mineralogical Magazine*, 78(3), 703-722.
- Breiter, K., Ackerman, L., Svojtka, M., & Müller, A. (2013). Behavior of trace elements in quartz from plutons of different geochemical signature: A case study from the Bohemian Massif, Czech Republic. *Lithos*, 175, 54-67.
- Breiter, K., Gardenová, N., Vaculovič, V. (2013) Topaz as an important host for Ge in granites and greisens. *Mineralogical Magazine*, **77(4)**, 403-417.
- Broz, M. E., Cook, R. F., & Whitney, D. L. (2006). Microhardness, toughness, and modulus of Mohs scale minerals. *American Mineralogist*, **91(1)**, 135-142.
- Burt, D. M., Sheridan, M. F., Bikun, J. V., Christiansen, E. H. (1982) Topaz rhyolites; distribution, origin, and significance for exploration. *Economic Geology,* **77 (8)**, 1818-1836.
- Černý, P. (1991). Rare-element granitic pegmatites. Part I: Anatomy and internal evolution of pegmatite deposits. *Geoscience Canada*, 18(2), 49-67.
- Černý, P., & Ercit, T. S. (2005). The classification of granitic pegmatites revisited. *The Canadian Mineralogist*, 43(6).
- Cervelli F., Carrato S., Mattei A., Benevoli L., Vaccari L. (2012) Beyond Fingerprints Morphology: Chemical Mapping of Functional Groups, proceedings of the 20th European Signal Processing Conference, EUSIPCO 2012, pp. 1509–1513.
- Cesare, B., Marchesi, C., Hermann, J., Gómez-Pugnaire, M. T. (2003) Primary melt inclusions in andalusite from anatectic graphitic metapelites: Implications for the position of the Al2SiO5 triple point. *Geology* **31 (7)**, 573-576.

- Chen, J., Lager, G. A., Kunz, M., Hansen, T. C., Ulmer, P. (2005) A Rietveld refinement using neutron powder diffraction data of a fully deuterated topaz, $Al_2SiO_4(OD)_2$. *Acta Crystallographica E,* **61 (11)**, i253-i255.
- Christiansen, E. H., Sheridan, M. F., & Burt, D. M. (1986). The geology and geochemistry of Cenozoic topaz rhyolites from the western United States.
- Coulson, I. M., Gregory, M. D., Raudsepp, M. (2001) Evolution of HF and HCl activity in magmatic volatiles of the gold-mineralized Emerald Lake pluton, Yukon Territory, Canada. *Mineralium Deposita,* **36**, 594-606.
- Darke, S. A., & Tyson, J. F. (1994). Review of solid sample introduction for plasma spectrometry and a comparison of results for laser ablation, electrothermal vaporization, and slurry nebulization. *Microchemical journal*, *50*(3), 310-336.
- Day, R. A., Vance, E. R., Cassidy, D. J., Hartman, J. S. (1995) The topaz to mullite transformation on heating. *Journal of materials research*, 10 (11), 2963-2969.
- De Campos, C. D., Mendes, J. C., Ludka, I. P., Medeiros, S. R., Moura, J. C., & Wallfass, C. (2004). A review of the Brasiliano magmatism in southern Espírito Santo, Brazil, with emphasis on postcollisional magmatism. *Journal of the Virtual Explorer*, *17*(1), 35.
- Deng, J., Wang, Q., Li, G., Li, C., & Wang, C. (2014). Tethys tectonic evolution and its bearing on the distribution of important mineral deposits in the Sanjiang region, SW China. *Gondwana Research*, *26*(2), 419-437.
- Dewonck, S., Leroy, J.L., Dusausoy Y. (1998) Colour in topaz from rhyolite domes of the San Luis Potosi volcanic field, Mexico. *Journal of Gemmology,* **26**, 29-39.
- Dolejš, D., & Baker, D. R. (2004). Thermodynamic analysis of the system Na 2 OK 2 O-CaO-Al 2 O 3-SiO 2-H 2 OF 2 O− 1: stability of fluorine-bearing minerals in felsic igneous suites. *Contributions to Mineralogy and Petrology*, *146*(6), 762-778.

- Dolejš, D., Baker, D. R. (2004) Thermodynamic analysis of the system Na_2O-K_2O-CaO-Al_2O_3-SiO_2-H_2OF_2O)1: Stability of fluorine-bearing minerals in felsic igneous suites. *Contributions to Mineralogy and Petrology,* **146**, 762-778.
- Dong, F. L., Hou, Z. Q., Gao, Y. F., Zeng, P. S., Jiang, C. X., & Du, A. D. (2005). Re-Os isotopic dating of molybdenite from Datongchang copper-lead-zinc deposit in Tengchong area, western Yunnan. *MINERAL DEPOSITS-BEIJING-*, *24*(6), 663.
- Duck J.J. (1986) An investigation of factors controlling the partitioning of trace germanium and gallium between topaz and quartz. MSc thesis, University of Pittsburgh, Pennsylvanis, USA, 76 pp.
- Duck J.J. Cohen A.J. (1986) Partition of trace germanium and gallium between intergrown topaz and quartz . Abstracts with program 1986; the Fourteenth general meeting of the International Mineralogical Association, Stanford, California, USA (Prewitt C.T., chairman), p. 93 (abstract)
- Durrant, S. F. (1999). Laser ablation inductively coupled plasma mass spectrometry: achievements, problems, prospects. *Journal of Analytical Atomic Spectrometry*, *14*(9), 1385-1403.
- Eadington, P. J., & Nashar, B. (1978). Evidence for the magmatic origin of quartz-topaz rocks from the New England Batholith, Australia. *Contributions to Mineralogy and Petrology*, *67*(4), 433-438.
- El Korh, A., Luais, B., Deloule, E., & Cividini, D. (2017). Iron isotope fractionation in subduction-related high-pressure metabasites (Ile de Groix, France). *Contributions to Mineralogy and Petrology*, 172(6), 1-19.
- El-Manawy, Islam. (2001) "Floristic composition and zonation of seaweeds on Zabargad Reef (Red Sea, Egypt)." *Taeckholmia* 21.1: 115-134

- Ercit, T. S., Linnen, R. L., & Samson, I. M. (2005). REE-enriched granitic pegmatites. *Rare-element geochemistry and mineral deposits: Geological Association of Canada, GAC Short Course Notes*, *17*, 175-199.
- Fei, Y. (1995) Thermal expansion in Mineral Physics and Crystallography: A Handbook of Physical Constants vol. 2 (ed. T. J. Ahrens) 29 – 44 (AGU, Washington, D. C.)
- Ferreira, M. D. S. F., Fonseca, M. A., & Pires, F. R. M. (2005). Pegmatitos mineralizados em água-marinha e topázio do Ponto do Marambaia, Minas Gerais: tipologia e relações com o Granito Caladão.
- Ferreira, M. S. F., Fonseca, M. A., Pires, F. R. M. (2005) Pegmatites mineralized in aqua marine and topaz of ponto do Marambaia, Minas Gerais: tipology and relationships with the Caladão granite. *Revista Brasileira de Geociências* **35 (4)**, 463-473.
- Feser, M., Hornberger, B., Jacobsen, C., De Geronimo, G., Rehak, P., Holl, P., & Strüder, L. (2006). Integrating Silicon detector with segmentation for scanning transmission X-ray microscopy. *Nuclear Instruments and Methods in Physics Research Section A: Accelerators, Spectrometers, Detectors and Associated Equipment*, *565*(2), 841-854.
- Finger, L. W., Cox, D. E., Jephcoat, A. P. (1994) A correction for powder diffraction peak asymmetry due to axial divergence. *Journal of Applied Crystallography,* **27 (6)**, 892-900.
- Frindt, S., & Poutiainen, M. (2002). PT path fluid evolution in the Gross Spitzkoppe granite stock, Namibia. *BULLETIN-GEOLOGICAL SOCIETY OF FINLAND*, *74*(1/2), 103-114.
- Foord, E. E., Chirnside, W., Lichte, F. E., & Briggs, P. H. (1995). Pink topaz from the Thomas Range, Juab County, *Utah. Mineralogical Record*, **26**(1), 57.
- Gandini, A. L, Achtschin, A. B., Marciano, V. R., Bello, R. F. & Pedrosa-Soares, A. C. (2001) Berilo. In: Castan˜ eda, C., Addad, J. E. & Liccardo, A. (eds) Gemas De Minas Gerais, Belo Horizonte, Sociedade Brasileira De Geologia Nu´cleo Minas Gerais, 100–127.

- Gatta, G. D., Nestola, F., Bromiley, G. D., Loose, A. (2006) New insight into crystal chemistry of topaz: A multi-methodological study. *American Mineralogist,* **91 (11-12)**, 1839–1846.
- Gauzzi, T., Graça, L. M., Lagoeiro, L., de Castro Mendes, I., Queiroga, G. N. (2018). The fingerprint of imperial topaz from Ouro Preto region (Minas Gerais state, Brazil) based on cathodoluminescence properties and composition. *Mineralogical Magazine,* **82 (4)**, 943-960.
- Gianoncelli, A., Bonanni, V., Gariani, G., Guzzi, F., Pascolo, L., Borghes, R., ... & Kourousias, G. (2021). Soft X-ray Microscopy Techniques for Medical and Biological Imaging at TwinMic—Elettra. *Applied Sciences*, *11*(16), 7216.
- Gianoncelli, A., Kaulich, B., Alberti, R., Klatka, T., Longoni, A., De Marco, A., ... & Kiskinova, M. (2009). Simultaneous soft X-ray transmission and emission microscopy. *Nuclear Instruments and Methods in Physics Research Section A: Accelerators, Spectrometers, Detectors and Associated Equipment*, *608*(1), 195-198.
- Gioncada, A., et al. (2014). Topaz magmatic crystallization in rhyolites of the Central Andes (Chivinar volcanic complex, NW Argentina): constraints from texture, mineralogy and rock chemistry. *Lithos*, *184*, 62-73.
- Gonzalez-Platas, J., Alvaro, M., Nestola, F., Angel, R. (2016) EosFit7-GUI: a new graphical user interface for equation of state calculations, analyses and teaching. *Journal of Applied Crystallography,* **49(4)**, 1377-1382.
- Gu, L. X., Gou, X. Q., Zhang, Z. Z., Wu, C. Z., Liao, J. J., Yang, H., ... & Min, M. Z. (2003). Geochemistry and petrogenesis of a multi-zoned high Rb and F granite in eastern Tianshan. *Acta Petrologica Sinica*, *19*(4), 585-600.

- Gu, L. X., Zhang, Z. Z., Wu, C. Z., Gou, X. Q., Liao, J. J., & Yang, H. (2011). A topaz-and amazonite-bearing leucogranite pluton in eastern Xinjiang, NW China and its zoning. *Journal of Asian Earth Sciences*, *42*(5), 885-902.
- Hansen, T. C. et al. (2008) The D20 instrument at the ILL: a versatile high-intensity two-axis neutron diffractometer. *Measurement Science and Technology,* **19 (3)**, 034001.
- Harlaux, M., Mercadier, J., Bonzi, W. M. E., Kremer, V., Marignac, C., & Cuney, M. (2017). Geochemical signature of magmatic-hydrothermal fluids exsolved from the Beauvoir rare-metal granite (Massif Central, France): Insights from LA-ICPMS analysis of primary fluid inclusions. *Geofluids*, *2017*.
- Hou, Z., Zaw, K., Pan, G., Mo, X., Xu, Q., Hu, Y., & Li, X. (2007). Sanjiang Tethyan metallogenesis in SW China: tectonic setting, metallogenic epochs and deposit types. *Ore Geology Reviews*, *31*(1-4), 48-87.
- Jin, X. (2013). *Neutron Diffraction: Principles, Instrumentation and Applications*. Novinka.
- Johnston, C., & Chappell, B. W. (1992). Topaz-bearing rocks from Mount Gibson, North Queensland, Australia. *American Mineralogist*, 77(3-4), 303-313.
- Kahwage, M. A., & Mendes, J. C. (2003). O berilo gemológico da provincia pegmatitica Oriental do Brasil. *Geochimica Brasiliensis*, 17(1).
- Kaznatcheev, K. V., Karunakaran, C., Lanke, U. D., Urquhart, S. G., Obst, M., & Hitchcock, A. P. (2007). Soft X-ray spectromicroscopy beamline at the CLS: commissioning results. *Nuclear Instruments and Methods in Physics Research Section A: Accelerators, Spectrometers, Detectors and Associated Equipment*, *582*(1), 96-99.
- Komatsu, K. et al. (2008) Pressure dependence of the hydrogen-bond geometry in topaz-OD from neutron powder diffraction. *American Mineralogist,* **93 (1)**, 217-227.
- Komatsu, K. et al. (2005) Pressure dependence of the OH-stretching mode in F-rich natural topaz and topaz-OH. *American Mineralogist,* **90 (1)**, 266-270.

- Komatsu, K., Kuribayashi, T., Kudoh, Y. (2003) Effect of temperature and pressure on the crystal structure of topaz, $Al_2SiO_4(OH, F)_2$. *Journal of Mineralogical and Petrological Sciences,* **98,** 167–180.
- Kortemeier, W. T., & Burt, D. M. (1988). Ongonite and topazite dikes in the Flying W ranch area, Tonto basin, Arizona. *American Mineralogist*, *73*(5-6), 507-523.

  Huang, F. F., Wang, R. C., Xie, L., Zhu, J. C., Erdmann, S., Che, X. D., & Zhang, R. Q. (2015). Differentiated rare-element mineralization in an ongonite–topazite composite dike at the Xianghualing tin district, Southern China: An electron-microprobe study on the evolution from niobium–tantalum-oxides to cassiterite. *Ore Geology Reviews*, *65*, 761-778.
- Košler, J. (2007). Laser ablation ICP—MS—a new dating tool in Earth science. *Proceedings of the Geologists' Association*, *118*(1), 19-24.
- Kovalenko, V. I., & Yarmolyuk, V. V. (2004). Ore deposits and metallogeny of Mongolia. In Tectonics, Magmatism and Metallogeny of Mongolia (pp. 242-261). Routledge.
- Launay, G., Sizaret, S., Lach, P., Melleton, J., Gloaguen, E., & Poujol, M. (2021). Genetic relationship between greisenization and Sn-W mineralizations in vein and greisen deposits: Insights from the Panasqueira deposit (Portugal). *BSGF-Earth Sciences Bulletin*, **192**(1), 2.
- Li, F., Zhu, J., Rao, B., Jin, Z., & Zhang, L. (2004). Origin of Li-F-rich granite: Evidence from high PT experiments. *Science in China Series D: Earth Sciences*, **47**(7), 639-650.
- Li, L., Chen, Y. J., & Qin, J. H. (2009). The Xinqi rare metal multimetallic deposit of syenogranite weathering crust, Tengchong. *Yunnan Geology*, **28**, 72-77.
- Li, F., Zhu, J., Rao, B., Jin, Z., & Zhang, L. (2004). Origin of Li-F-rich granite: Evidence from high PT experiments. Science in China Series D: Earth Sciences, **47**(7), 639-650.
- London, D. (2008). Pegmatites. *Canadian Mineralogist*, **10**, 347.
- London, D., & Kontak, D. J. (2012). Granitic pegmatites: scientific wonders and economic bonanzas. *Elements*, **8**(4), 257-261.

- London, D., Hunt, L. E., & Duval, C. L. (2020) Temperatures and duration of crystallization within gem-bearing cavities of granitic pegmatites. *Lithos*, 360, 105417.
- Lukkari, S., Holtz, F. (2006) Phase relations of a F-enriched peraluminous granite: an experimental study of the Kymi topaz granite stock, southern Finland. *Contributions to Mineralogy and Petrology*, 153, 273-288.
- Lutz, H. D. (2003) Structure and strength of hydrogen bonds in inorganic solids. *Journal of Molecular Structure*, **646** (1-3), 227-236.
- Markl, G., & Schumacher, J. C. (1997). Beryl stability in local hydrothermal and chemical environments in a mineralized granite. *American Mineralogist*, **82**(1-2), 194-202.
- Markl, G., Piazolo, S. (1998) Halogen-bearing minerals in syenites and high-grade marbles of Dronning Maud Land, Antarctica: monitors of fluid compositional changes during late-magmatic fluid–rock interaction processes. *Contributions to Mineralogy and Petrology,* **132**, 246-268.
- Marshall, L. J., Oliver, N. H. S. (2008) Constraints on hydrothermal fluid pathways within Mary Kathleen Group stratigraphy of the Cloncurry iron-oxide–copper–gold District, Australia. *Precambrian Research*, **163** (1-2), 151-158.
- Martin, R. F., & De Vito, C. (2005). The patterns of enrichment in felsic pegmatites ultimately depend on tectonic setting. *Canadian Mineralogist*, **43**(6), 2027.
- Martins, M. L., Gates, W. P., Michot, L., Ferrage, E., Marry, V., & Bordallo, H. N. (2014) Neutron scattering, a powerful tool to study clay minerals. *Applied clay science*, **96**, 22-35.
- Martucci a., Hansen T.C. (2019) Exploring the role of OH/F substitution in topaz: relationships between structural features and chemical environments. Institut Laue-Langevin (ILL)

- Mendes, J.C., Medeiros, S.R., McReath, I., De Campos, C. (2005) Cambro–Ordovician magmatism in SE Brazil: U-Pb and Rb–Sr ages, combined with Sr–Nd isotopic data of charnockitic rocks from the Várzea Alegre Complex. *Gondwana Research*, **8**, 1-9.
- Menzies, M. A. (1995). The mineralogy, geology and occurrence of topaz. *Mineralogical Record*, **26**(1), 5.
- Miller, W., Smith, C. W., Mackenzie, D. S., & Evans, K. E. (2009). Negative thermal expansion: a review. *Journal of materials science*, **44**(20), 5441-5451.
- Monteiro, L. V. S. et al. (2008) Mineral chemistry of ore and hydrothermal alteration at the Sossego iron oxide–copper–gold deposit, Carajás Mineral Province, Brazil. *Ore Geology Reviews*, **34** (3), 317-336.
- Monteiro, R. R., & Sabioni, A. C. S. (2014). Preparation of Mullite Whiskers from Powder of Topaz Pure and Doped with Rare Earths. In Materials Science Forum (Vol. 798, pp. 189-194). Trans Tech Publications Ltd.
- Miao, X. (1999). Porous mullite ceramics from natural topaz. *Materials Letters*, **38**(3), 167-172.
- Rudnick, R. L., Gao, S., Holland, H. D., & Turekian, K. K. (2003) Composition of the continental crust. *The crust*, **3**, 1-64.
- Mookherjee, M., Tsuchiya, J., Hariharan, A. Crystal structure, equation of state, and elasticity of hydrous aluminosilicate phase, topaz-OH ($Al_2SiO_4(OH)_2$) at high pressures. *Physics of the Earth and Planetary Interiors,* **251**, 24-35 (2016).
- Morrison, G. R., Gianoncelli, A., Kaulich, B., Bacescu, D., & Kovac, J. (2006). A fast read-out CCD system for configured-detector imaging in STXM. In Conf. Proc. Series IPAP (Vol. 7, pp. 277-379).
- Müller-Lorch, D., Marks, M. A., & Markl, G. (2007). Na and K distribution in agpaitic pegmatites. *Lithos*, **95**(3-4), 315-330.

- Munoz, J. L. (1992) Calculation of HF and HCl fugacities from biotite compositions: Revised equations. Geol. Soc. Am. Bull., Abstr. Prog. 24, A221.
- Munoz, J. L., Swenson A. (1981) Chloride-hydroxyl exchange in biotite and estimation of relative HC1/HF activities in hydrothermal fluids. *Economic Geology,* **76**, 2212-2221.
- Newbury, D. E., Ritchie, N. W. (2015) Performing elemental microanalysis with high accuracy and high precision by scanning electron microscopy/silicon drift detector energy-dispersive X-ray spectrometry (SEM/SDD-EDS). *Journal of Material Science*, **50**(2), 493-518.
- Northrup, P. A., & Reeder, R. J. (1994). Evidence for the importance of growth-surface structure to trace element incorporation in topaz. *American Mineralogist*, **79**(11-12), 1167-1175.
- Northrup, P. A., Leinenweber, K., Parise, J. B. (1994) The location of H in the high-pressure synthetic Al2SiO4(OH)2 topaz analogue. *American Mineralogist*, **79**(3-4), 401-404.
- Parise, J. B., Cuff, C., Moore, F. H. (1980) A neutron diffraction study of topaz: evidence for a lower symmetry. *Mineralogical Magazine*, **43** (331), 943-944.
- Pauling, L. (1928). The crystal structure of topaz. *Proceedings of the National Academy of Sciences of the United States of America,* **14**(8), 603.
- Pedrosa-Soares, A. C., & Wiedemann-Leonardos, C. M. (2000). Evolution of the Araçuaí Belt and its connection to the Ribeira Belt, Eastern Brazil. *Tectonic Evolution of South America*, **31**, 265-310.
- Pedrosa-Soares, A.C. et al. (2006) Magmatismo e tectônica do orógeno Araçuaí no extremo leste de Minas e Norte do Espírito Santo (18°-19°S, 41°-40°30'W). *Geonomos* **14 (1-2)**, 97-111.
- Pedrosa-Soares, A. C., Alkmim, F. F., Tack, L., Noce, C. M., Babinski, M., Silva, L. C. D., & Martins-Neto, M. A. (2008) Similarities and differences between the Brazilian and

African counterparts of the Neoproterozoic Araçuaí-West Congo orogen. *Geological Society, London, Special Publications*, **294**(1), 153-172.

- Pedrosa-Soares, A. C., Babinski, M., Noce, C., Martins, M., Queiroga, G., & Vilela, F. (2011) The Neoproterozoic Macaúbas Group, Araçuaí orogen, SE Brazil. *Geological Society, London, Memoirs*, **36**(1), 523-534.
- Peterson, V. K., Auckett, J. E., Pang, W. K. (2017) Real-time powder diffraction studies of energy materials under non-equilibrium conditions. *IUCrJ,* **4 (5)**, 540-554.
- Pinheiro, M. V. B., Fantini, C., Krambrock, K., Persiano, A. I. C., Dantas, M. S. S., & Pimenta, M. A. (2002) OH/F substitution in topaz studied by Raman spectroscopy. *Physical Review B*, **65**(10), 104301.
- Plaisier, J. R. et al. The X-ray diffraction beamline MCX at Elettra: a case study of non-destructive analysis on stained glass. *Acta Imeko,* **6 (3)**, 71 (2017).
- Precisvalle, N., Martucci, A., Gigli, L., Plaisier, J. R., Hansen, T. C., Nobre, A. G., & Bonadiman, C. (2021). F/OH ratio in a rare fluorine-poor blue topaz from Padre Paraíso (Minas Gerais, Brazil) to unravel topaz's ambient of formation. *Scientific reports*, **11**(1), 1-14.
- Preinfalk, C., Morteani, G., Huber, G. (2000) Geochemistry of the granites and pegmatites of the Aracuai pegmatite district, Minas Gerais (Brazil). *Chemie Der Erde-Geochemistry,* **60 (4)**, 305-326.
- Rebuffi, L. et al. (2014) MCX: a Synchrotron Radiation Beamline for X-ray Diffraction Line Profile Analysis. *Zeitschrift für anorganische und allgemeine Chemie*, **640 (15)**, 3100-3106.
- Ribbe, P. H., & Gibbs, G. V. (1971). The crystal structure of topaz and its relation to physical properties. *American Mineralogist: Journal of Earth and Planetary Materials*, **56(1-2)**, 24-30.

- Ribbe, P. H., & Rosenberg, P. E. (1971). Optical and X-ray determinative methods for fluorine in topaz. *American Mineralogist: Journal of Earth and Planetary Materials,* **56(9-10)**, 1812-1821.
- Rinne, F. (1926) XIII. Comment on optical anomalies within a topaz from Brazil. *Z. Krist. Cryst. Mater.* **63(1–6)**, 236–246.
- Rojas, A. J., Bello, R. M. D. S., Endo, I., & Gandini, A. L. (2009). Estudio mineralógico, microtermométrico y aspectos estructurales de la mineralización de topacio imperial de Antônio Pereira, Distrito de Ouro Preto (Minas Gerais)-Brasil. *Rem: Revista Escola de Minas*, **62**, 9-16.
- Rosenberg, P. E. (1972). Compositional variations in synthetic topaz. *American Mineralogist: Journal of Earth and Planetary Materials*, **57**(1-2), 169-187.
- Schott, S., Rager, H., SCHÜRMANN, K., & Taran, M. (2003). Spectroscopic study of natural gem quality "Imperial"-Topazes from Ouro Preto, Brazil. *European Journal of Mineralogy*, **15**(4), 701-706.
- Selby, D., Nesbitt, B. E., Muehlenbachs, K., Prochaska, W. (2000) Hydrothermal Alteration and Fluid Chemistry of the Endako Porphyry Molybdenum Deposit, British Columbia. *Economic Geology,* **95***(1), 183-202*
- Shannon, R. D. (1976) Revised effective ionic radii and systematic studies of interatomic distances in halides and chalcogenides. *Acta Crystallographica A,* **32**, 751-767.
- Simons, B., Andersen, J. C., Shail, R. K., & Jenner, F. E. (2017). Fractionation of Li, Be, Ga, Nb, Ta, In, Sn, Sb, W and Bi in the peraluminous early permian Variscan granites of the Cornubian Batholith: Precursor processes to magmatic-hydrothermal mineralisation. *Lithos*, **278**, 491-512.

- Smirnov, S. Z. (2015) The fluid regime of crystallization of water-saturated granitic and pegmatitic magmas: a physicochemical analysis. *Russian Geology and geophysics*, **56**(9), 1292-1307
- Soufi, M., Remmal, T., El Hassani, I. E. E. A., & Makhoukhi, S. (2018) Topaz solid solution in the F-rich granitic rocks from Blond (NW Massif Central, France). *Arabian Journal of Geosciences*, **11**(14), 1-22.
- Soufi, M. (2021). Origin and physical-chemical control of topaz crystallization in felsic igneous rocks: Contrasted effect of temperature on its OH–F substitution. *Earth-Science Reviews*, **213**, 103467.
- Staron, P., Fischer, T., Lippmann, T., Stark, A., Daneshpour, S., Schnubel, D., Schreyer, A. (2011) In situ experiments with synchrotron high-energy X-rays and neutrons. *Advanced Engineering Materials*, **13**(8), 658-663.
- Sun, S.-s. & McDonough, W. F. (1989) Chemical and isotopic systematics of oceanic basalts: implications for mantle composition and processes. In: Saunders, A. D. & Norry, M. J. (eds) Magmatism in the Ocean Basins. *Geological Society, London, Special Publications,* **42**, 313-345
- Sutherland, F. L., Zaw, K., Meffre, S., Yui, T. F., & Thu, K. (2015) Advances in trace element "fingerprinting" of gem corundum, ruby and sapphire, Mogok area, Myanmar. *Minerals*, **5**(1), 61-79.
- Sykes, M. L., & Moody, J. B. (1978) Pyrophyllite and metamorphism in the Carolina slate belt. *American Mineralogist*, **63**(1-2), 96-108.
- Tao, Y., Zhu, F. L., Ma, Y. S., Ye, L., & Chen, Z. T. (2009) LA-ICP-MS zircon U-Pb dating of Zhibenshan granite from Baoshan block. *Acta Mineralogica Sinica*, **29**, 329.

- Taylor, R. P. (1992) Petrological and geochemical characteristics of the Pleasant Ridge zinnwaldite-topaz granite, southern New Brunswick, and comparisons with other topaz-bearing felsic rocks. *Canadian Mineralogist*, **30**(3), 895-921.
- Tennakoon, S. et al. (2018) Single crystal elasticity of natural topaz at high temperatures. *Scientific Reports,* **8** (1), 1-9.
- Thomas, R. (1982). Ergebnisse der thermobarogeochemischen Untersuchungen an Flüssigkeitseinschlüssen in Mineralen der postmagmatischen Zinn-Wolfram-Mineralisation des Erzgebirges.
- Thomas, R., Davidson, P. (2010) Hambergite-rich melt inclusions in morganite crystals from the Muiane pegmatite, Mozambique and some remarks on the paragenesis of hambergite. *Mineralogy and Petrology*, **100(3-4)**, 227-239.
- Thomas, R., Davidson, P., Appel, K. (2019) The enhanced element enrichment in the supercritical states of granite–pegmatite systems. *Acta Geochimica,* **38(3)**, 335-349.
- Thomas, R., & Davidson, P. (2013). The missing link between granites and granitic pegmatites. *Journal of Geosciences*, **58**(2), 183-200.
- Thompson, J. F. H. (1995) (Ed.). Magmas, fluids, and ore deposits. Mineralogical Association of Canada (Short course) **Vol. 23**.
- Tillberg, M., Maskenskaya, O. M., Drake, H., Hogmalm, J. K., Broman, C., Fallick, A. E., & Åström, M. E. (2019). Fractionation of rare earth elements in greisen and hydrothermal veins related to A-type magmatism. *Geofluids*, 2019.
- Tilley R.J.D. (2013) Color Centres. In: Luo R. (eds) Encyclopedia of Color Science and Technology. Springer, New York, NY.
- Toby, B. H. (2001) EXPGUI, a graphical user interface for GSAS. *Journal of Applied Crystallography*, **34**(2), 210-213.

- Ul-Hamid, A. (2018). A beginners' guide to scanning electron microscopy (Vol. 1, p. 402). Cham: Springer International Publishing.
- Turley, C. H., & Nash, W. P. (1980). Petrology of late Tertiary and Quaternary volcanism in western Juab and Millard Counties, Utah. *Utah Geological Mineral Survey Study*, **52**, 1-33.
- Ulian, G., Valdrè, G. (2017) Effects of fluorine content on the elastic behaviour of topaz [Al2SiO4(F,OH)2]. *American Mineralogist*, **102** (2), 347-356.
- Van Laar, B., Yelon, W. B. (1984) The peak in neutron powder diffraction. *Journal of Applied Crystallography*, **17**(2), 47-54.
- Veksler, I. V., Thomas, R., & Schmidt, C. (2002) Experimental evidence of three coexisting immiscible fluids in synthetic granitic pegmatite. *American Mineralogist*, **87**(5-6), 775-779.
- Viana, R. R., Jordt-Evangelista, H., Stern, W. B. (2007) Geochemistry of muscovite from pegmatites of the Eastern Brazilian pegmatite province: a clue to petrogenesis and mineralization potential. *European Journal of Mineralogy*, **19** (5), 745-755.
- Vladykin, N. V. (2013) Petrology and composition of rare-metal alkaline rocks in the South Gobi Desert, Mongolia. *Russian Geology and Geophysics*, **54**(4), 416-435.
- Von Dreele, R. B., Larson, A. C. (2004) General structure analysis system (GSAS). Los Alamos, New Mexico: Los Alamos National Laboratory 748, 86-748.
- Wang, Y., Xing, X., Cawood, P. A., Lai, S., Xia, X., Fan, W., ... & Zhang, F. (2013). Petrogenesis of early Paleozoic peraluminous granite in the Sibumasu Block of SW Yunnan and diachronous accretionary orogenesis along the northern margin of Gondwana. *Lithos*, **182**, 67-85.
- Watenphul, A., & Wunder, B. (2010) Temperature dependence of the OH-stretching frequencies in topaz-OH. *Physics and Chemistry of Minerals*, **37**(2), 65-72.

- Wen, B. Y., Chen, Q. Q., Radjenovic, P. M., Dong, J. C., Tian, Z. Q., & Li, J. F. (2021) In Situ Surface-Enhanced Raman Spectroscopy Characterization of Electrocatalysis with Different Nanostructures. *Annual Review of Physical Chemistry*, **72**, 331-351.
- Wise, M. A. (1995) Topaz: A mineralogical review. Rocks & Minerals, 70(1), 16-25.
- Wunder, B., Rubie, D. C., Ross, C. R., Medenbach, O., Seifert, F., & Schreyer, W. (1993). Synthesis, stability, and properties of Al2SiO4 (OH) 2: a fully hydrated analogue of topaz. *American Mineralogist*, **78**(3-4), 285-297.
- Wunder, B., Andrut, M., & Wirth, R. (1999) High-pressure synthesis and properties of OH-rich topaz. *European Journal of Mineralogy*, **11**(5), 803-813.
- Xie, L., Wang, R., Chen, J., Zhu, J., Zhang, W., Lu, J., & Zhang, R. (2013) A tin-mineralized topaz rhyolite dike with coeval topaz granite enclaves at Qiguling in the Qitianling tin district, southern China. *Lithos*, **170**, 252-268.
- Xiong, X. (1996) A preliminary experimental investigation on genesis of topaz greisen. *Chinese Science Bulletin*, **41**(17), 1451-1454.
- Xiong, X. L., Rao, B., Chen, F. R., Zhu, J. C., & Zhao, Z. H. (2002) Crystallization and melting experiments of a fluorine-rich leucogranite from the Xianghualing Pluton, South China, at 150 MPa and H2O-saturated conditions. *Journal of Asian Earth Sciences*, **21**(2), 175-188.
- Yang, Q. J., Xu, Y. G., Huang, X. L., & Luo, Z. Y. (2006) Geochronology and geochemistry of granites in the Gaoligong tectonic belt, western Yunnan: Tectonic implications. *Acta Petrologica Sinica*, **22**(4), 817-834.
- Yang, X. M., Lentz, D. R., Chi, G., & Thorne, K. G. (2008) Geochemical characteristics of gold-related granitoids in southwestern New Brunswick, Canada. *Lithos*, **104**(1-4), 355-377.

- Yang, Q., Yigang, X., Xiaolong, H., Zhenyu, L., & Yuruo, S. (2009) Geochronology and geochemistry of granites in the Tengliang area, western Yunnan: Tectonic implication. *Acta Petrologica Sinica*, **25**(5), 1092-1104.
- Yokoi, O. Y., Viglio, E. P., Waghorn, J. G., Jones, J. P., & Figueroa, L. A. (1987) Potosi, a primary tin deposit in Rondônia. *Revista Brasileira de Geociências*, **17**(4), 557-561.
- Zagorsky, V. Y., Makagon, V. M., & Shmakin, B. M. (1999) The systematics of granitic pegmatites. *Canadian Mineralogist*, **37**(3), 800-802.
- Zemann, J., Zobetz, E., Heger, G., Vollenke, H. (1979) Strukturbestimmung eines OH-reichen Topases. Osterreichische Akad. Wiss., Mathem.-Naturwiss. Klasse **116**, 145-147.
- Zhang, R.Y., Liou, J.G., Shu J.F. (2002) Hydroxyl-rich topaz in high-pressure and ultrahigh-pressure kyanite quartzites, with retrograde woodhouseite, from the Sulu terrane, eastern China. *American Mineralogist*, **87**, 445-453.
- Zhang, W., Lentz, D. R., Thorne, K. G., McFarlane, C. (2016) Geochemical characteristics of biotite from felsic intrusive rocks around the Sisson Brook W–Mo–Cu deposit, west-central New Brunswick: An indicator of halogen and oxygen fugacity of magmatic systems. *Ore Geology Reviews*, **77**, 82-96.
- Zhang, Z. M. et al. (2011) Fluid–rock interactions during UHP metamorphism: a review of the Dabie–Sulu orogen, east-central China. *Journal of Asian Earth Sciences*, **42** (3), 316-329.
- Zhengjun, W., Lei, X. , Rucheng, W., Jinchu, Z., Xudong, C., & Xu, Z. (2018). The Petrogenesis and Mineralization of the Laiziling Greisen, Xianghualing District, Hunan Province, South China. *Geological Journal of China Universities*, **24**(4), 467.
- Zhu, C., Sverjensky, D. A. (1992) Partitioning of F-Cl-OH between minerals and hydrothermal fluids. *Geochimica et Cosmochimica Acta,* **55 (7)**, 1837-1858.

APPENDIX A 1: Trace elements from LA-ICP-MS (expressed in ppm), Padre Paraíso

	PAD3_1	σ_error	PAD3_2	σ_error
Li	1.559	0.074	2.208	0.097
Be	<0.00	<0.00	<0.048	0.015
B	<0.67	0.33	3.6	0.32
Mg	6.95	0.3	7.54	0.31
Ca	187.56	7.318	78.45	7.318
Sc	4.04	0.18	3.42	0.16
Ti	59.35	2.49	50.05	2.13
V	0.0678	0.007	0.0875	0.0076
Cr	0.89	0.13	0.46	0.096
Mn	<0.056	0.033	<0.052	0.023
Fe	72.77	4.77	53.83	3.63
Co	0.0032	0.0011	0.00171	0.00075
Ni	<0.0053	0.003	0.0358	0.0054
Cu	0.0177	0.0063	0.0639	0.0078
Zn	0.218	0.044	<0.053	0.023
Ga	8.42	0.74	8.16	0.74
Ge	47.1	4.6	48.38	4.87
As	<0.079	0.04	<0.078	0.033
Rb	<0.0063	0.0033	0.0219	0.0034
Sr	0.0184	0.0019	0.00435	0.00067
Y	<0.00057	0.0002	0.00298	0.0004
Zr	0.0152	0.0018	0.0218	0.0021
Nb	18.06	1.61	13.83	1.27
Mo	0.0238	0.0039	<0.0062	0.0026
Cd	<0.057	0.029	<0.056	0.036
In	0.00123	0.00052	<0.00063	0.00027
Sn	0.381	0.048	0.114	0.018
Sb	0.018	0.0045	0.025	0.0053
Cs	0.0205	0.0031	<0.0040	0.0017
Ba	0.00462	0.00071	0.0348	0.0036
La	0.00567	0.00076	0.00118	0.00023
Ce	0.00383	0.0006	0.0048	0.00064
Pr	0.00313	0.0005	<0.00057	0.00021
Nd	<0.00	<0.00	<0.00	<0.00
Sm	0.013	0.0025	<0.00	<0.00
Eu	<0.00	<0.00	<0.00	<0.00
Gd	<0.00	<0.00	<0.00	<0.00
Tb	<0.00	<0.00	<0.00	<0.00
Dy	<0.00	<0.00	<0.00	<0.00
Ho	<0.00	<0.00	<0.00	<0.00
Er	<0.00	<0.00	<0.00	<0.00
Tm	<0.00067	0.00039	<0.00	<0.00
Yb	<0.00	<0.00	<0.00	<0.00
Lu	<0.00	<0.00	<0.00	<0.00
Hf	0.0246	0.0035	0.0257	0.0033
Ta	5.65	0.56	3.9	0.4
W	0.475	0.061	0.411	0.054
Au	<0.0054	0.0025	0.0054	0.0012
Pb	0.081	0.013	0.024	0.005
Bi	<0.0022	0.0011	0.00203	0.00092
Th	0.00349	0.00068	<0.00	<0.00
U	<0.00130	0.00046	<0.00	<0.00

	PAD3_3	σ_error	PAD3_4	σ_error	PAD3_5	σ_error
Li	2.204	0.096	0.932	0.048	1.126	0.055
Be	<0.00	<0.00	<0.00	<0.00	0.152	0.02
B	1.63	0.24	1.01	0.27	2.86	0.29
Mg	6.55	0.28	6.2	0.27	4.88	0.22
Ca	43.09	7.318	171.65	7.318	36.37	7.318
Sc	3.48	0.16	3.75	0.18	3.71	0.18
Ti	47.12	2.04	52.1	2.29	55.17	2.46
V	0.0526	0.0052	0.0643	0.0064	0.0299	0.0043
Cr	0.755	0.096	0.377	0.086	0.335	0.084
Mn	0.166	0.022	<0.044	0.021	<0.047	0.025
Fe	55.54	3.81	63.36	4.45	66.09	4.74
Co	0.00295	0.00044	<0.00187	0.00084	0.0068	0.001
Ni	0.0114	0.0037	<0.0065	0.0027	0.0166	0.0048
Cu	0.0516	0.0065	0.0331	0.0062	0.0225	0.0049
Zn	0.172	0.033	0.44	0.069	0.259	0.044
Ga	8.06	0.75	8.27	0.79	7.79	0.77
Ge	47.85	4.95	44.22	4.7	44.4	4.84
As	<0.050	0.022	0.058	0.027	0.398	0.037
Rb	<0.0047	0.0022	<0.0053	0.0028	<0.0051	0.0022
Sr	0.0345	0.0034	0.0145	0.0015	0.009	0.0011
Y	0.00078	0.00015	<0.00040	0.0002	<0.00050	0.00018
Zr	0.0259	0.0024	0.0204	0.002	0.0238	0.0024
Nb	13.88	1.31	15.98	1.55	16.69	1.66
Mo	0.0201	0.0037	<0.0052	0.0024	<0.0065	0.0028
Cd	0.253	0.044	<0.036	0.017	<0.061	0.031
In	0.00085	0.00018	<0.00088	0.0004	0.00292	0.00058
Sn	0.084	0.014	0.494	0.064	0.78	0.1
Sb	0.0587	0.0086	<0.0096	0.0048	0.0323	0.0058
Cs	<0.0035	0.0016	0.0059	0.0019	<0.0036	0.0016
Ba	0.0183	0.002	0.00677	0.00087	0.00264	0.00043
La	0.00187	0.00029	0.00331	0.00046	0.00107	0.00021
Ce	0.00568	0.00071	<0.00049	0.00025	0.00326	0.00049
Pr	<0.00	<0.00	<0.00040	0.0002	0.00178	0.0003
Nd	<0.00	<0.00	0.0254	0.0034	<0.0035	0.0013
Sm	<0.00	<0.00	<0.00	<0.00	<0.0041	0.0014
Eu	<0.00	<0.00	<0.00	<0.00	<0.00	<0.00
Gd	0.006	0.0012	<0.00	<0.00	<0.00	<0.00
Tb	<0.00	<0.00	<0.00	<0.00	<0.00	<0.00
Dy	<0.00	<0.00	<0.00	<0.00	<0.00	<0.00
Ho	<0.00	<0.00	0.00113	0.00023	<0.00	<0.00
Er	<0.00	<0.00	<0.00	<0.00	<0.00	<0.00
Tm	<0.00063	0.00026	<0.00096	0.00046	<0.00060	0.00022
Yb	<0.00	<0.00	<0.00260	0.00094	<0.00	<0.00
Lu	<0.00	<0.00	<0.00	<0.00	<0.00067	0.00025
Hf	<0.00195	0.0007	0.0192	0.0027	0.0233	0.0032
Ta	3.96	0.42	4.92	0.54	5.35	0.6
W	0.47	0.064	0.478	0.067	0.513	0.073
Au	0.0085	0.0016	0.0201	0.0035	0.0195	0.0034
Pb	0.084	0.014	0.0322	0.0059	0.06	0.01
Bi	0.0095	0.0017	<0.0024	0.0014	<0.00196	0.00084
Th	0.00174	0.00034	<0.00	<0.00	0.002	0.0004
U	0.00179	0.00037	<0.00	<0.00	<0.00	<0.00

	PAD1_1	σ_error	PAD1_2	σ_error	PAD1_3	σ_error	PAD1_4	σ_error
Li	0.75	0.045	0.474	0.038	0.956	0.047	0.461	0.034
Be	<0.00	<0.00	<0.00	<0.00	<0.039	0.012	0.079	0.014
B	4.19	0.36	4.59	0.39	1.56	0.23	<0.78	0.31
Mg	3.12	0.15	2.6	0.13	3.51	0.16	2.64	0.13
Ca	44.38	7.92375	50.94	7.92375	227.92	7.92375	36.11	7.92375
Sc	1.254	0.064	1.147	0.059	1.104	0.058	1.173	0.063
Ti	35.77	1.63	33.96	1.57	36.32	1.7	45.08	2.14
V	0.133	0.012	0.0872	0.0086	0.115	0.011	0.196	0.018
Cr	<0.239	0.099	<0.25	0.11	0.737	0.098	0.75	0.12
Mn	<0.059	0.025	0.098	0.026	0.141	0.021	<0.060	0.024
Fe	62.88	4.63	68.33	5.13	62.42	4.76	66.18	5.17
Co	<0.0027	0.0011	<0.00204	0.0008	<0.00192	0.00083	0.00199	0.00088
Ni	0.0072	0.0032	<0.0140	0.0056	0.0234	0.004	<0.0117	0.0045
Cu	0.091	0.011	0.0383	0.0067	0.0424	0.006	<0.0147	0.0076
Zn	<0.066	0.045	0.233	0.043	<0.044	0.033	<0.067	0.045
Ga	11.77	1.19	11.51	1.19	10.47	1.11	15.52	1.68
Ge	54.35	6.07	54.9	6.28	50.48	5.9	57.46	6.86
As	<0.076	0.032	<0.077	0.031	0.307	0.03	<0.079	0.031
Rb	0.0101	0.0029	<0.0074	0.003	0.012	0.0024	<0.0066	0.0027
Sr	0.0092	0.0011	0.00311	0.00057	0.00564	0.00081	0.00333	0.00081
Y	<0.00072	0.00028	0.00103	0.00021	<0.00063	0.00029	<0.00	<0.00
Zr	0.00228	0.00044	<0.00	<0.00	<0.00	<0.00	<0.00	<0.00
Nb	0.327	0.034	0.298	0.031	0.299	0.032	0.482	0.053
Mo	0.0059	0.0026	0.0131	0.0033	0.0043	0.0017	<0.0054	0.0021
Cd	<0.058	0.024	0.214	0.042	0.095	0.024	0.294	0.057
In	0.00112	0.00024	0.00302	0.00062	<0.00049	0.0002	<0.00112	0.00052
Sn	<0.031	0.017	0.071	0.015	<0.022	0.012	0.072	0.016
Sb	<0.0133	0.0073	<0.0117	0.0048	<0.0090	0.0073	0.0226	0.0053
Cs	<0.0051	0.0025	0.0103	0.0022	0.0045	0.0015	<0.0049	0.002
Ba	0.0106	0.0013	0.00457	0.00068	0.0243	0.0029	0.0107	0.0014
La	0.00123	0.00025	0.00247	0.0004	0.00329	0.00046	0.00218	0.00036
Ce	0.0075	0.001	<0.00	<0.00	0.0025	0.00039	0.00331	0.00052
Pr	<0.00071	0.00028	<0.00	<0.00	0.00136	0.00024	0.00181	0.00032
Nd	0.0071	0.0015	0.0142	0.0024	0.00472	0.00098	<0.00	<0.00
Sm	<0.0083	0.0033	<0.00	<0.00	<0.00	<0.00	<0.00	<0.00
Eu	<0.00	<0.00	<0.00	<0.00	<0.00	<0.00	<0.00	<0.00
Gd	<0.00	<0.00	<0.00	<0.00	<0.00	<0.00	<0.00	<0.00
Tb	<0.00	<0.00	<0.00	<0.00	<0.00	<0.00	<0.00	<0.00
Dy	<0.00	<0.00	<0.00	<0.00	<0.00	<0.00	<0.00	<0.00
Ho	<0.00	<0.00	<0.00	<0.00	<0.00	<0.00	<0.00	<0.00
Er	<0.00	<0.00	<0.00	<0.00	<0.00	<0.00	<0.00	<0.00
Tm	<0.00	<0.00	<0.00090	0.00033	<0.00	<0.00	<0.00	<0.00
Yb	<0.00	<0.00	<0.00	<0.00	<0.00	<0.00	<0.00	<0.00
Lu	<0.00	<0.00	<0.00	<0.00	<0.00	<0.00	<0.00	<0.00
Hf	<0.00	<0.00	<0.00	<0.00	<0.00	<0.00	<0.00	<0.00
Ta	0.0467	0.0056	0.0287	0.0036	0.0426	0.0053	0.111	0.014
W	0.74	0.11	0.75	0.11	0.81	0.13	0.318	0.051
Au	0.0056	0.0013	<0.00	<0.00	<0.00	<0.00	0.0098	0.002
Pb	0.0259	0.0053	<0.0084	0.0034	0.0188	0.0042	0.0096	0.0031
Bi	0.0035	0.0012	<0.0034	0.0017	0.00235	0.0009	<0.00165	0.00073
Th	0.00462	0.00073	<0.00241	0.00095	0.0013	0.00051	<0.00	<0.00
U	<0.00	<0.00	<0.00	<0.00	<0.00	<0.00	0.00212	0.00046

APPENDIX A 2: Trace elements from LA-ICP-MS (expressed in ppm),

Baoshan

	BAO1_1	σ_error	BAO1_2	σ_error
Li	0.78	0.042	0.485	0.032
Be	<0.00	<0.00	<0.00	<0.00
B	<0.74	0.32	2.02	0.3
Mg	3.36	0.14	0.285	0.029
Ca	3.36	1.9	2.305	1.89
Sc	1.693	0.07	0.365	0.018
Ti	17.05	0.67	8.64	0.35
V	0.098	0.0077	0.0221	0.0043
Cr	0.59	0.11	0.55	0.1
Mn	0.16	0.028	<0.056	0.026
Fe	21.31	1.43	2.3	0.7
Co	0.00663	0.00097	0.00599	0.00073
Ni	0.0441	0.0068	0.018	0.0057
Cu	0.251	0.021	0.108	0.011
Zn	0.87	0.1	0.423	0.057
Ga	11.87	0.88	3.98	0.31
Ge	87.4	7.23	197.73	16.96
As	<0.088	0.039	0.086	0.036
Rb	0.0088	0.003	<0.0064	0.0029
Sr	0.0162	0.0015	0.00348	0.00069
Y	0.00363	0.00045	0.1022	0.0079
Zr	0.00262	0.00048	<0.00139	0.00059
Nb	0.0196	0.0017	0.0176	0.0016
Mo	0.0091	0.0036	<0.0083	0.0033
Cd	0.468	0.067	<0.066	0.028
In	<0.00073	0.00026	<0.00097	0.00042
Sn	<0.036	0.02	0.06	0.014
Sb	0.0111	0.0048	<0.0113	0.005
Cs	0.0178	0.0024	0.0104	0.0022
Ba	0.0156	0.0015	0.00619	0.00084
La	0.0158	0.0014	0.00129	0.00025
Ce	0.0246	0.0023	0.0313	0.0029
Pr	0.00237	0.00035	<0.00	<0.00
Nd	0.0329	0.0039	0.0148	0.0022
Sm	<0.0078	0.003	<0.00	<0.00
Eu	<0.00	<0.00	<0.00	<0.00
Gd	<0.00	<0.00	<0.00	<0.00
Tb	<0.00	<0.00	<0.00	<0.00
Dy	<0.00	<0.00	0.0109	0.0022
Ho	<0.00	<0.00	0.00651	0.00073
Er	<0.00	<0.00	0.0082	0.0012
Tm	<0.00079	0.00027	0.00252	0.00037
Yb	<0.00	<0.00	0.0069	0.0013
Lu	0.00155	0.0003	0.0084	0.00094
Hf	0.0062	0.0012	<0.00	<0.00
Ta	0.0044	0.00057	<0.00	<0.00
W	0.567	0.061	0.0323	0.0043
Au	<0.00	<0.00	<0.00	<0.00
Pb	0.102	0.013	0.0383	0.0061
Bi	0.0053	0.0017	0.0044	0.0013
Th	0.0052	0.00074	<0.00	<0.00
U	0.00267	0.00052	<0.00	<0.00

	BAO1_3		BAO1_4		BAO1_5	
Li	<0.049	0.022	0.38	0.024	1.19	0.055
Be	<0.00	<0.00	<0.00	<0.00	<0.00	<0.00
B	1.9	0.28	1.81	0.26	2.21	0.27
Mg	5.38	0.22	0.155	0.021	0.356	0.031
Ca	7.28	1.73	1.965	1.67	2.566	1.53
Sc	1.094	0.048	0.28	0.015	0.1218	0.0098
Ti	13.61	0.55	6.18	0.26	6.35	0.27
V	0.0284	0.0042	0.0223	0.0036	<0.0068	0.0031
Cr	0.428	0.095	0.8	0.1	0.597	0.094
Mn	<0.052	0.023	0.277	0.029	<0.046	0.025
Fe	12.38	0.98	13.33	1.01	14.99	1.11
Co	0.00193	0.0006	0.00584	0.00067	<0.00145	0.00057
Ni	0.0287	0.0043	0.0216	0.0027	<0.0083	0.0034
Cu	<0.0119	0.0052	<0.0106	0.0044	0.0528	0.0065
Zn	<0.061	0.048	0.087	0.02	<0.051	0.028
Ga	9.33	0.74	4.65	0.38	4.71	0.4
Ge	92.76	8.24	163.36	15	157.4	14.92
As	<0.08	<0.00	<0.079	0.033	<0.067	0.032
Rb	<0.0054	0.0024	0.0076	0.0024	<0.0052	0.0024
Sr	0.00468	0.00055	<0.00065	0.0003	0.00853	0.00094
Y	<0.00	<0.00	<0.00058	0.0002	<0.00	<0.00
Zr	<0.00128	0.00042	0.00172	0.00032	0.00807	0.00091
Nb	0.0121	0.0012	0.0264	0.0024	0.0394	0.0036
Mo	<0.0076	0.0031	0.0059	0.0012	0.0138	0.0022
Cd	<0.053	0.024	0.141	0.029	<0.045	0.021
In	0.00113	0.00023	0.00288	0.00054	<0.00084	0.00036
Sn	<0.030	0.013	0.033	0.012	<0.025	0.013
Sb	0.0381	0.0064	0.0263	0.0051	0.0564	0.008
Cs	<0.0041	0.0018	0.0217	0.0026	0.0129	0.0021
Ba	<0.00	<0.00	<0.00	<0.00	0.0121	0.0013
La	0.00124	0.00024	<0.00	<0.00	<0.00	<0.00
Ce	0.0088	0.00097	<0.00	<0.00	0.00667	0.00079
Pr	<0.00	<0.00	<0.00	<0.00	<0.00044	0.00021
Nd	<0.00	<0.00	0.0091	0.0022	<0.00	<0.00
Sm	<0.00	<0.00	<0.00	<0.00	<0.00	<0.00
Eu	<0.00	<0.00	<0.00	<0.00	<0.00	<0.00
Gd	<0.00	<0.00	<0.00	<0.00	<0.00	<0.00
Tb	<0.00	<0.00	<0.00	<0.00	<0.00	<0.00
Dy	<0.00	<0.00	<0.00	<0.00	<0.00	<0.00
Ho	<0.00	<0.00	<0.00	<0.00	<0.00054	0.00019
Er	<0.00	<0.00	<0.00	<0.00	<0.00	<0.00
Tm	<0.00	<0.00	<0.00	<0.00	0.00108	0.00021
Yb	<0.00	<0.00	<0.00	<0.00	0.0059	0.0012
Lu	<0.00	<0.00	<0.00	<0.00	<0.00	<0.00
Hf	<0.00	<0.00	<0.0030	0.001	<0.00	<0.00
Ta	<0.00	<0.00	0.0058	0.00068	0.00683	0.00082
W	0.293	0.034	0.0188	0.0027	0.0331	0.0047
Au	<0.00	<0.00	<0.00	<0.00	<0.00	<0.00
Pb	0.0077	0.003	0.0103	0.003	0.0313	0.0053
Bi	<0.00	<0.00	<0.00221	0.00088	0.00259	0.00083
Th	<0.00	<0.00	<0.00	<0.00	<0.00	<0.00
U	0.00233	0.00046	<0.00	<0.00	<0.00	<0.00

APPENDIX B 1: CORRELOGRAMS FROM LEXRF, Padre Paraíso

XRF Map 25 76x76um 96x96px 3s/px

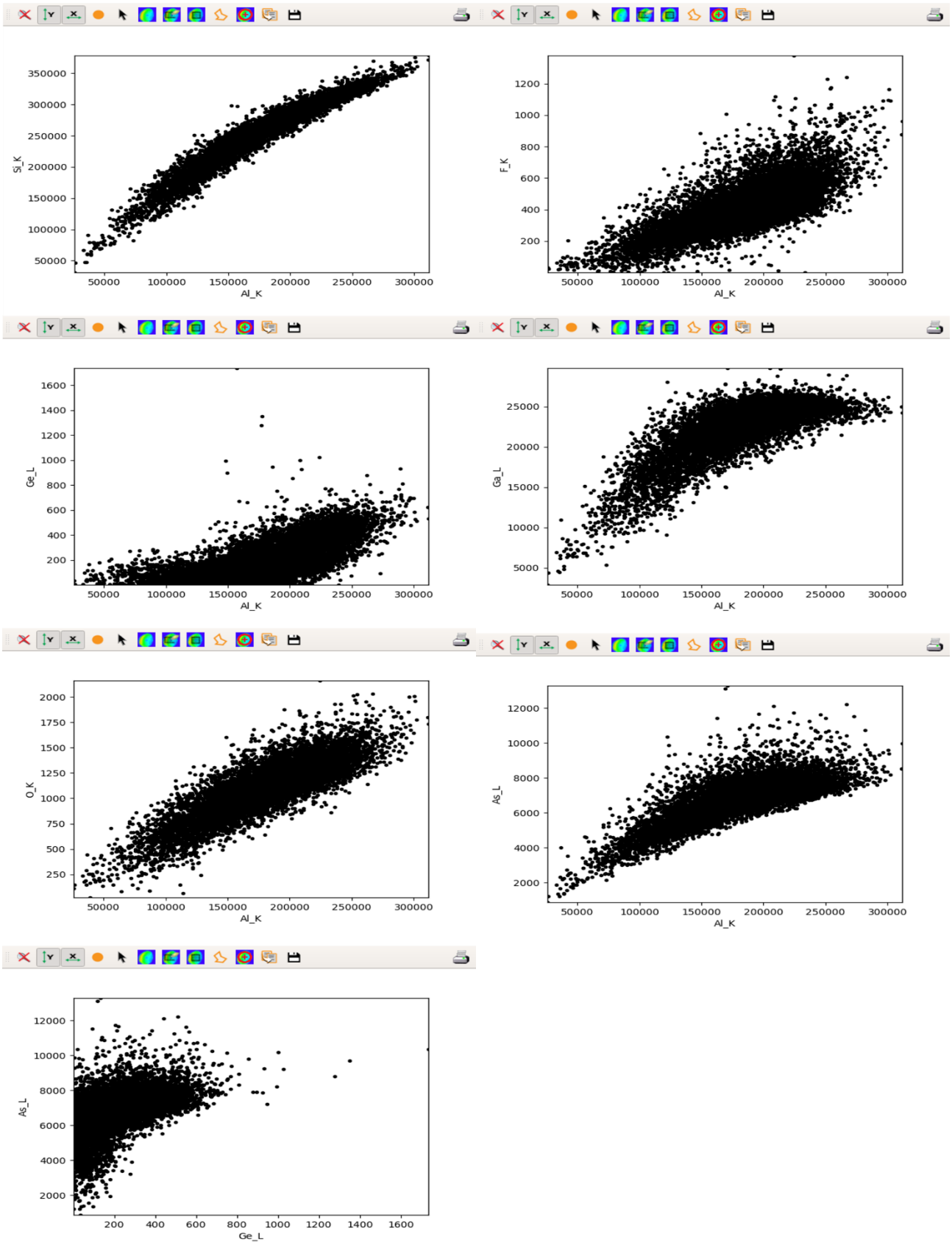

XRF Map 26 76x76um 96x96px 3s/px

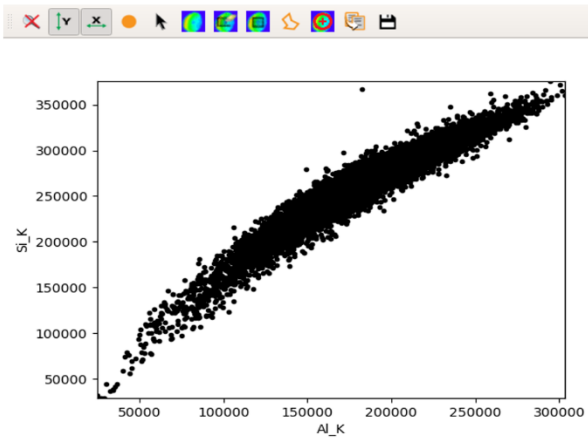

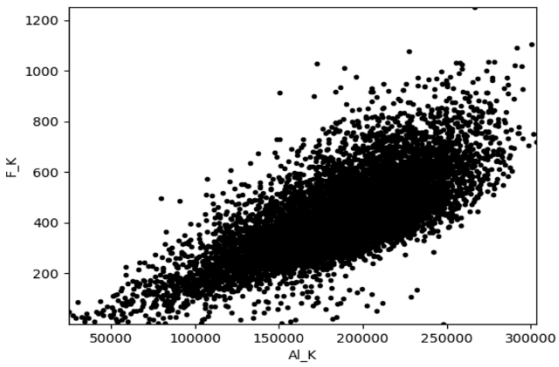

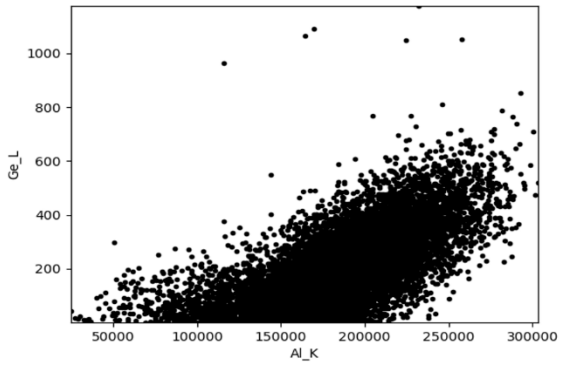

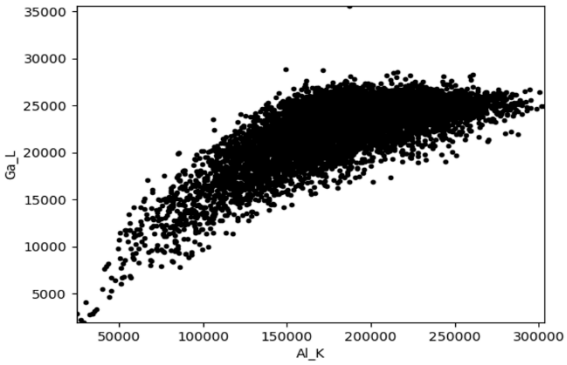

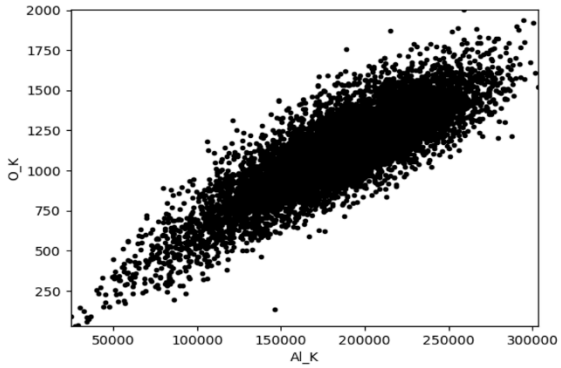

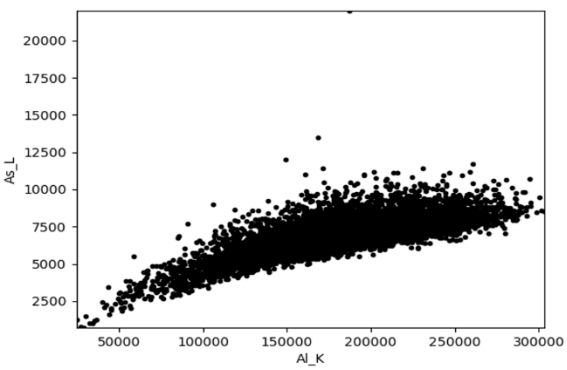

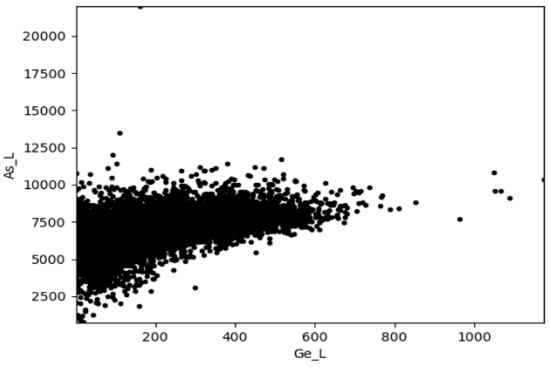

XRF Map 27 68x68um 86x86px 3s/px

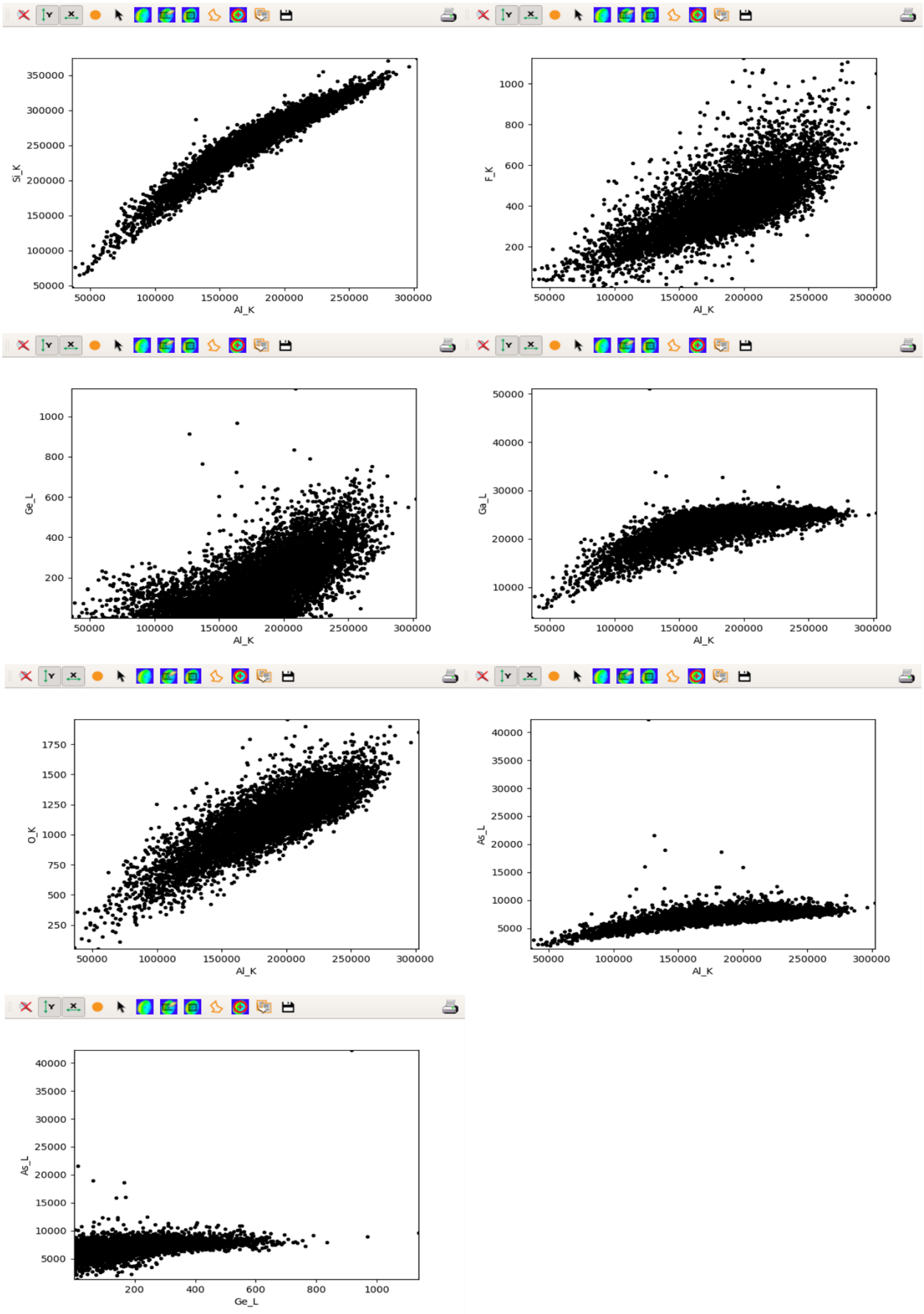

XRF Map 29 76x76um 96x96px 3s/px

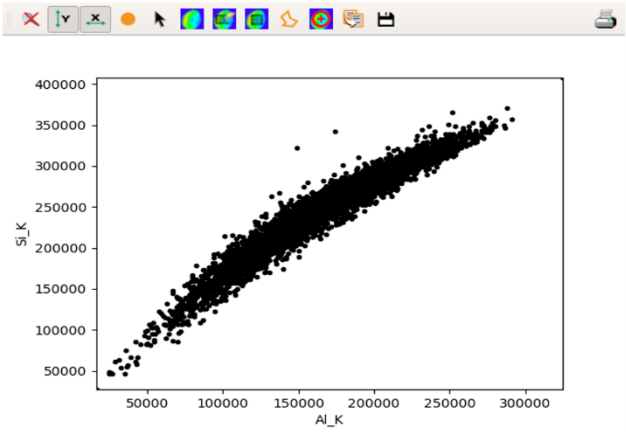

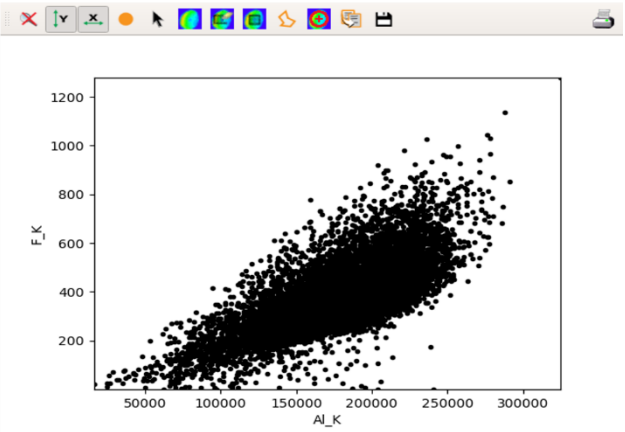

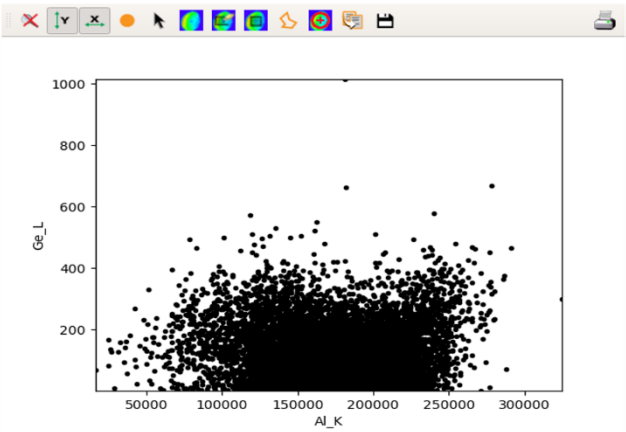

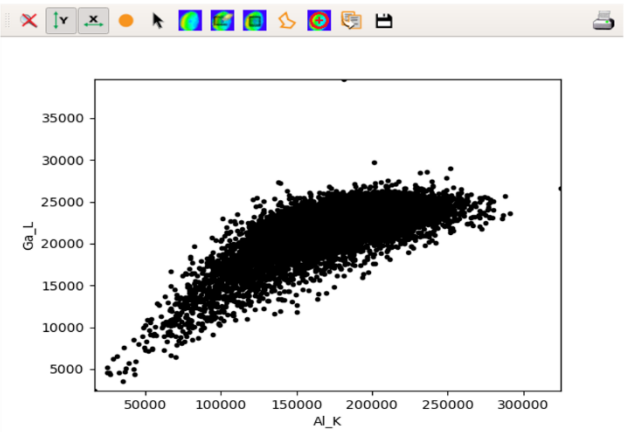

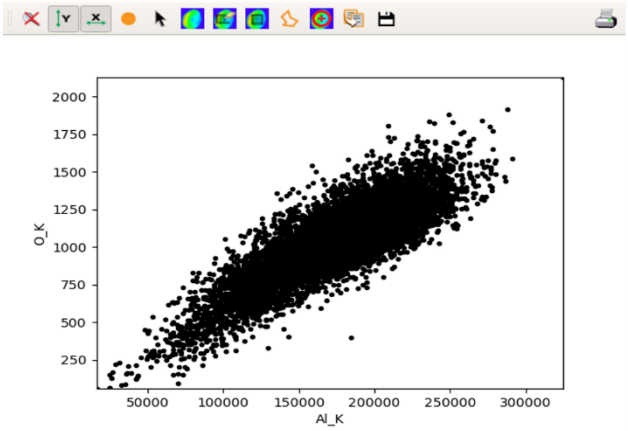

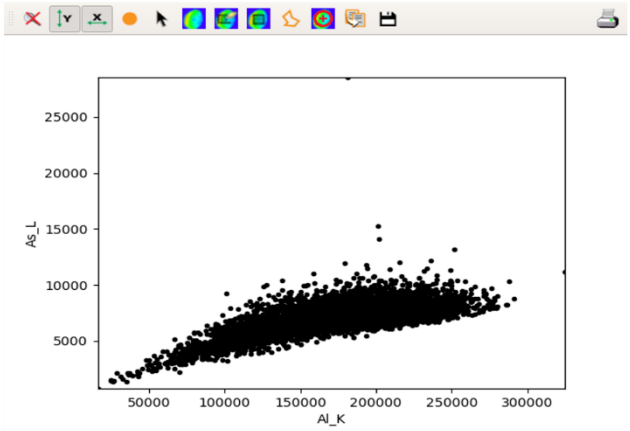

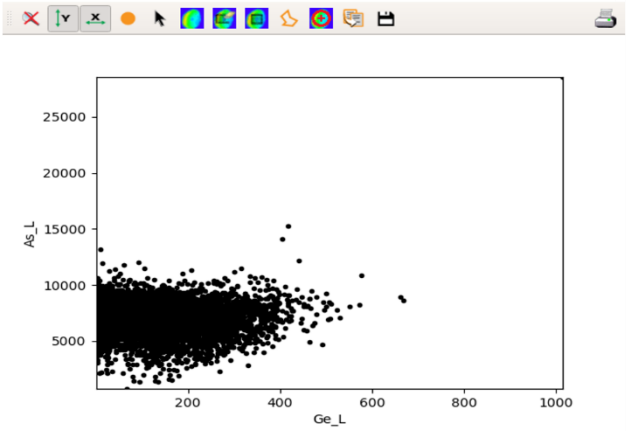

APPENDIX B 2: CORRELOGRAMS FROM LEXRF, Baoshan

XRF Map 14 40x80um 3s/px

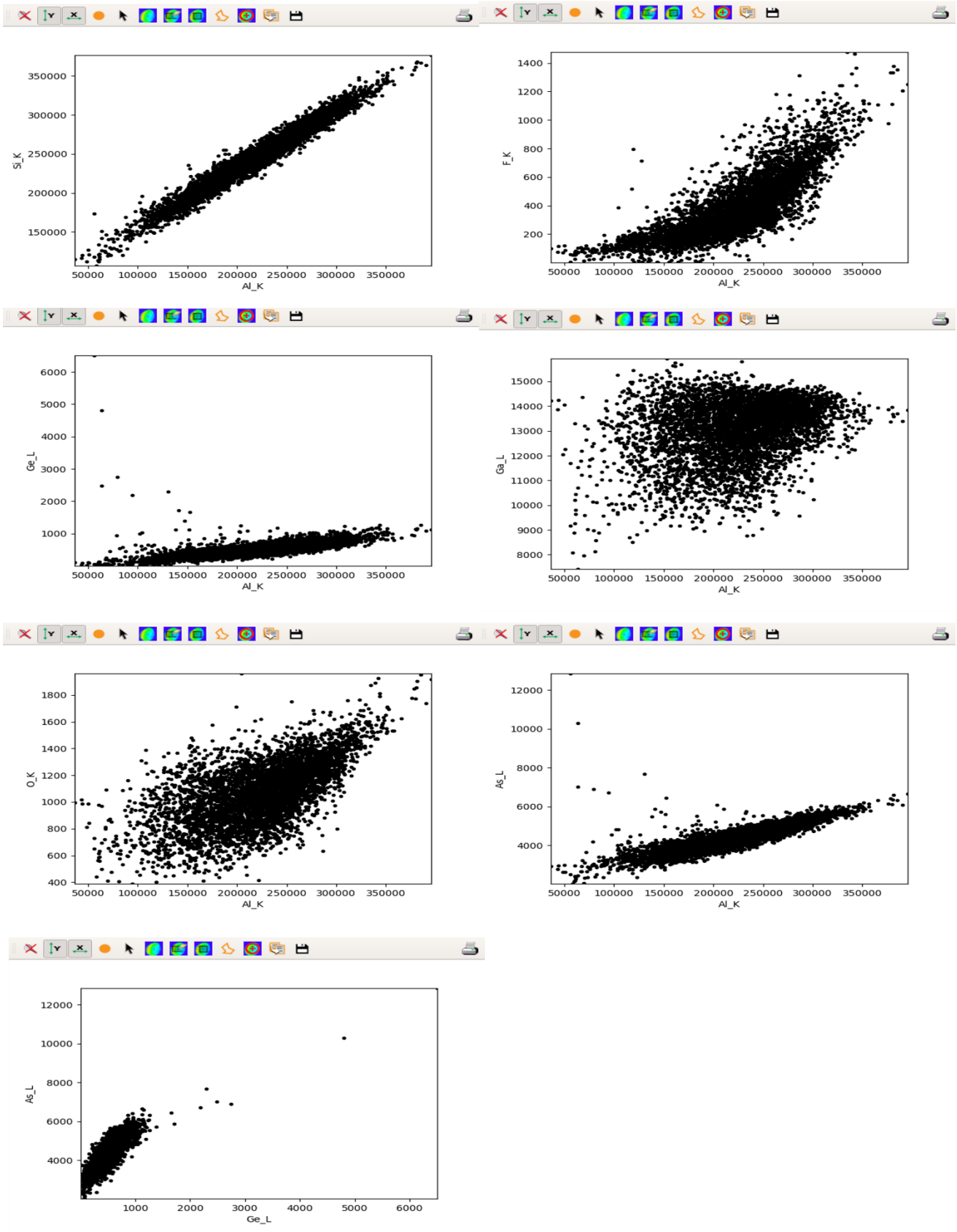

XRF Map 17 80x80um 101x101px 3s/px

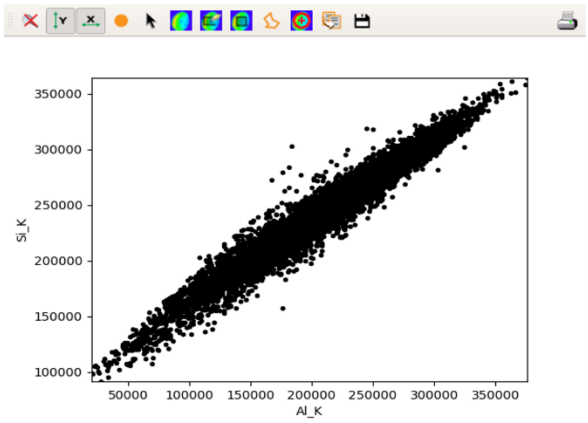

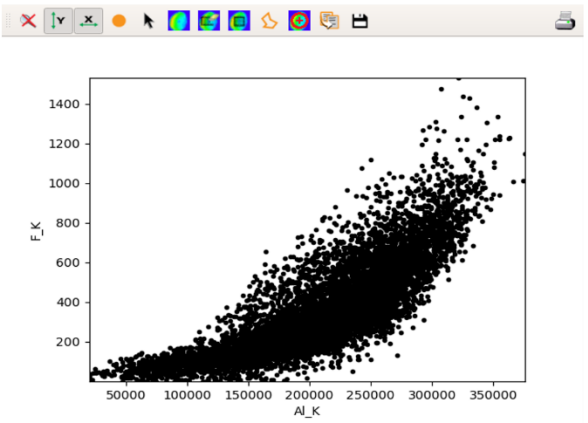

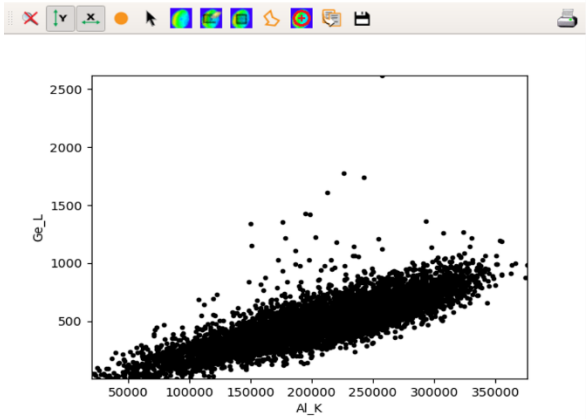

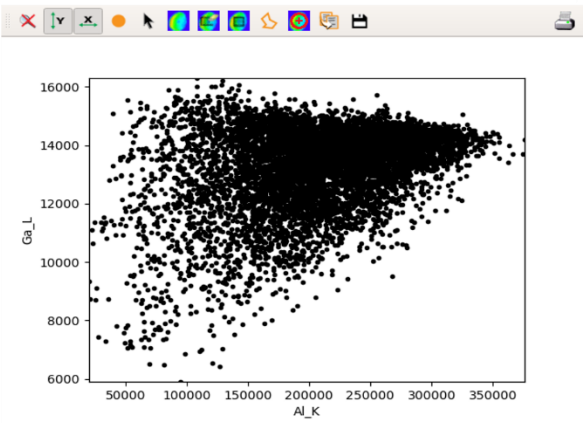

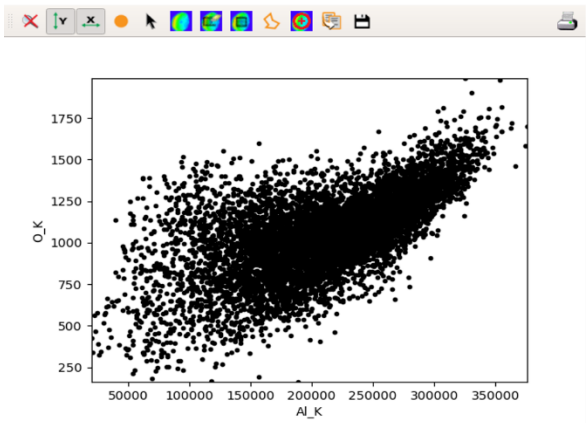

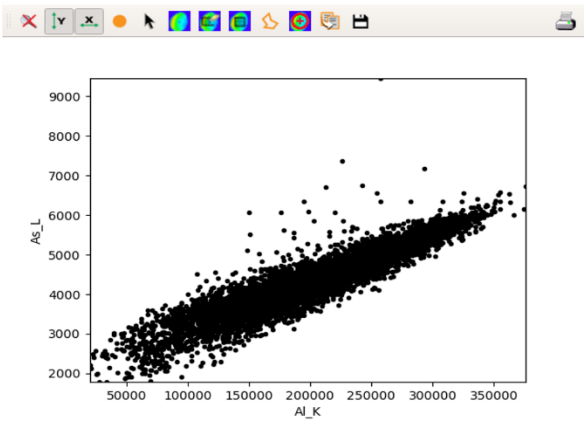

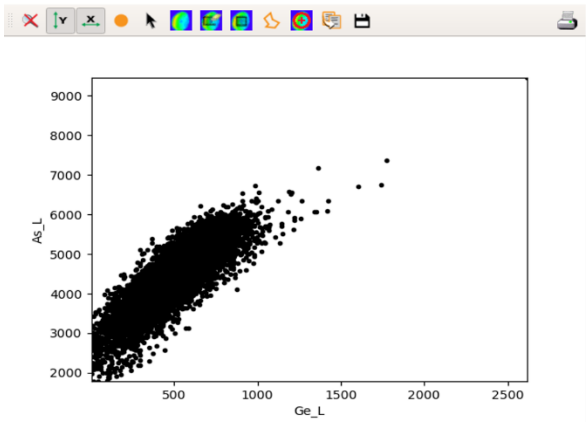

XRF Map 18 76x76um 96x96px 3s/px

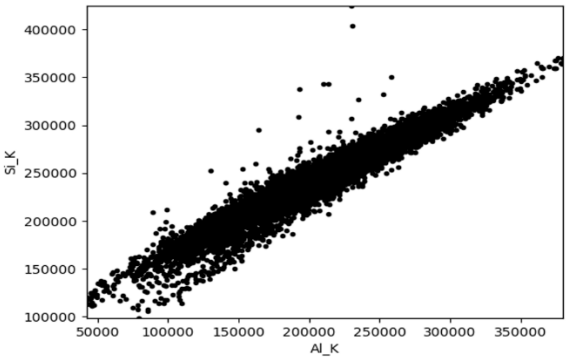

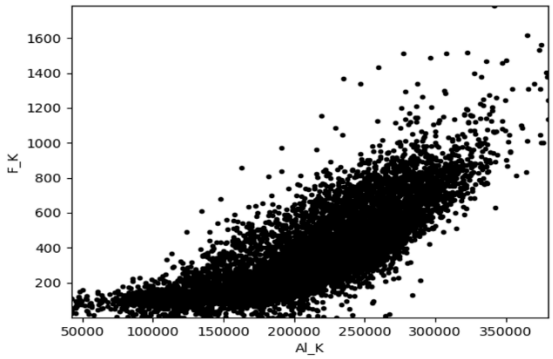

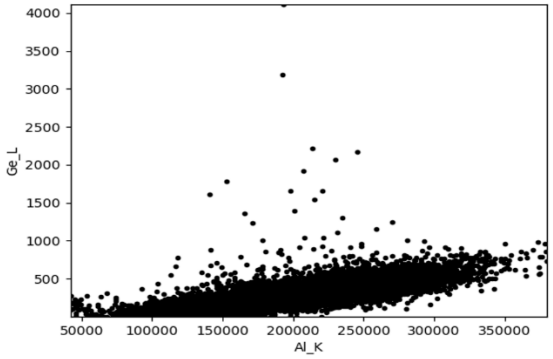

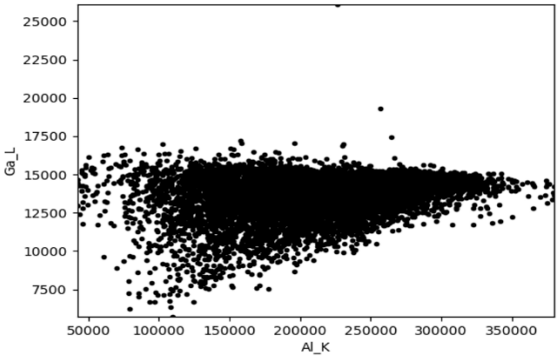

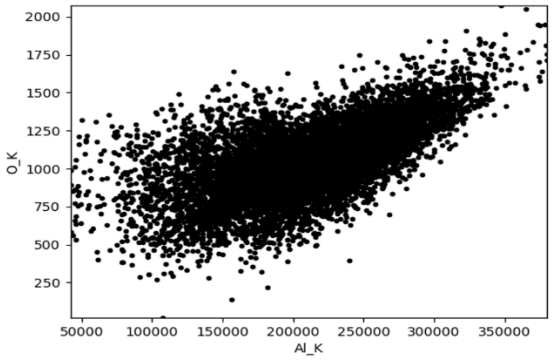

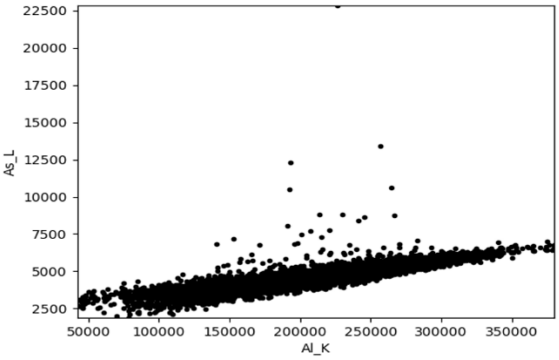

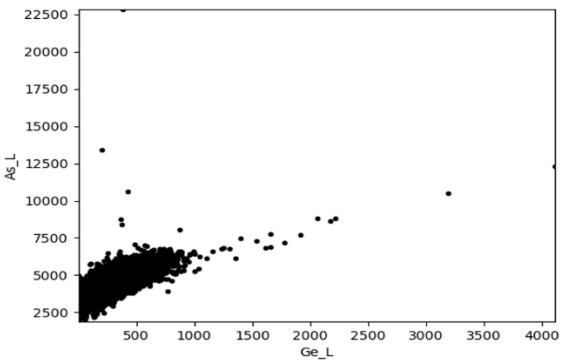

XRF Map 19 76x76um 96x96px 3s/px

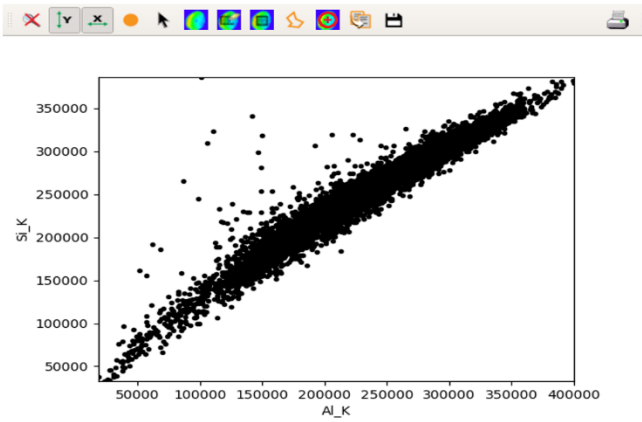

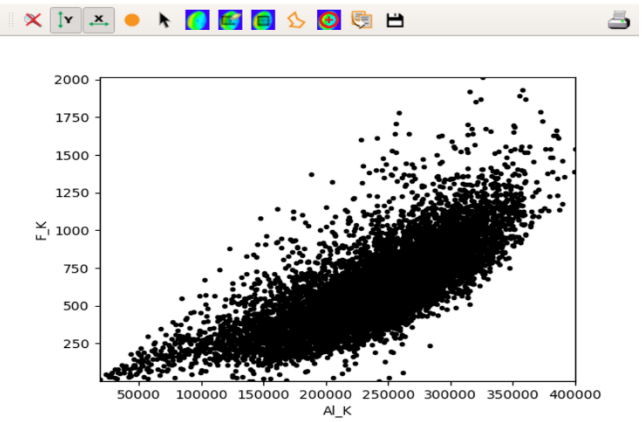

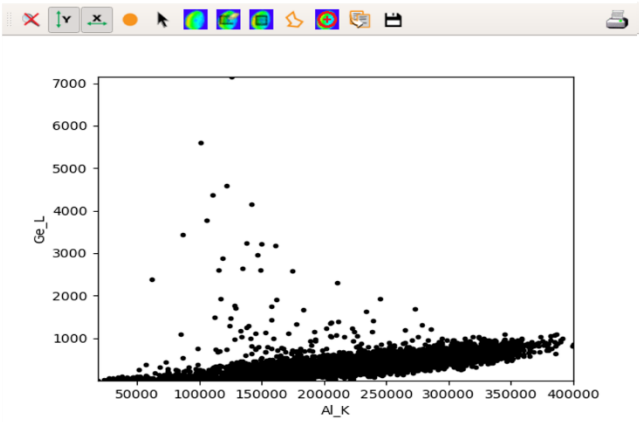

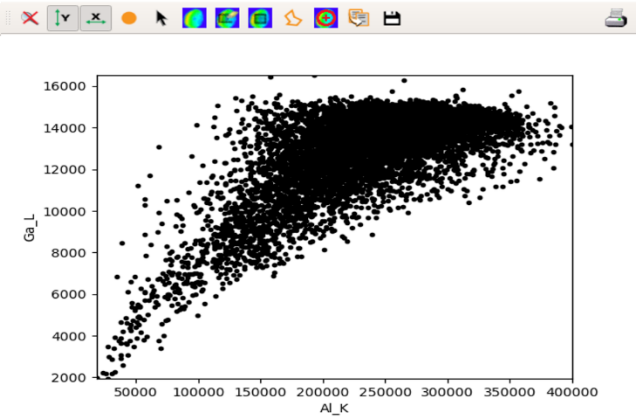

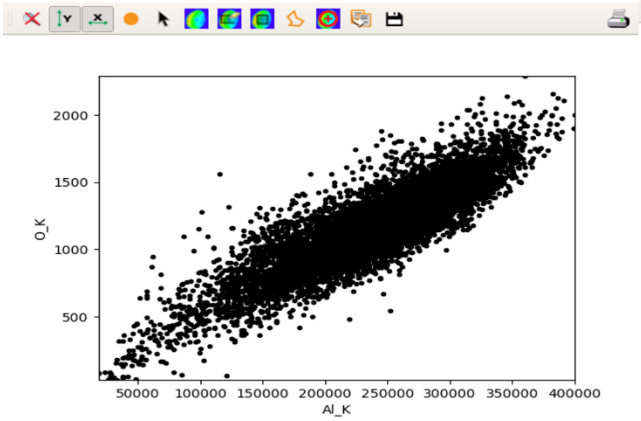

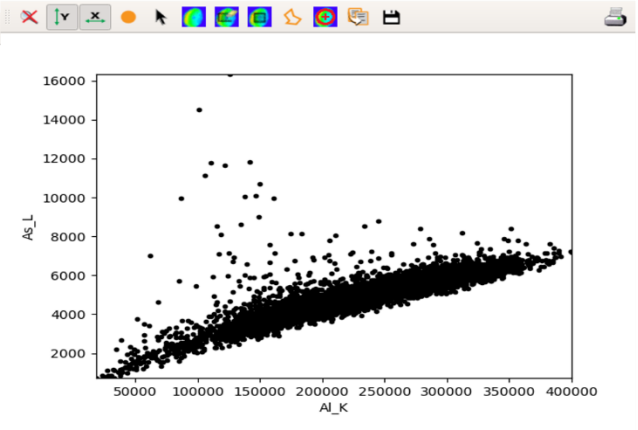

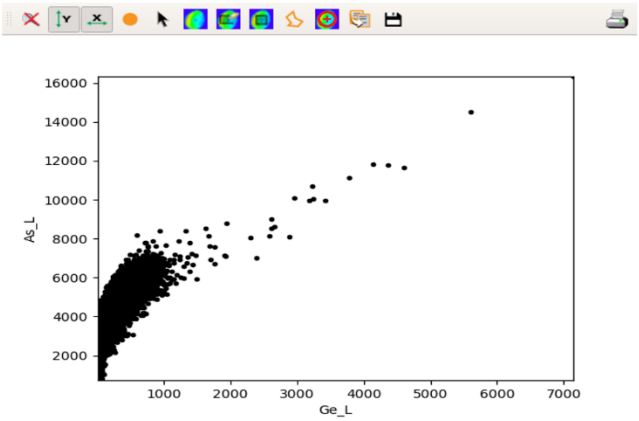

XRF Map 21 72x72um 91x91px 3s/px

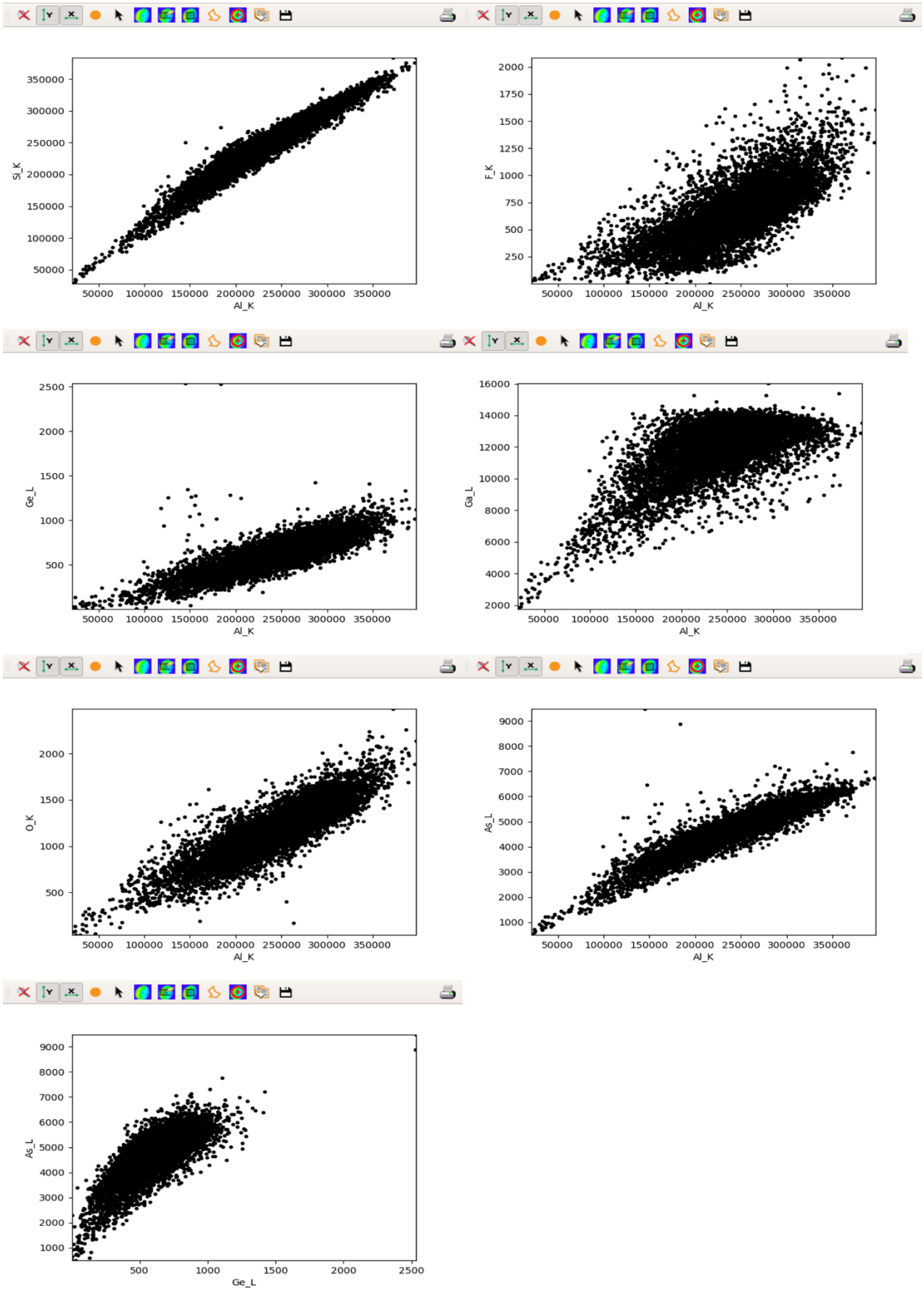

APPENDIX C 1: MAPS OF ELEMENTAL DISTRIBUTION FROM LEXRF, Padre Paraíso

XRF Map 25
76x76um
96x96px
X= 28522
Y= 20507
SS 35um
50ms
XRF 3s
Zosa = -1749
Zzp = -251

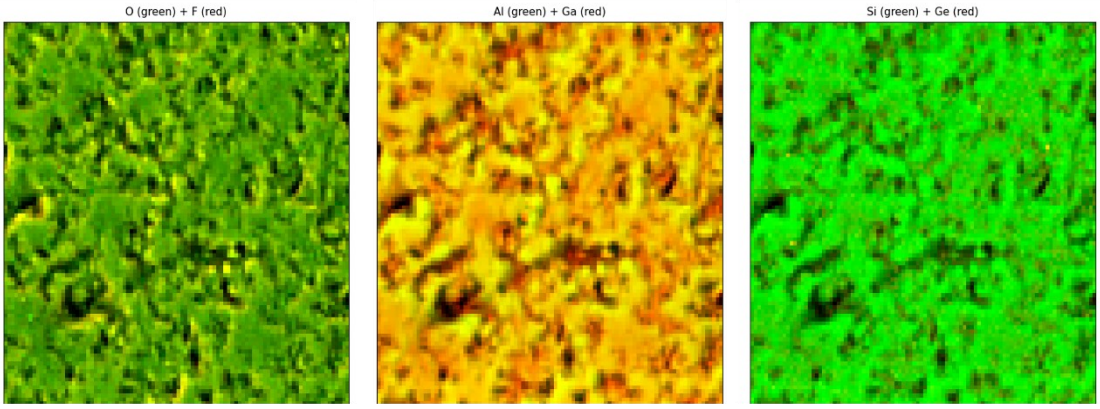

XRF Map 26
76x76um
96x96px
X= 28322
Y= 20507
SS 35um
50ms
XRF 3s
Zosa = -1749
Zzp = -251

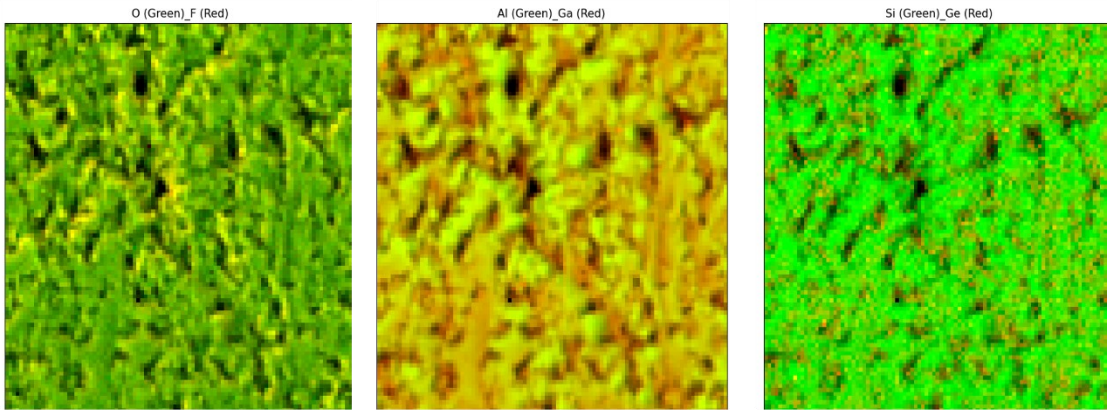

XRF Map 27
68x68um
86x86px
X= 28122
Y= 20507
SS 35um
50ms
XRF 3s
Zosa = -1749
Zzp = -251

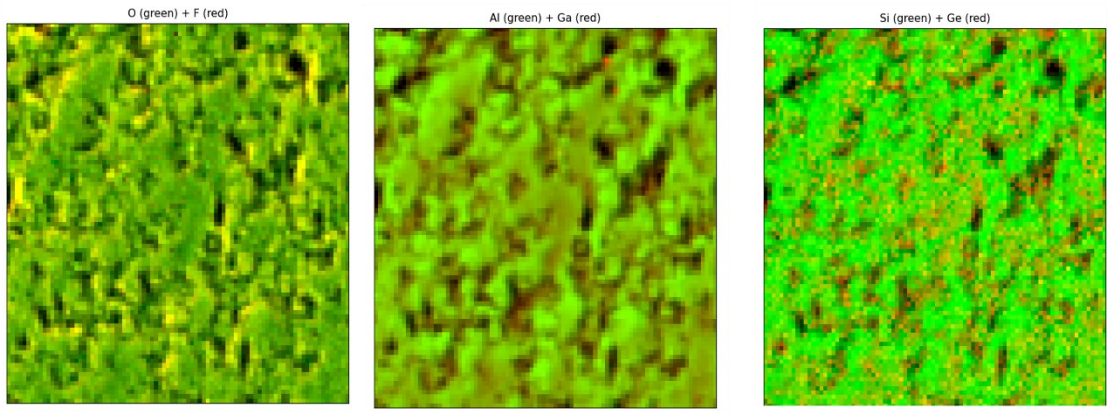

XRF Map 25
76x76um
96x96px
X= 28522
Y= 20507
SS 35um
50ms
XRF 3s
Zosa = -1749
Zzp = -251

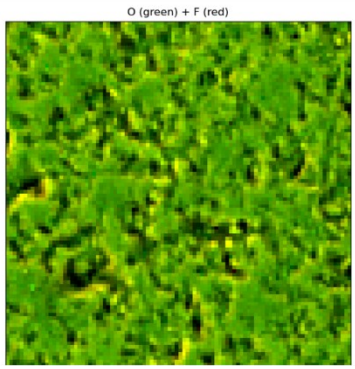

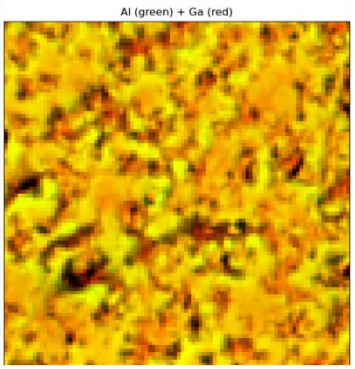

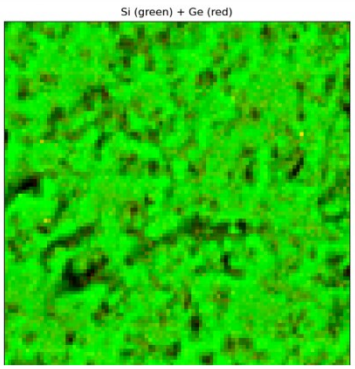

XRF Map 26
76x76um
96x96px
X= 28322
Y= 20507
SS 35um
50ms
XRF 3s
Zosa = -1749
Zzp = -251

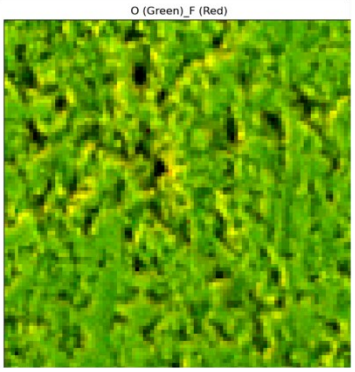

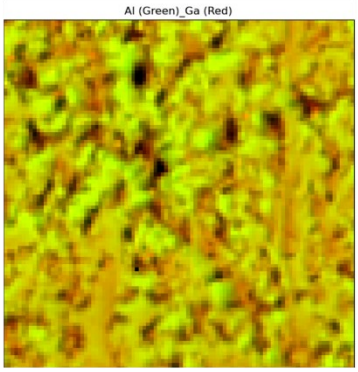

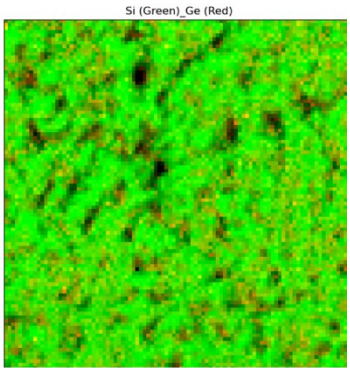

XRF Map 27
68x68um
86x86px
X= 28122
Y= 20507
SS 35um
50ms
XRF 3s
Zosa = -1749
Zzp = -251

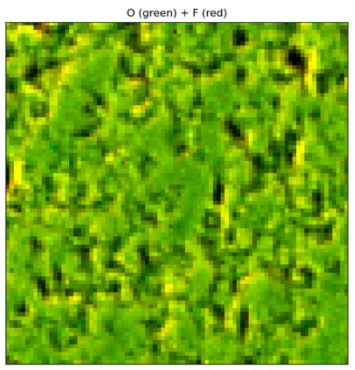

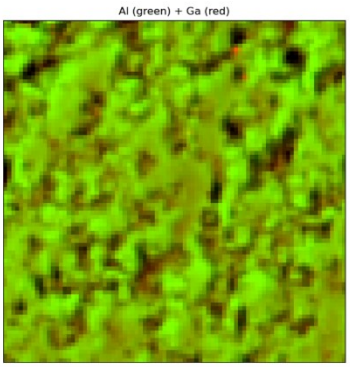

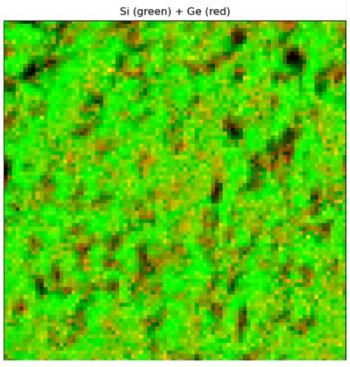

XRF Map 29
76x76um
96x96px
X= 27922
Y= 20507
SS 35um
50ms
XRF 3s
Zosa = -1749
Zzp = -251

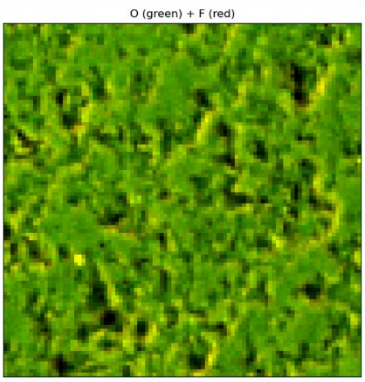

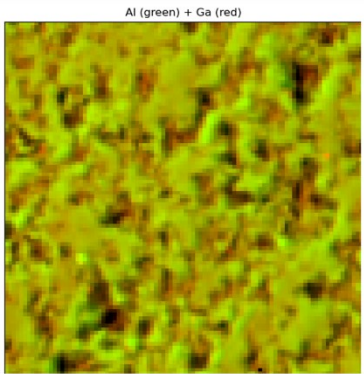

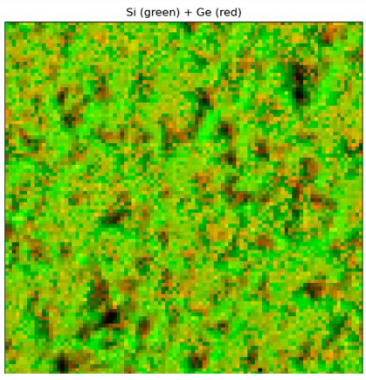

APPENDIX C 2: MAPS OF ELEMENTAL DISTRIBUTION FROM LEXRF, Baoshan

XRF Map 14
40x80um
51x101px
X= 20892
Y= 20507
SS 35um
Dt 50ms
XRF 5s
Zosa = -1749
Zzp = -251

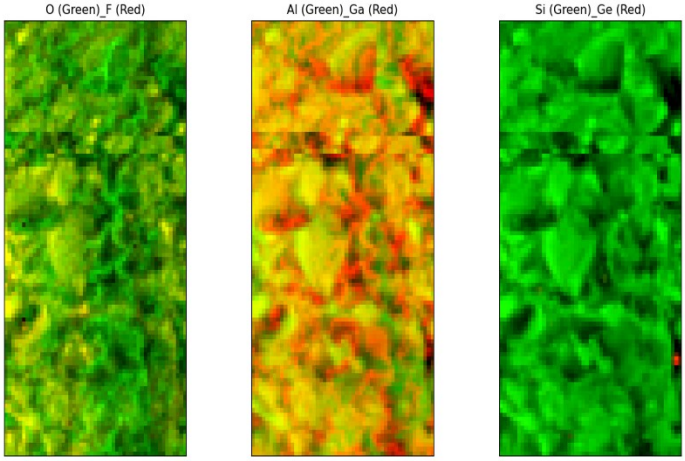

XRF Map 17
80x80um
101x101px
X= 21092
Y= 20507
SS 35um
50ms
XRF 3s
Zosa = -1749
Zzp = -251

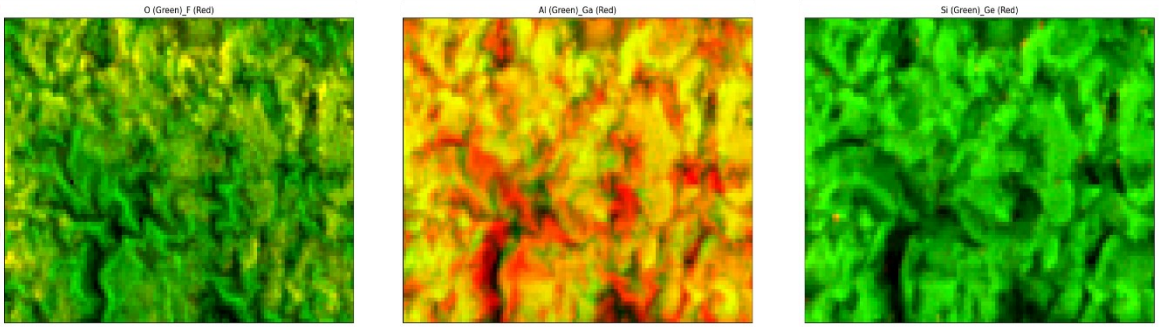

XRF Map 18
76x76um
96x96px
X= 21292
Y= 20507
SS 35um
50ms
XRF 3s
Zosa = -1749
Zzp = -251

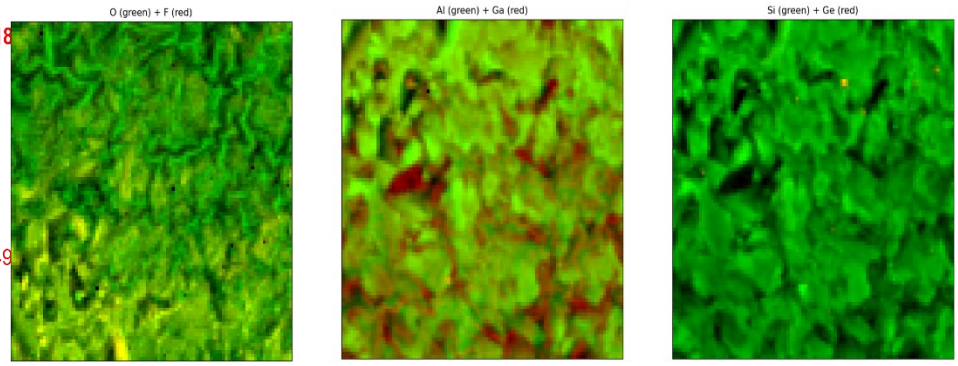

XRF Map 19
76x76um
96x96px
X= 21492
Y= 20507
SS 35um
50ms
XRF 3s
Zosa = -1749
Zzp = -251

O (green) + F (red)

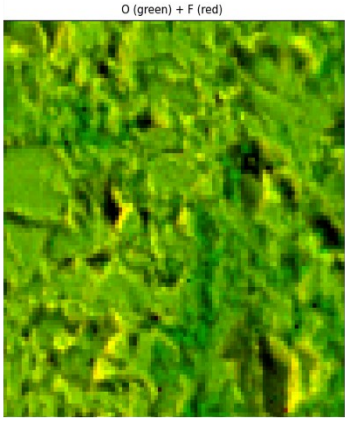

Al (green) + Ga (red)

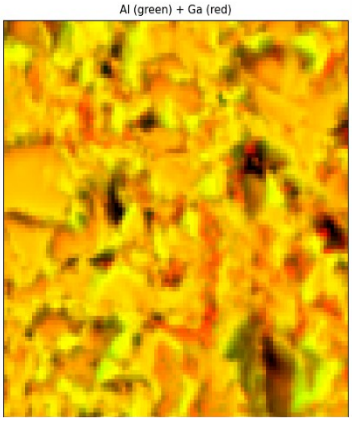

Si (green) + Ge (red)

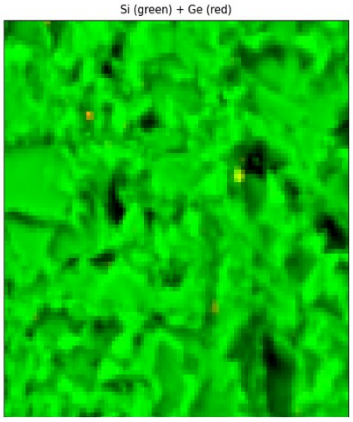

XRF Map 21
72x72um
91x91px
X= 21692
Y= 20507
SS 35um
50ms
XRF 3s
Zosa = -1749
Zzp = -251

O (Green)_ F (Red)

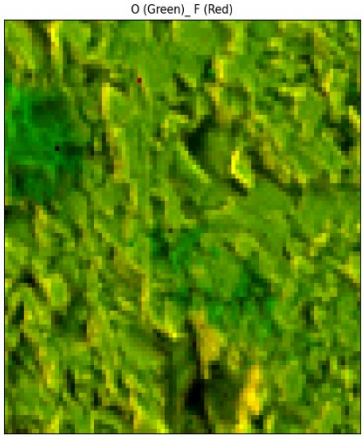

Al (Green)_ Ga (Red)

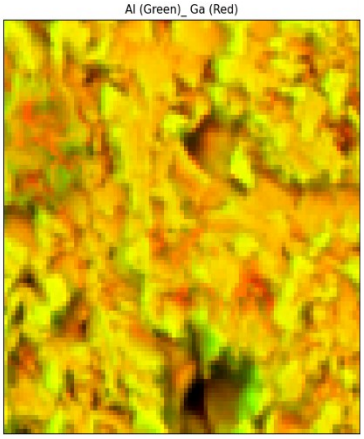

Si (Green)_ Ge (Red)